



LIBRARY Michigan State University

This is to certify that the

thesis entitled

FINITE ELEMENT SIMULATION OF SWAGING IN

THIN-WALLED CYLINDERS

presented by

Eric James Leaman

has been accepted towards fulfillment of the requirements for

Master's degree in Mechanics

Ronald C. averill

Major professor

Date March 28, 1995

O-7639

MSU is an Affirmative Action/Equal Opportunity Institution

PLACE IN RETURN BOX to remove this checkout from your record.
TO AVOID FINES return on or before date due.

PLACE IN RETURN BOX TO AVOID FINES return	on or before date due.	
DATE DUE	DATE DUE	DATE DUE
JAN 1 7 1997		
11:719694		
		-
	-	
	_	
	athe Action/Es	qual Opportunity Institution characteristics pm3-p.1
MOI LIE A	O AMILINATIVE PROPERTY	 -

MSU is An Affirmative Action/Equal Opportunity Institution

FINITE ELEMENT SIMULATION OF SWAGING IN THIN-WALLED CYLINDERS

BY

Eric James Leaman

A THESIS

Submitted to
Michigan State University
in partial fulfillment of the requirements
for the degree of

MASTER OF SCIENCE

Department of Materials Science and Mechanics

ABSTRACT

FINITE ELEMENT SIMULATION OF SWAGING IN THIN-WALLED CYLINDERS

By

Eric James Leaman

The sheet metal forming operation of swaging can produce wrinkles in a thin-walled cylinder. In order to alleviate wrinkling, an understanding of the deformations and stress state was necessary to isolate those variables controlling the formation of wrinkles. In this investigation, a finite element model for simulating the swaging process was developed using the commercial finite element code MARC. Revealed in the analysis was the presence of tensile circumferential stresses on the inner surface of the cylinder in the wrinkling region. These stresses, in conjunction with the transcending of critical circumferential strain levels were hypothesized to be responsible for wrinkling. A proposal was made to increase the cylinder wall's effective moment of inertia by the introduction of a circumferential stiffening rib.

ACKNOWLEDGEMENTS

I would like to acknowledge the Faculty and Students of the Department of Materials Science and Mechanics for their guidance in completing this project. In particular, I would like to thank Mr. Mike Wood and Dr. James Lucas for their contribution of the mechanical properties, and also Mr. Yue (Jeffery) Qiu for drawing Figure 1.1 of the text. I would like to acknowledge the financial support of the United States Can Company under grant 61-8502. I would like to thank the personnel at MARC Analysis Research Corporation for their assistance in using their product. I must, also extend my gratitude to my research advisor, Dr. Ronald C. Averill, for his guidance and support throughout this project. Although simple words are inadequate, I must say thank you to my wife Laurie for all of her encouragement, support, and sacrifices that she has made during the completion of this work.

Table of Contents

List of Tables	vii
List of Figures	x
Chapter 1 Introduction	1
1.0 Introduction	1
1.1 Problem Statement	5
1.2 Literature Review	7
1.3 The Present Study	25
Chapter 2 Modelling of the Swaging Operation	28
2.0 Introduction	28
2.1 Geometric Model of Cylinder and Forming Tools	29
2.1.1 Preliminary Element Selection	33
2.1.2 Evaluation of Element Performance for a Linear Problem	35
2.1.3 Discussion of Results for a Linear Problem	37
2.1.4 Nonlinear Evaluation of Element Performance	43
2.2 Boundary Conditions and Contact Constraints	45
2.2.1 Boundary Conditions	45
2.2.2 Initial Stresses	47
2.2.3 Contact Conditions	50

2.3 Material Model	52
2.3.1 Mechanical Properties	52
2.3.2 Plasticity Model	54
2.4 Solution Parameters and Analysis Options	57
2.4.1 Solution Method	57
2.4.2 Analysis Options	59
Chapter 3 Numerical Simulation of Swaging	60
3.0 Introduction	60
3.1 Simulation of the Swaging Process	61
3.2 Final Element Selection	66
3.2.1 Forming Analysis Results Using Element 1	67
3.2.2 Forming Analysis Results Using Element 116	67
3.3 Convergence of Forming Problem	69
3.3.1 Mesh Refinement Study	71
3.3.2 Discussion of Mesh Convergence Study Data	73
3.3.3 Comparison of Stress Trends Resulting from Mesh Refinement	81
3.3.4 Convergence Study on Number of Load Increments	91
3.4 Results from Forming Simulation	91
3.4.1 Strain and Stress States in the Critical Region	91
3.4.2 Assessment of Strain Hardening and Initial Stress Effects on Strain and Stress States	93
Chapter 4 Discussion of Wrinkling	102
4.0 Introduction	102

4.1 Existence of Critical Strain	103	
4.2 Bending Effects	106	
4.3 Introduction of Stiffening Rib	108	
Chapter 5 Summary and Future Work		
5.1 Summary	122	
5.2 Future Work	123	
APPENDIX		
A.1 Mesh Refinement Study Data	128	
A.2 Analysis Results without Strain Hardening	137	
REFERENCES		

List of Tables

Table 2.1	MARC Elements	34
Table 2.2	Predicted maximum deflection due to a circumferential line load in a simply supported cylinder of radius=1.0, thickness=0.1, and length=100.0. All values are normalized to the closed form solution.	38
Table 2.3	Predicted maximum deflection due to a circumferential line load in a simply supported cylinder of radius=5.0, thickness=0.05, and length=300.0. All values are normalized to the closed form solution.	39
Table 2.4	Predicted maximum deflection due to a circumferential line load in a simply supported cylinder of radius=100.0, thickness=1.0, and length=200.0. All values are normalized to the closed form solution.	42
Table 2.5	Nonlinear test case results corresponding to the predicted maximum deflection due to a circumferential line load in a simply supported cylinder of radius= 100.0, thickness=1.0, and length=100.0. All values are normalized to the closed form solution.	44
Table 2.6	Mechanical Properties of Double-Reduced Tinplate Steel, Type L.	53
Table 2.7	Stress versus Plastic Strain for Double-Reduced Tinplate Sheet Steel, Type L.	56
Table 3.1	Percentage Change in Axial Strain Values in the Critical Region. (%)	76
Table 3.2	Percentage Change in Circumferential Strain Values in the Critical Region. (%)	76

Table 3.3	Stress Values for 250 vs. 500 incs for the First Stage in the Critical Region.	92
Table 3.4	Stress Values for 250 vs. 500 incs for the Second Stage in the Critical Region.	92
Table 3.5	Effects of Strain Hardening on the Global Minimum and Maximum Strain and Stress Values.	94
Table 3.6	Effects of Initial Stresses on the Global Minimum and Maximum Strain and Stress Values.	95
Table A.1	Axial Strain on the Outer Surface in the First Bending Region. $(x10^{-3})$	128
Table A.2	Axial Strain on the Mid-Plane Surface in the First Bending Region. $(x10^{-3})$	128
Table A.3	Axial Strain on the Inner Surface in the First Bending Region. $(x10^{-3})$	129
Table A.4	Circumferential Strain on the Outer Surface in the First Bending Region. $(x10^{-3})$	129
Table A.5	Circumferential Strain on the Mid-Plane Surface in the First Bending Region. $(x10^{-3})$	129
Table A.6	Circumferential Strain on the Inner Surface in the First Bending Region. $(x10^{-3})$	130
Table A.7	Axial Stress on the Outer Surface in the First Bending Region. (kPsi)	130
Table A.8	Axial Stress on the Mid-Plane Surface in the First Bending Region. (kPsi)	130
Table A.9	Axial Stress on the Inner Surface in the First Bending Region. (kPsi)	131
Table A.10	Circumferential Stress on the Outer Surface in the First Bending Region. (kPsi)	131
Table A.11	Circumferential Stress on the Mid-Plane Surface in the First Bending Region. (kPsi)	131

Table A.12	Circumferential Stress on the Inner Surface in the First Bending Region. (kPsi)	132
Table A.13	Axial Strains on the Outer Surface in the Critical Region. (x10 ⁻³)	132
Table A.14	Axial Strains on the Mid-Plane Surface in the Critical Region. $(x10^{-3})$	132
Table A.15	Axial Strains on the Inner Surface in the Critical Region. (x10 ⁻³)	133
Table A.16	Circumferential Strains on the Outer Surface in the Critical Region. $(x10^{-3})$	133
Table A.17	Hoop Strains on the Mid-Plane Surface in the Critical Region. (x10 ⁻³)	133
Table A.18	Hoop Strains on the Inner Surface in the Critical Region. (x10-3)	134
Table A.19	Axial Stresses on the Outer Surface in the Critical Region. (kPsi)	134
Table A.20	Axial Stresses on the Mid-Plane Surface in the Critical Region. (kPsi)	134
Table A.21	Axial Stresses on the Inner Surface in the Critical Region. (kPsi)	135
Table A.22	Circumferential Stresses on the Outer Surface in the Critical Region. (kPsi)	135
Table A.23	Circumferential Stresses on the Mid-Plane Surface in the Critical Region. (kPsi)	135
Table A.24	Circumferential Stresses on the Inner Surface in the Critical Region. (kPsi)	136

List of Figures

Figure 1.1	Wrinkling Behavior Exhibited in Swaged Cylinder.	6
Figure 2.1	Relationship Between Modelled Surface and Full Cylinder.	30
Figure 2.2	Geometry of Forming Tools with Reference to the Cylinder Axis. (Not to scale)	31
Figure 2.3	MENTAT Model of Cylinder and Forming Tools.	32
Figure 2.4	Geometric Model with Applied Boundary Conditions.	46
Figure 2.5	Cross Section of Cylinder with Stress Resulting from Pure Bending.	48
Figure 2.6	Stress versus Plastic Strain for Double Reduced Tinplate Sheet Steel.	56
Figure 2.7	Newton-Raphson Solution Method.	58
Figure 3.1(a) First Stage of Swaging at the Zero th Increment.	62
Figure 3.1(b) First Stage of Swaging at the 50 th Increment.	62
Figure 3.1(c	First Stage of Swaging at the 100 th Increment.	63
Figure 3.1(d) First Stage of Swaging at the 250 th Increment.	63
Figure 3.1(e	Release of the First Stage Tool.	64
Figure 3.1(f) Tool Moved into Position in First Increment of Second Stage.	64
Figure 3.1(g	s) Second Stage of Swaging at the 352 nd Increment.	65
Figure 3.1(h) Final Increment of the Second Stage.	65

Figure 3.1(i)	Release of Second Stage Tool.	66
Figure 3.2	Swaging Analysis Using Element 116 with a 150x2 Mesh.	68
Figure 3.3	Sampling Locations for Convergence Study of Forming Analysis.	72
Figure 3.4	Axial Strain on the Outer Surface in the Critical Region vs. Mesh Size	74
Figure 3.5	Circumferential Stress on the Outer Surface in the Critical Region vs. Mesh Size.	74
Figure 3.6	Axial Strain on the Inner Surface in the Critical Region vs. Mesh Size.	75
Figure 3.7	Circumferential Strain on the Inner Surface in the Critical Region vs. Mesh Size.	75
Figure 3.8	Axial Stress on the Outer Surface in the Critical Region vs. Mesh Size.	78
Figure 3.9	Circumferential Stress on the Outer Surface in the Critical Region vs. Mesh Size.	78
Figure 3.10	Axial Stress on the Inner Surface in the Critical Region vs. Mesh Size.	79
Figure 3.11	Circumferential Stress on Inner Surface in the Critical Region vs. Mesh Size.	79
Figure 3.12	Computational Time vs. Mesh Size.	80
Figure 3.13	Axial Stress in the Critical Region for the Second Stage of the 150x8 Mesh.	83
Figure 3.14	Circumferential Stress in the Critical Region for the Second Stage of the 150x8 Mesh.	84
Figure 3.15	Axial Stress in the Critical Region for the Second Stage of the 300x8 Mesh.	85
Figure 3.16	Circumferential Stress in the Critical Region for the Second Stage of the 300x8 Mesh.	86
Figure 3.17	Axial Stress in the Critical Region for the Second Stage of the 150x2 Mesh.	87
Figure 3.18	Circumferential Stress in the Critical Region for the Second Stage of the 150x2 Mesh	88

Figure 3.19	Deformations of the 800x2 Mesh at Increment 303.	89
Figure 3.20	Deformations of the 150x2 Mesh at Increment 303.	89
Figure 3.21	Deformations for the 800x2 Mesh at Increment 373.	90
Figure 3.22	Deformations for the 150x2 Mesh at Increment 373.	90
Figure 3.23	Axial Strains in the Critical Region at the 503 rd Increment.	96
Figure 3.24	Circumferential Strains in the Critical Region at the 503 rd Increment.	97
Figure 3.25	Axial Stresses in the Critical Region at the 503 rd Increment.	98
Figure 3.26	Circumferential Stresses in the Critical Region at the 503 rd Increment.	99
Figure 3.27	Axial Stresses in Critical Region at 503rd Increment, Calculated without Initial Stresses.	100
Figure 3.28	Circumferential Stresses in the Critical Region at the 503rd Increment, Calculated without Initial Stresses.	101
Figure 4.1	Euler Buckling Column.	104
Figure 4.2	Shell Element Subject to Bending and Resultant Moments.	104
Figure 4.3	Circumferential Stress versus Strains for the First Stage of Forming.	109
Figure 4.4	Simple Beam Subjected to a Bending Moment.	114
Figure 4.5	Plate Subjected to a Bending Moment.	114
Figure 4.6	Initial Geometry of Cylinder with Added Stiffening Rib.	115
Figure 4.7	Formed Shape of the Cylinder with Added Stiffening Rib.	116
Figure 4.8	Final Shape of the Cylinder with Added Stiffening Rib after Elastic Snapback.	117
Figure 4.9	Axial Strains in the Critical Region of the Cylinder with Added Stiffening Rib.	118
Figure 4.10	Circumferential Strains in the Critical Region of the Cylinder with	119

Figure 4.11	Axial Stresses in the Critical Region for the Cylinder with Added Stiffening Rib.	120
Figure 4.12	Circumferential Stresses in the Critical Region for the Cylinder with Added Stiffening Rib.	121
Figure A.1	Axial Strains in the Critical Region Without Work Hardening.	138
Figure A.2	Circumferential Strains in the Critical Region Without Work Hardening.	139
Figure A.3	Axial Stresses in the Critical Region Without Work Hardening.	140
Figure A.4	Circumferential Stresses in the Critical Region Without Work Hardening.	141

Chapter 1

Introduction

1.0 Introduction

The current thrust in the manufacturing community is toward the conservation of resources and energy, while at the same time maintaining product quality and responding to the demands of the consumer. This philosophy has its roots in the latter days of the stone age and has evolved over the next six thousand years to its present state. The primary concern of early man was simply to obtain food to eat. The tools necessary to kill were fashioned by chipping flint into weapons. Eventually flint tools began to take on specific roles, such as axes, knives, or borers. Toward the end of the Stone Age man discovered the ease with which some materials could be worked into shape and metal forming was born. A couple of millennia later casting was found to make the working of metals

more efficient by eliminating some of the hammering necessary, but, because the castings were of copper, a soft material, it was still advantageous to use stone. Bronze improved the utility of cast tools, but shortcomings were still present. For instance, bronze chisels could not cut stone. Thus a new material was needed and iron was found to satisfy those needs, giving us the iron age (Parr, 1967). In each of these cases, societal needs for improved tools and weapons required new materials and methods of production to be developed. Many discoveries were made by pure luck and others were the result of investments in manpower, raw material, and time. The experiences of those working in metal forming built up over time and eventually a group of artisans was established.

The needs of the United States government in the late 18th century made it necessary to obtain a large stand of arms. The time and the gunsmiths necessary to fill the need was scarce. Eli Whitney was driven by these two circumstances to develop a new system of manufacturing whereby he would "form the tools so the tools themselves shall fashion the work and give to every part its just proportion - which when accomplished will give expedition, uniformity, and exactness to the whole" (Green, 1956). The process Whitney was proposing was currently being used to produce goods, but not on the scale of complexity that the musket required. The lock on a musket required an exact fit of the parts in order to work. This being the case, the standard of the day called for crude parts to be made and then assembled by a craftsman who filed and fitted the parts together to produce the working lock, a very time consuming task. Whitney's plan would eliminate the need for filing, and introduce the system of interchangeable parts. This evolution in manufacturing was consistent with the goals of speeding up the manufacturing process, reducing the labor necessary, and improving the quality in musket production. But the system still

required craftsmen to assemble the parts and tools needed to do the work. These two difficulties prevented the delivery of the arms on time, but the system was successful nonetheless.

Finally, Henry Ford brought mass production to its present form. He recognized the need for a low cost, high quality vehicle that almost anyone could afford. To do so required the marriage of five components: precision, standardization, interchangeability, synchronization, and continuity. While all of these existed individually, Ford brought them all together in the moving assembly line where the work moved to the worker who performed a single operation. Production costs were once again driven downward by this new manufacturing concept and the joys of driving were delivered to a wider audience. Thus the advent of mass production had arrived on the scene, with its roots stemming from Whitney's system of interchangeability. However, elaborate planning, expensive tooling, and exact synchronization of the parts moving through the plant were still required.

While each of these evolutionary steps has brought about greater efficiency and reduced cost in manufacturing, societal requirements are for even greater cost reductions, quicker product development times, and environmental impact awareness. To accomplish these manufacturers have turned to a concept known as simultaneous or concurrent engineering. This represents a fundamental change in the manner in which products are designed and manufactured. Previously a sequential process was followed. A need was defined, a part designed to meet the need, a means of manufacturing the part devised, and the process was tested. Rarely, though, is the cycle correct the first time. One or more of the components in the design cycle may have to be altered, thus forcing a retrial of the process. Trial and error is expensive and not consistent with the current thrust of conserva-

tion.

Concurrent engineering is "a more co-operative, simultaneous, computer-aided" approach to product development (Butman, 1991). Design and manufacturing engineers are voicing their concerns to each other at the initial stages. This parallel approach gives rise to a more efficient design cycle, but methods of analyzing the integrity of the part and the manufacturing process are also essential. Although trial and error methods served this function in the past, the decline of skilled tradesmen and the need for rapid results render this scheme insufficient. What is needed is a means to do the analysis without the physical product or process. Numerical methods are readily adept at performing this function.

Numerical methods consist of building mathematical models that are representative of the product and tools of the process. In this way testing is done on the computer rather than on the plant floor. The finite element method is one such numerical scheme available for the analysis of continuous structures that are currently being manufactured. The approach of the method is to model the structure by discretizing the geometry with a group of elements. The equations that govern the behavior of each of these individual elements are then assembled to produce a system of algebraic equations of the form

$$\mathbf{K}\bar{\mathbf{x}} = \mathbf{F} \tag{1.1}$$

where \overline{K} is the stiffness matrix of the entire structure and is a function of the elemental deformation modes and the material properties, \overline{x} is a vector of the displacements and rotations (or the degrees of freedom, DOF) that describe the deformations of the elements, and \overline{F} is a vector of the forces at discrete points within each element. By substituting the applied loading along with the DOF which are fixed on the boundary into Equation 1.1,

thus the global response of the structure may be predicted. The results obtained, however, are rarely exact because of the approximations necessary to manipulate the governing equations of the elements into the form of Equation 1.1. Even so, solutions accurate for engineering purposes can usually be obtained, though the large number of equations necessary to obtain theses results may demand the use of large scale computing machinery.

In the above paragraph it was assumed that the stiffness matrix, \overline{K} , and the force vector, \overline{F} , were independent of the displacement vector, \overline{x} . In many practical situations this is not true and the analysis becomes nonlinear. Such is the case when analyzing a manufacturing process. One such operation is sheet metal forming where a set of rigid tools introduces plastic deformations into a relatively simple geometry to produce the more complex configuration of the final product. The analysis of such an operation is nonlinear because of the large deformations required, the relationship between stress and strain, and the contact of the rigid tools and the blank. Not only does this add to the complexity of the finite element analysis, but it also renders nearly impossible any analytical solution. Therefore, the means to analyze sheet metal forming are either the trial and error method, which has been shown to be costly and contrary to the requirements of simultaneous engineering, or the development of computer models where part and process evaluation may be done for relatively little cost on the computer.

1.1 Problem Statement

A typical example of a metal forming operation is swaging or necking wherein the diameter of a cylinder is reduced by the action of a set of rigid dies. When using this pro-

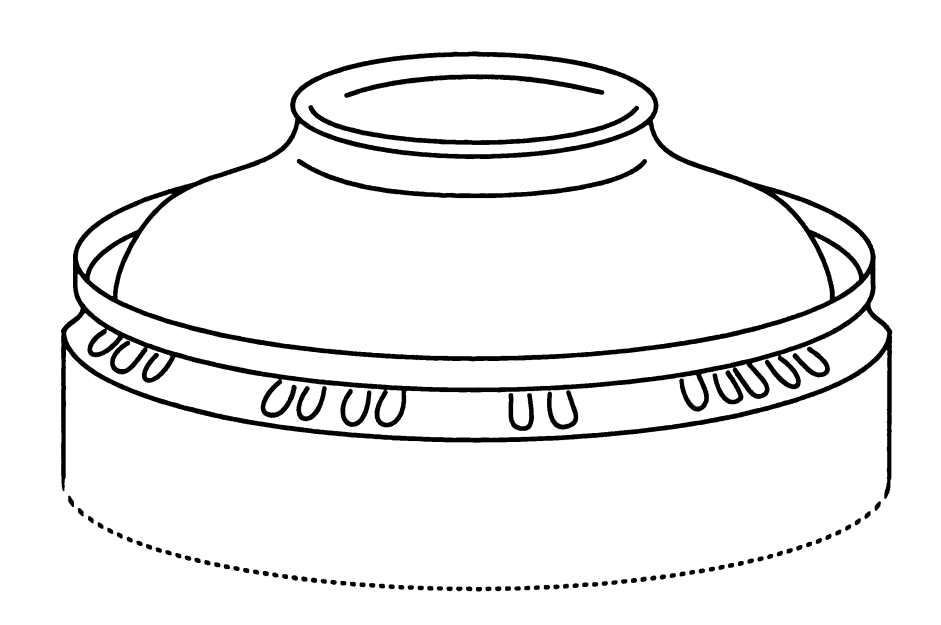


Figure 1.1 Wrinkling Behavior Exhibited in Swaged Cylinder.

cess on thin-walled cylinders the possibility then exists for the formation of wrinkles in the necked-in region, as shown in Figure 1.1. The wrinkles are the result of a build up of compressive circumferential stresses in the cylinder. When these stresses exceed some critical value, any disturbance, whether due to material imperfections or the manufacturing process, will cause the cylinder to buckle (or bifurcate) to an adjacent equilibrium position (the wrinkled configuration). One possible solution to the problem is to increase the thickness of the cylinder wall. However, arbitrary use of thicker material increases the cost associated with the purchasing of raw materials which in the end is passed on to the consumer or absorbed by the manufacturer, neither of which is desirable. In addition, other solutions may exist that will eliminate the misuse of resources. In other words, the increased wall thickness places greater demands on the environment both in terms of raw materials for steel production and waste management at the end of product life. However

an investigation of the stress state and kinematics of the cylinder during the swaging process may lead to an alternate solution that is consistent with the goal of conserving resources and energy. Trial and error techniques coupled with the die makers experience will not produce the desired information, and this also inherently conflicts with the current thrust in manufacturing as already explained. No analytical means of evaluating the process is available. The nonlinearities due to large deflections, plasticity, and contact between the cylinder and tools associated with the problem render the solution analytically intractable. Thus, a finite element simulation of the necking process is sought in order to achieve the stated objectives. With the stress states and deformations of the cylinder in hand, changes, whether in the material, the forming path, and/or the final geometry, with an engineering basis may be proposed to eliminate the wrinkling phenomena.

1.2 Literature Review

Early attempts to predict the success of a forming operation centered on the use of forming limit diagrams (FLD). The formation of the FLD is through experimental procedures wherein the sheet blank is etched with a grid pattern of circles. The blank is then stretched over an unlubricated punch and the deformation of the circles in the region of failure are observed. The shape of the etchings will have changed from circular to elliptical. The major strain is calculated by measuring the major axis of the ellipse and the minor strain from the minor axis. After a series of tests the delineation between a successful formation and one that fails is established (Kalpakjian, 1991). While experimental construction of FLD's has been successful, numerical prediction of the curves requires a failure criterion. Toh (1989) proposed a method of predicting the forming limit curves of sheet

materials using an incremental rigid-plastic finite element method and a new limit criterion. In the analysis of a hemispherical punch stretching a circular blank with various circular cutoffs and various friction conditions at the tool-sheet interface, the material was assumed to obey Hill's anisotropic yield criterion and its associated flow rule. The resulting set of load versus displacement curves were then used to derive a critical slope condition which could subsequently be used as a criterion to determine the corresponding critical major and minor strains. This approach has been shown to give reasonable prediction of the FLD's, but this is only a method of predicting the failure of the material. To understand the underlying behavior of a structure, simulation of the forming process is necessary.

Simulation requires a sophisticated finite element formulation, especially concerning those components giving rise to non-linearities. These include the large deformations that are usually introduced to the workpiece. The changes in the configuration of the workpiece should be permanent and as such the material experiences plastic deformations, another source of nonlinearity. Finally, the deformations are produced by a tool or set of tools that come into contact with the workpiece, thus introducing nonlinear boundary conditions into the analysis. While many considerations are necessary in the analysis of metal forming operations, these components draw the most attention.

Keck, et al. (1990) summarized results obtained for various sheet metal forming operations that were simulated using an implicit finite element code. In general, a variety of element types are used, but all are formulated based on the principle of virtual displacements and an updated Lagrangian description for the incremental calculation of the deformation process.

Use was made of the rate form of the elastic-plastic material model. However with the assumption of small strains, a hypoelastic constitutive law may be implied, because the strains may be decomposed into their elastic and plastic components. This required a yield function for the material which, in general, was assumed to conform to von Mises yield criterion. But in the case of a membrane element formulation, Hill's quadratic yield criterion was used, thereby taking into account the normal anisotropy. The rate form requires the integration of the constitutive relationship which was performed using either a radial return method or a return mapping algorithm.

The treatment of the changing contact conditions of the problem were handled in the following manner: The dies were treated as rigid bodies and in order to fulfill the contact conditions a penalty formulation was adopted. Penetration of the tool was checked only at nodes that were specified as contact nodes. Then a penalty factor was calculated for each possible contact node from the stiffness of the workpiece perpendicular to the tool surface and scaled by a user defined factor. The resulting contact friction was modelled with a modified Coulomb friction model. This overcame the problem of singularities arising in the first derivative of the Coulomb friction model at vanishing relative motions and enables the linearization of the friction law in connection with the Newton-Raphson iteration scheme.

The equilibrium of each incremental loading of the structure was obtained by a dynamic solution scheme. In general, the Newton-Raphson iteration method was used, but in cases where the rate of convergence reached some predetermined value, the so called BFGS method (named for Broyden Fletcher, Goldfarb, and Shanno, see for example, Zienkiewicz, 1989) was employed. The Newton-Raphson method was reintroduced upon a deceleration of the convergence rate.

The finite element formulation proposed was applied to the analysis of hydrostatic bulging of a circular sheet of annealed aluminum, hydrostatic bulging of rectangular sheets of anisotropic mild sheet steel, an axisymmetric stretch forming process, and the deep drawing of a rectangular cup. In each case the results showed good agreement with previous experimental work. The authors point out, however, that the formulation presented is limited to materials which have accurately identified constitutive models and material parameters. Emphasis is thus placed on the accurate description of the material behavior through experimental techniques before proceeding with more complex analyses than those performed.

A more complicated analysis was conducted by Lee, et al. (1991) on a stretch-drawing process particularly used in the automotive industry. The aim was to develop a finite element method which resulted in acceptable computational times, while retaining the ability to model the key features of a metal forming analysis. Chief among these being the contact algorithm which is generally regarded as a major issue for numerical stability. As such the authors implemented a membrane line element consistent with a shell formulation for the contact formulation. Additionally, to aid in the reduction of computational time, the number of degrees of freedom within the shell elements was reduced.

The model was formulated using an updated Lagrangian description of motion. In addition, the shells used to describe the sheet metal were assumed to be thin and therefore, the through the thickness shear deformations could be neglected. With a full bending theory being considered, the strain expressions contained the second derivative of the incremental in-plane displacements. The degrees of freedom therefore consisted of the change in axial displacement, the change in transverse deflection, and their first derivatives. But,

by assuming a linear variation of the incremental axial displacement, its derivative was no longer required, resulting in a net reduction in the number of DOF in the model. Therefore, the interpolation functions used in the finite element formulation were linear for inplane displacements and Hermite cubic for the transverse deflection. These interpolation functions were then used in the principle of virtual work, which when linearized along with a geometric constraint for tool contact resulted in the stiffness matrices and force vectors due to inertia, contact forces, and internal reactions. When evaluating the resulting algebraic equations the through the thickness integration was reduced to single point quadrature rule in order to reduce computational time, while retaining the key features of the bending model.

In regard to the material model of the formulation, the response was assumed to be rigid visco-plastic so that incompressibility could be applied using small natural strains. In addition, normal anisotropy was taken into account through the use of Hill's yield criterion. Finally, a power law hardening relation with strain rate sensitivity of the form

$$\bar{\sigma} = \sigma_o + K (a_o + \bar{\epsilon}_o + \Delta \bar{\epsilon})^n (\dot{\bar{\epsilon}}/\gamma)^m$$
 (1.2)

was implemented, where σ_o is the yield stress, K is the material strength parameter, a_o is the pre-strain, n is the strain hardening exponent, m is the strain rate sensitivity index, and γ is the base strain rate. Using this expression a wider variety of sheet metals could be considered.

Finally, the detection of contact between the tool and the workpiece was indicated by satisfaction of the following,

$$g_n \equiv \mathbf{n} \cdot \left(\mathbf{x}^p - \mathbf{x}^s \right) = 0 \quad , \tag{1.3}$$

where n is the normal between the tool and the workpiece and x^p and x^s are position vectors of a point on the sheet and it nearest point on the tool. However, because x^p and x^s are unknowns the equation must be linearized and solved iteratively. This was a general gap condition. In the event that the tool moved only in the vertical direction, a vertical gap parameter would be used. In either case, when the tool and sheet metal were in contact external forces would be transmitted through the tool to the sheet metal and therefore a consistent contact formulation was required.

The methods used above show good agreement with other numerical results as well as with experimental data. However, it was found that when the strain reaches the n value of the strain hardening equation (1.2), the model failed to converge. This difficulty was due to a loss of definiteness in the stiffness matrix and is termed softening.

Rebolo, et al. (1990) are members of a team developing a general robust finite element code for the analysis of sheet metal forming problems. As such the techniques which they employ have been proven to be effective in the solution of these types of analyses. The focus of the discussion was again toward the element types used, the modelling of the contact condition, and the frictional model used in the metal forming analyses. Little consideration was given to the constitutive model as it appeared to the authors that the conventional elasto-plastic models together with small strain linear elasticity, a smooth flow surface, and isotropic hardening provided adequate representation of the material behavior

during forming.

In discussing the types of elements which are available, the authors point out that the use of continuum elements is prohibitively expensive. These computational difficulties can be overcome by the use of structural elements, such as membrane or shell elements, but these elements introduce the inability to handle two-sided contact due to their lack of ability to accommodate thickness stresses. In contrast, the introduction of assumed strain and stress elements allow for the advantages of structural elements, while at the same time providing for two-sided contact.

The formulation presented was based on a membrane element which employed finite strain plasticity. Generally this type of formulation would require the introduction of an additional rotation tensor to account for the stresses and strains. However, a more direct method was offered by calculating the strain measures from the polar decomposition of the incremental deformation gradient, the incremental rotation vector, and the incremental plastic strain. The stress was then a function of the elastic strain. The advantage of this formulation was the ease in which it may be implemented in an updated Lagrangian framework.

A simplified approach to the detection of contact and the use Lagrange multiplier techniques to impose the no penetration constraint were employed. A measure of overclosure, quite similar to that proposed by Lee, et al., was formulated by calculating the distance along the normal from the closest point on the rigid surface to the contact node on the deformable body. When the overclosure is greater than or equal to zero, contact is detected and a Lagrange multiplier was introduced which provided the contact pressure.

Finally, when contact was identified a Coulomb friction model was employed to

account for the sticking or slipping stresses generated within the model. Again this was done by introducing Lagrange multipliers. In this situation, however, the parameters could take on different roles. In the event that sheet metal and the die stuck together the Lagrange multiplier was used to enforce the constraint that the shear strain was zero. Conversely for a sliding condition, the Lagrangian took on the value of the frictional stress.

Within each of these formulations the technique used for the detection of contact was carried out in similar fashions. A normal vector from the tool(s) to the workpiece was constructed and when the magnitude of the vector goes to zero contact was assumed. Once contact has been realized, a constraint must be added to the governing equations to prevent penetration of the tool into the material. In general this constraint was enforced in one of two manners, either a Lagrange multiplier was used or a penalty function parameter was used. The Lagrange multiplier enforces the contact condition exactly, but at the expense of additional DOF in the solution. Also, a singular stiffness matrix can result from this formulation. Both of these difficulties can be avoided by using the penalty function, but satisfaction of the contact condition is not exact and the solution is highly sensitive to the choice of the penalty factor. In each case the contact constraint is enforced in a "pointwise" sense.

A method of enforcing the contact constraint in an average sense over the element boundary was proposed by Simo and Taylor (1985). This work was conducted within the context of bilinear isoparametric interpolation of the displacement field, thereby allowing the assumption that the contact pressure was constant over each contact segment, and discontinuous across segments. The contact constraint was therefore enforced in an average sense over the contact segment, rather than in a pointwise manner. This resulted in the

average gap being a kinematic variable.

The introduction of the average contact constraint was accomplished by using a perturbed Lagrangian formulation of the total potential energy functional. By defining the gap function in the usual manner, a modified total potential energy functional for the constrained system may be written as

$$\Pi_{\varepsilon}\left(\underline{u}^{1},\underline{u}^{2},\lambda\right) = \sum_{A=1}^{2} \Pi^{A}\left(\underline{u}^{A}\right) + \lambda g - \frac{1}{2\varepsilon}\lambda^{2}$$
(1.4)

where the first term on the right hand side is the potential energy, the second term is the contribution of the Lagrangian constraint, and the last term has the form of a penalty term. As this penalty term goes to infinity, $\varepsilon \to \infty$, the standard Lagrangian formulation is recovered. The real value in adding the additional 'penalty term' to the functional was that the possibility of a non-positive definite stiffness matrix was eliminated. The perturbed Lagrangian functional could then, after taking the first variation, be used to formulate a finite element solution to the contact problem.

Yet the perturbed Lagrangian formulation, as with the other classical approaches, is not without faults. In each method only those constraints that were active during the iteration contributed to the incremental equations. Undesirable consequences may arise from this approach. For example, the quadratic convergence of the Newton-Raphson method may be seriously affected if there are frequent changes in the active set.

By introducing a method in which all the inequality constraints are enforced directly by means of additional equations together with the equilibrium equations to form a system of nonlinear equations in the displacements and the contact tractions, the New-

ton-Raphson method may be used to overcome these difficulties. Just such an algorithm was introduced by Eterovic and Bathe (1991). The goal was to derive a set of finite element equations that would explicitly account for the presence of the contact conditions. This was done by formulating the virtual work for a continuous body in a total Lagrangian fashion. To this statement was added the virtual work done by the contact tractions over the virtual relative displacements between the contacting bodies. A second governing equation was derived from the contact conditions. Thus, using the two equations in conjunction resulted in a complete variational formulation of the motion. These equations were then cast into a finite element model which contained n+4m unknowns, where n is the number of nodal dof and m is the number of contact nodes. But the elegance of the model was that all the inequality constraints associated with the contact conditions were contained within the finite element equations. But this gives rise to a highly nonlinear set of equations, and therefore a robust solution technique was paramount.

Riccobono (1992) presented a comparison of two methods which are used to handle the nonlinearities presented by the plasticity model in metal forming problems. The first was a matrix method proposed by Prager and Hodge in which the actual strain rate field of the analysis was the one that satisfied the following:

$$J = \frac{2}{\sqrt{3}} \sigma_0 \int_V \sqrt{\frac{1}{2} \dot{\varepsilon}_{ij} \dot{\varepsilon}_{ij}} dV - \int_{S_\tau} T_i v_i dS$$
 (1.5)

where S is the surface and T_i are components of the surface traction. In this formulation, the incompressibility condition is enforced using Lagrange multipliers. Thus the problem

is defined as finding the minimum to a functional which combines (1.5) and the Lagrangian constraint of the incompressibility condition.

The second method used the infinitesimal strain increment form of (1.5). Linearizing the yield surface by a set of tangent planes and using Gaussian numerical integration, the functional was written as,

$$J = \sqrt{2}c \sum_{j=1}^{4} 2\pi r_{j} S_{j} \sum_{i=1}^{n_{i}} d\lambda_{i} - \sum_{i=1}^{n_{i}} F_{i} du_{i}$$
 (1.6)

where for the axisymmetric state, $2\pi r_j S_j$ is the volume associated with the integration point j, and u_i the number of the nodes on which the forces F_i are applied. Thus, using this new functional along with two sets of restraints (one which states that the infinitesimal strain increments derived by the velocity field equals the one derived by imposing the normality law at each integration point and the other stating that the die never penetrates the blank) the linearization of the yield function is complete.

A comparison of the two methods revealed that the first formulation is based on an iterative process and uses a non-linear system of equations, while, on the other hand, the second formulation is given in a closed form and thus eliminates any chance of convergence problems. This also meant that the matrix method may allow the tool to penetrate the blank during a solution step, but the linearization technique enforces the non-penetration restraint explicitly. Therefore the linearization method may provide superior performance to the matrix method, but the increased number of unknowns associated with the formulation may indeed cancel any advantages gained.

Finite element models are usually formulated for fully three dimensional or possi-

bly two dimensional spaces when assumptions of plane stress or plane strain are made. This may lead to a prohibitively expensive analysis in the case of a nonlinear metal forming problem. In cases when the geometry, properties, and loading are constant in one direction, for example an axisymmetric problem, the model may be simplified by modelling the mechanical fields in that coordinate with a traditional, trigonometric Fourier series. In general this method fails to satisfy the anisotropic form of the governing equations for laminated composite structures. Padovan (1974) developed a quasi-analytic finite element procedure for axisymmetric anisotropic shells and solids by using the exact functional representation for the circumferential variable dependency.

In shell theory for anisotropic materials the appearance of the shearing terms in the stiffness matrix cause the traditional, trigonometric Fourier series approach to break down when trying to obtain a solution for the equilibrium equations. One possible resolution is to transform the equilibrium equations into an orthotropic form, but the analytical solution is intractable due to the distortion of the boundary conditions. Therefore, it was proposed to cast the displacement vector into a complex Fourier series expansion. Applying the new formulation for the displacement and force vectors in the equilibrium equations yielded a complex differential equation with the real and imaginary parts of the displacement vector being coupled for the fully anisotropic case. The difficulty in obtaining an analytical solution lead to the development of a finite element solution. The formulation of the finite element equations was the same as a traditional approach with the exception that the displacement and force vectors were in the complex, Fourier expansion form. This lead to a complex stiffness matrix for solution.

The procedure outlined was tested against problems with known solutions and it was found that the complex form of the equations gave very good approximations in all

cases. Given the accuracy of the results and the difficulties in using the traditional Fourier series, the complex Fourier series representation appeared to have some advantages, especially in that the significant effects of material anisotropy were revealed by its use.

Two constraints on the use of the semi-analytic, or finite strip method are that the geometry of solids of revolution be axisymmetric and that the material properties in the circumferential direction be constant. To broaden the scope of the method Sedaghat and Hermann (1983) proposed relaxing the first constraint and removing the second altogether. The formulation started with the removal of the circumferential or theta dependence of the total potential energy of the system. This was done by expanding the displacements and body forces with a trigonometric Fourier expansion. However the elastic coefficient matrix may also be theta dependent. This difficulty was handled by decomposing this matrix into two components called the base properties and the deviation properties respectively. The base properties are theta independent and are in most cases found by averaging the material properties in theta coordinate. The deviation properties are simply the deviation from the base values.

From the decomposed elastic matrix the stress-strain relationship was in the form of

$$\sigma^{N} = \bar{D}\varepsilon^{N} + \tilde{D}\varepsilon^{N-1} \tag{1.7}$$

where the first term was independent of theta and yielded the usual uncoupled equations and the second term was theta dependent and contributed to the load matrix in a manner similar to initial stresses. The finite element model could then be constructed from the

total potential energy of the system.

The variation of the material properties aided in the formulation of the semi-analytic method for non-axisymmetric geometries. By idealizing the geometry and then varying the material properties a semi-analytic formulation could be brought about. For example a semi-infinite plate with a hole loaded by internal pressure was idealized by a circular plate of radius ρ , where ρ was chosen such that the value of stress in the x direction was small. If the hole is near the top edge of the plate, the edge effects would be accounted for by varying the properties within the idealized plate. Results from a finite element model formulated using the idealized geometry and the varying material properties were in good agreement with the closed form solution for the problem. Thus it appears that the scope of the Fourier series formulation had been broadened.

Attention will now be turned to analyses involving the formation of wrinkles in sheet metals. Currently the most popular method of predicting wrinkle failures is the Yoshida Buckling test. However, this method, as well as other empirical techniques, have proved to be inadequate for observed trends. In particular the local curvature of sheet metal during forming has been shown to have a significant effect on the conditions for wrinkling, but the empirical methods fail to account for this parameter.

Neale and Tugcu (1990) concentrated on some of the basic features of wrinkle formation, in particular those occurring within the context of the plastic buckling theory for thin plates and shells. Wrinkling can be viewed as a plastic buckling process in which a wavelength of the buckles in one direction is very short. This buckling is local and dependent on the local curvature, the thickness of the sheet, on the material properties, and the local stress state.

The basic element considered had constant radii of curvature R₁ and R₂ and constant thickness t, the state of stress was assumed to be a uniform membrane state (no bending), and the investigation was limited to those regions of the sheet that were not in contact with the die. Simplifications arose by exploiting the fact that the short-wavelength wrinkling modes were shallow and could be analyzed by the Donnell-Mushtari-Vlasov (DMV) shallow shell theory, which restricted the analysis to modes where the characteristic wavelength was large in comparison to the thickness, but small compared to the local radii of curvature.

To determine the critical stress state for buckling, a so called "bifurcation functional" was developed. For all admissable displacement fields the condition that the second variation of the bifurcation functional is greater than zero ensures buckling does not occur. However, buckling becomes possible when the bifurcation functional is zero for some non-zero field. The analysis was done by considering three fields in the bifurcation functional and then integrating over some local region, S, which was separated from the rest of the sheet. Because the integration is carried out over a local region, the boundary or continuity conditions are relatively unimportant.

The bifurcation model may also be written as a function of the buckling displacements and a coefficient matrix, M. When the determinant of the matrix M goes to zero, buckling was again predicted. Also, by minimizing the determinant with respect to some waveform parameters and setting it equal to zero, the critical stresses associated with buckling could be found. Because of the complexity of the equations, closed-form solutions to the problem are difficult to obtain, therefore numerical solutions are generated by means of the Newton-Raphson technique. This gave rise to an understanding of how the material flowed in the plastic regime. The most widely used constitutive relations in buck-

ling are based on the J2 flow theory or the J2 deformation theory of plasticity. In addition, the material behavior has been assumed to be isotropic and the power-law hardening rule used.

A parametric study was done to determine the influence of material properties and geometry of the critical stress state for local buckling. Material constant values of mild steel and low-hardening steel were used and the results were plotted in terms of principal compressive stresses and angle between the principal stress axes and the principal axes of curvature. When comparing the flow theory results to the deformation theory results, the deformation theory gave a more conservative prediction for the onset of wrinkling than that of the flow theory and as a result was the preferred theory. Also, the results showed that the critical stresses for the onset of wrinkling decreased as the strain hardening exponent decreased and the critical stresses were also shown to decrease with the thickness of the sheet.

Chan (1993) presented a method for locating the bifurcation points on the generalized force-displacement curve. This method was to be carried out in conjunction with any technique which could traverse the limit point using the following equation,

$$\left[\Delta F_i^k + \Delta \lambda_i^k \Delta F\right] = \left[K_T\right]_i^k \left[\Delta u_i^k + \Delta \lambda_i^k \Delta \bar{u}\right] \tag{1.8}$$

where $\Delta \lambda_i^k$ is the load parameter vector, ΔF_i^k is the vector of unbalanced forces, Δu_i^k is the residual displacement vector, ΔF is the reference load vector parallel to the applied load vector, and $\Delta \bar{u}$ is the vector of conjugate displacement. The superscript is the load increment and the subscript is the iteration within the load increment. The load parameter,

 $\Delta \lambda_i^{\kappa}$, was chosen such that the equilibrium error was minimized and the load increment was chosen using the constant arc-length method. This procedure has shown to have good convergence and reliability against divergence.

A change in equilibrium state was detected by checking,

$$Det\left(K_{T}^{k}\right) \bullet Det\left(K_{T}^{k+1}\right) < 0 \quad . \tag{1.9}$$

When the above equation was satisfied, a critical point was found to lie between the solutions at k and k+1. The location of the critical point was within the displacement degree of freedom with the largest increase during the load increment. The secant method was then used to predict the displacement increment, Δu_m , which caused the determinant of the tangent stiffness matrix to go to zero. The iterative procedure outlined satisfied simultaneously the equilibrium and semi-definite conditions for the structural system and was more efficient than satisfying them separately. Finally, equilibrium was assumed when both the Euclidean norms of the residual displacements and of unbalanced forces were less than 0.1% of their respective total or accumulated normal. The semi-definite condition was fulfilled when the change of correction load factor, $\Delta \lambda_i^{\kappa}$, was less than 1×10^{-5} of the first load.

Yu and Zhang (1988) investigated the plastic wrinkling of an circular plate being transformed into a cup by means of a deep drawing operation. To do this they attempted to develop a criterion for combinations of geometry and material properties that gave rise to wrinkling on the upper flange of the cup. The geometry of the investigation was simplified

by assuming an annular ring with a uniform tension applied on the inner edge. By non-dimensionalizing the wrinkling equation, the Kantorovich method was used to produce an ordinary differential equation (ODE). However before the Kantorovich method was applied it was assumed that the transverse deflection of the ring was the product of two functions, f, a function of the non-dimensionalized radius, and g, a function of the angle theta and the number of waves. The resulting ODE was then a function of the non-dimensionalized radius and was not readily solvable. Therefore the Galerkin method was applied to obtain an approximate solution. The result of the Galerkin analysis yielded two equations which could be used to establish a criterion to show which combinations of geometry and material properties would result in wrinkling. The authors then used these equations to develop curves showing the faulty combinations and thus gave the limits for safe production.

Finally, Adams (1993) investigated the wrinkling of a pre-tensioned, circular plate subject to a concentrated load at the center. Using the von Karman plate equations, analysis of the axisymmetric response was performed followed by an algorithm to determine if wrinkling resulted from the calculated displacements. In finding the deflections and stress state due to the load, the static, axisymmetric governing equations were cast into finite difference form. The resulting set of N nonlinear, banded algebraic equations were solved by an iterative solution routine. This reference configuration must then be checked to see if wrinkling was induced. Accomplishing this goal required returning to the full von Karman equations and replacing the displacements by perturbation expansions in ε . Collecting terms would reveal that the zeroth order terms reflect the axisymmetric results while the first order terms gave a new set of governing equations which were coupled to the refer-

ence configuration by the transverse deflection and the circumferential stresses. The first order perturbation displacements were then taken to be the product of a function of radius and circumference and a harmonic function of time. Dependence on the circumferential direction was removed by an exponential Fourier series expansion and using the orthogonal property. This resulted in a set of m ordinary differential equations, $m = 0, 1, ..., \infty$. For each Fourier number, m, a set of linear algebraic equations was generated by using a finite difference approximation. Combining the boundary conditions with the finite difference equations resulted in a linear, matrix eigenvalue problem. The eigenvalues found corresponded to the square of the natural frequency, and when a zero eigenvalue resulted, wrinkling was assumed to have occurred. An equivalent method of prediction was to compute a zero determinant for the finite difference coefficients. Adams' results showed that the axisymmetric transverse displacements could give rise to compressive circumferential stresses which become large enough to induce wrinkling. The use of nonlinear membrane theory would give wrinkling when the circumferential stress goes to zero.

1.3 The Present Study

The information in the literature has shown that the finite element method has been successfully applied to the analysis of metal forming operations. In addition, the method has also been used in the prediction of wrinkling in circular plates. Therefore, rather than attempting to use trial and error methods or develop a closed form solution, the finite element method will be used in the present work as a means for determining the stress state and the deformation modes of the cylinder during the swaging process.

Before building the mathematical models necessary to simulate the necking pro-

cess with the finite element method, it would be useful to make some initial simplifying assumptions about the operation. Thus an examination of the physical process of swaging a cylinder was initiated to determine which parameters have the greatest impact on the formation of wrinkles. These variables will be classified as primary parameters, as their omission from computational analysis would render any results meaningless. A second classification would contain those parameters which contribute to the deformation response of the cylinder as it is formed, but do not directly contribute to the wrinkling phenomena. That is the wrinkling will occur for any value of the secondary parameters within the range of interest, and their omission from any analysis will not alter the numerical results or the conclusions based thereon.

In the current study, the primary parameters are identified as:

- 1) geometry of the can diameter, thickness, and final shape;
- 2) material properties elastic and yield moduli, anisotropy, and plastic flow;
- 3) tool geometry contact conditions;
- 4) forming steps path dependency of the response.

The secondary parameters are:

- 1) rate of the forming process material strain rate dependency;
- 2) friction tangential interaction between the tool and the cylinder;
- 3) lack of axisymmetry presence of weld seam and microstructural imperfections;
- 4) elastic snap-back release of stored energy after the forming process.

In addition to the above assumptions, an analysis of the swaging process requires a computational model that accurately accounts for large deformations, large strains and rotations, nonlinear material behavior, rate-independent elastic-plastic material model, and contact conditions, an algorithm for tracing the contact conditions between the tool and the cylinder at all stages of the forming process. The complexity involved in formulat-

ing a fully operational program for each of these situations leads to the use of a commercial finite element code for the analysis of the forming problem. Two programs from MARC Analysis Research Corporation were well suited for this task, Mentat II and MARC version K6.1 (Mentat II, 1994 and MARC, 1994)

Using Mentat II, the geometry and parameters for the mathematical models of all the occurring phenomena can be generated. These models are then translated into input for the analysis program, MARC. MARC reads the input created by Mentat II, processes the information, and calculates results for the unknown variables. These solutions are then read back into Mentat II wherein they may be plotted in several manners. Most often the results will be plotted as bands of color on the geometric model of the cylinder, with a range of values being assigned a different color. In this way it will be possible to visualize the levels of stress and strain within the cylinder as it a passes through the forming process.

Chapter 2

Modelling of the Swaging Operation

2.0 Introduction

Simulation of the swaging process involves the creation of a computational model to approximate the behavior of the cylinder during deformation. Therefore the domain of the problem is defined by constructing a geometric model of both the cylinder and the forming tools. The continuous region constituting the cylinder will then be discretized into a set of elements and the deformation of each element approximated using the finite element method. The selection of the element to be used for this purpose is the subject of some scrutiny. While several elements are available to model the cylinder, not all will provide accurate results for a reasonable level of computational cost. Once an element has been chosen the mechanical properties must by applied to the model. This includes not

only the elastic properties, but also the definition of material behavior after yielding. In addition to geometric and material properties, the conditions which exist in the cylinder prior to swaging (the initial stresses due to rolling the flat sheet into a cylinder) and the known conditions at the boundaries must also be applied to the model in order to calculate adequate results. Finally, the contact conditions of the problem, such as which bodies may come into contact and the motion of the forming tools, are required as well. The accuracy of the solution obtained is dependent on the quality of the definition of each of these components because each contributes to the final result.

Once the model has been completed, the nonlinear nature of the problem forces the need for a special solution algorithm. Usually the load-deflection relationship is linearized and solved using the Newton-Raphson algorithm. The resolution of the linearized curve is determined by the number of loading steps requested. Additionally, the accuracy of each step in the solution will be tested with a convergence criteria and specification of the degree of accuracy required. Finally, the large deformations involved in the necking process necessitate the definition of a coordinate system to locate the material points as the model of the cylinder is deformed.

2.1 Geometric Model of Cylinder and Forming Tools

The initial step in modelling the problem was to establish the geometry of the cylinder. For the purposes of this study the physical dimensions used for the cylinder were given as:

$$ID = 2.581 \text{ in.}$$
 $h = 0.007 \text{ in.},$ (2.1)

where ID is the inside diameter of the cylinder and h is the thickness of the material. How-

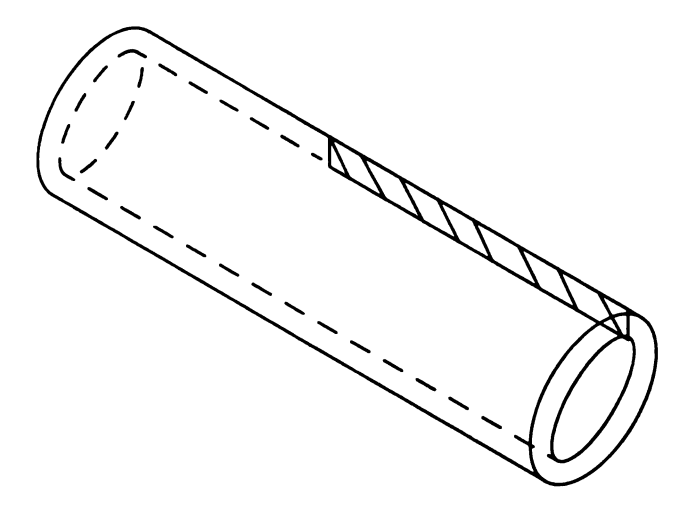


Figure 2.1 Relationship Between Modelled Surface and Full Cylinder.

ever, it was not necessary to model the fully three dimensional cylinder. Because the geometry, the applied load, and the deformation response were all axisymmetric, the cylinder and the subsequent models for the forming tools were represented by simple geometric entities. In the case of the cylinder, the geometry consisted of a surface created by slicing the cylinder along its length and using the cross-sectional plane which made up the wall thickness. The cross hatched region in Figure 2.1 shows the modelled surface and its relationship to the fully three dimensional cylinder. Only a small portion of the length was modelled because the region in which wrinkling occurs is rather small in comparison to the entire length of the cylinder. Thus, the deformations due to the forming occur only at some finite distance from the necked region, which is approximately 0.7 inches in this case.

The desired diameter reduction was to be achieved in two successive forming stages by similar operations. In each stage the tool moves toward the cylinder and upon

contact between the tool and the cylinder, the leading edge of the cylinder was pushed down to a new diameter, contained in a region called the "alley". While each tool operates in an analogous fashion, different levels of diameter reduction result from them.

The ramp of the first stage tool was established at 30 degrees from horizontal, measured clockwise, and the diameter of the cylinder was reduced 5.73%, or until *ID*= 2.4330 in. The final diameter of 2.367 in. was realized through the use of a 35 degree ramp from horizontal. Each of these rigid dies is represented as a set of bold lines in Figure 2.2, the first stage being on the left and the second on the right. Also shown in Figure 2.2 for reference are the cylinder, the cross hatched region, and the centerline of the geometry, the dashed lined. The actual model as created by the MENTAT program is displayed in Figure 2.3. Here the surface representing the cylinder is in black and the dies are presented in red with the first stage tool above the second stage tool. Again the center line of the geometries is given for reference.

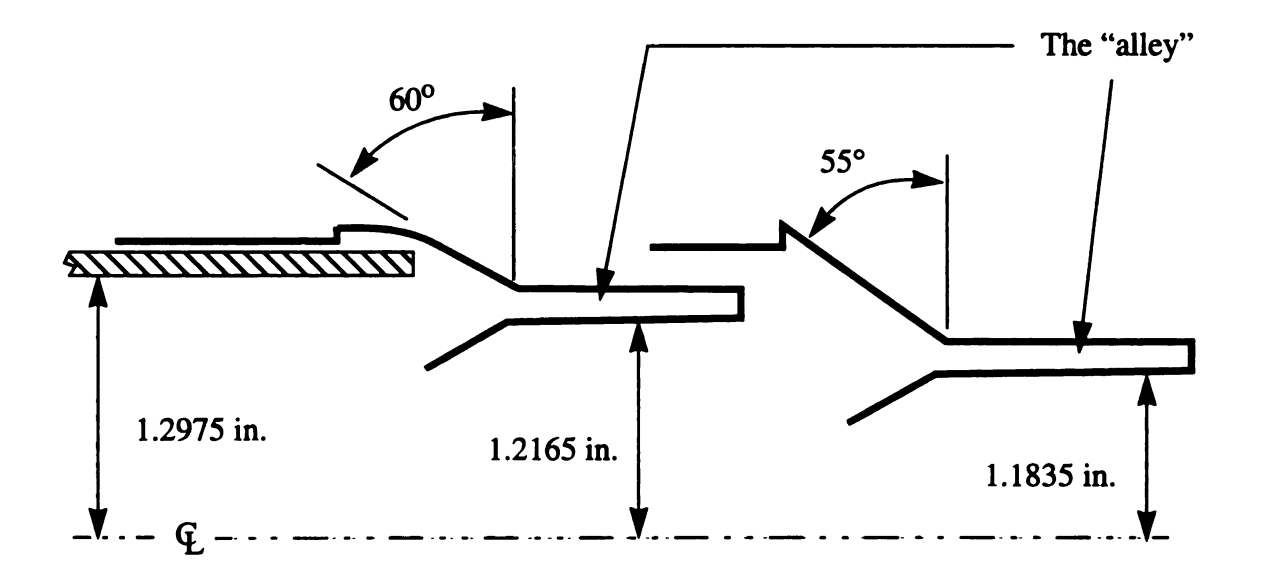


Figure 2.2 Geometry of Forming Tools with Reference to the Cylinder Axis. (Not to scale)

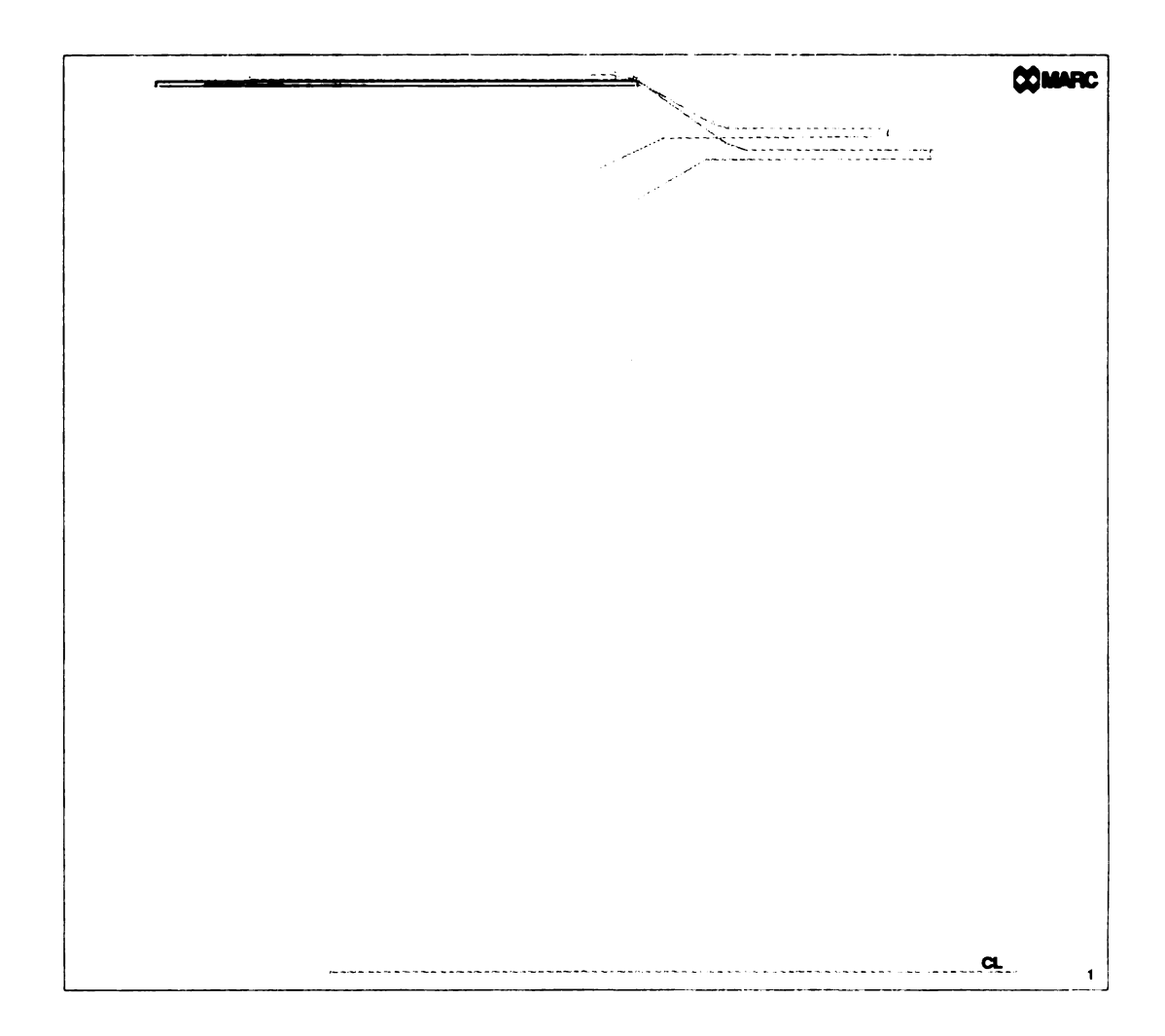


Figure 2.3 MENTAT Model of Cylinder and Forming Tools.

2.1.1 Preliminary Element Selection

An important step in the modelling process was the selection of an appropriate finite element which would allow for the most accurate results at an efficient computational cost. Inspection of the geometry and the deformation modes of the process helped in the identification of a limited group of appropriate elements. The reliability and efficiency of each was then estimated by using each of the appropriate elements to model problems with known solutions. The problem of reducing the diameter or necking of a thin-walled cylinder requires an axisymmetric element which can be subjected to bending. Given this criterion two groups of MARC elements were tested in a series of validation problems. Table 2.1 shows a simple schematic and gives relevant information for both groups of elements under consideration.

The first group contained axisymmetric, quadrilateral isoparametric elements. The kinematics of the elements are based on a continuum theory. Only two DOF are required to describe the deformations, axial displacement along the generator axis and radial displacement perpendicular to the generator axis. The behavior of each element in the group is governed by the interpolation of the displacement field and the number of integration or Gauss points used for numerical integration. Element 10 consists of four corner nodes and four integration points, which gives two point integration through the thickness of the element. In contrast, element 28 has nine integration points, three through the thickness, and assumes a quadratic displacement field. In addition, because element 28 consists of four corner nodes and four midside nodes, it has twice the number of degrees of freedom per element, 16, when compared to element 10, which contains 8 dof. Finally, element 116, like element 10, uses a linear displacement assumption, but the number of

34 **Table 2.1 MARC Elements**

Element	Topology / DOF	Attributes
10	U, V	 - Axisymmetric - Bilinear displacement interpolation - 2 x 2 Gaussian integration
28	U, V	 - Axisymmetric - Biquadratic displacement interpolation - 3 x 3 Gaussian integration
116	U, V	 Axisymmetric Bilinear displacement interpolation 1 point Gaussian integration with hourglass control
1		 Axisymmetric Linear displacement interpolation 1 point Gaussian integration Simpson's rule integration through the thickness
89	в в U, V, Ф	 Axisymmetric Quadratic displacement interpolation 1 point Gaussian integration Simpson's rule integration through the thickness

integration points has been reduced to one and hour glass control has been added. (More information on the meaning of these two aspects of element 116 will follow.)

The second group of elements included element 1 and element 89. Both elements are also axisymmetric and isoparametric, but, in contrast to the previous group, the kinematics are based on first order shear deformation shell theory (FSDT). The FSDT assumes that planes originally straight and normal to the midplane remain straight but not necessarily normal during deformation. This assumption allowed for inclusion of the shear deformations which may arise. The displacement field was then be approximated using three DOF at each node, axial and radial displacements and a right hand rotation in the plane. Again the behavior of the elements is governed by the displacement field interpolation and number of integration points along the length. Element 1 uses a linear shape function with one integration point and element 89 uses a quadratic interpolation and a two point integration rule. For both of these elements the integration through the thickness is carried out using Simpson's rule based on a user specified number of points or shell layers determined by the type of problem to be analyzed. At this time, the number of layers was set to three.

2.1.2 Evaluation of Element Performance for a Linear Problem

Given this set of eligible elements, the validity of each may be verified through the comparison of results obtained for simple problems using these elements to those from closed form solutions to the same problems. Therefore, each element was used to model a test case of an infinitely long cylinder subjected to a circumferentially distributed line load of unit magnitude. The data required for modelling the test case includes Young's modulus and Poisson's ratio of the material and the radius and the thickness. Because some finite

length must be declared in order to use the finite element method, a finite cylinder was modelled with sufficient length that the displacements near the ends were neglible. Additionally, it was appropriate to apply simply supported boundary conditions to the end points of the finite cylinder. Two sets of geometric data were used to generate the model, one being a moderately thick-walled cylinder:

$$R = 1.0 \text{ in.}$$
 $h = 0.1 \text{ in.}$ $L = 100.0 \text{ in.}$ (2.2)

where R was the radius, h was the thickness, and L was the length of the cylinder. The second set of data was representative of a thin-walled cylinder with the following geometry:

$$R = 5.0$$
 in. $h = 0.05$ in. $L = 300.0$ in. (2.3)

The material properties were the same for each of the cases:

$$E = 6.895 \times 10^{10} \text{ Psi} \qquad v = 0.3$$
 (2.4)

where E was Young's modulus and v is Poisson's ratio. After obtaining approximate linear solutions from MARC, the results were normalized to the closed form solution developed for a thin-walled cylinder based on FSDT (Reddy, 1984) given by

$$u_3(max) = -\frac{QR^2\beta}{2Eh} \tag{2.5}$$

where $u_3(max)$ was the maximum radial deflection, Q was the magnitude of the circumferentially distributed line load, R was the radius of the cylinder, E was Young's Modulus, h was the thickness, and β was a parameter defined by

$$\beta = \left[\frac{3(1 - v^2)}{R^2 h^2} \right]^{1/4}.$$
 (2.6)

Using a load of $1.0/2\pi$, the maximum deflection for the thick-walled cylinder was calculated to be -4.8072×10^{-11} in., while the thin-walled cylinder had a maximum deflection of -2.9745×10^{-10} in. The normalized MARC results for the thick cylinder are shown in Table 2.2 and the results for the thin cylinder are in Tables 2.3. In all cases the advantage of symmetry was taken to reduce computational times.

2.1.3 Discussion Results for a Linear Problem

A discussion of the results obtained from the MARC analysis of the test problem requires an examination of the assumptions that were involved in the formulation of the elements and the closed form solution. The closed form solution was based on FSDT. Thus any result obtained using Equation 2.5 was approximate. Since the normalizing solution was based on shell theory, one would expect elements 1 and 89 to have better agreement with the closed form solution because of the consistency in formulation. Elements 10, 28, and 116, being based on a continuum theory may not converge exactly to

Table 2.2 Predicted maximum deflection due to a circumferential line load in a simply supported cylinder of radius = 1.0 in., thickness = 0.1 in., and length = 100.0 in. All values are normalized to the closed form solution.

Mesh Size (with symmetry)	Element 10	Element 28	Element 116	Element 1	Element 89
50 x 1	0.4458	0.6689	0.6555	1.0321	1.0285
50 x 2	0.4462	0.6683			
100 x 1	0.6020	0.8499	0.8782	1.0321	1.0285
200 x 1	0.7666	0.9810	0.9776	1.0321	1.0285
200 x 2	0.6027	0.9817		********	
400 x 1	0.8861	1.0063	1.0021	1.0321	1.0285
600 x 1	0.9208	1.0103	1.0009	1.0321	1.0285
600 x 2	0.8559	1.0215			
750 x 1	0.9312	1.0142	1.0193	1.0321	1.0285
1000 x 1	0.9387	1.0180	1.0301	1.0321	1.0285

the results given by Equation 2.5 for thick shells, but should approach the same results for thin shells.

Examination of the results for elements 1 and 89 in Table 2.2 showed good correlation with the closed form solution, with the error for each being approximately 3 percent. In comparison, substantial mesh refinement was required for the continuum elements to converge. Using the 50 x 1 mesh size as a baseline, elements 28 and 116 required an increase of about four times as many elements, while twenty times the number of elements were necessary for convergence of element 10. Despite the need for an

Table 2.3 Predicted maximum deflection due to a circumferential line load in a simply supported cylinder of radius = 5.0 in., thickness = 0.05 in., and length = 300.0 in. All values are normalized to the closed form solution.

Mesh Size (with symmetry)	Element 10	Element 28	Element 116	Element 1	Element 89
50 x 1	0.1833	0.2786	0.4101	1.0032	1.0032
50 x 2	0.1833	0.2786	*****		
100x1	0.2499	0.4365	0.6695	1.0032	1.0032
200 x 1	0.3438	0.6986	0.8760	1.0032	1.0032
400 x 1	0.4762	0.9116	0.9659	1.0032	1.0032
750 x 1	0.6235	0.9839	0.9921	1.0032	1.0032
750 x 2	0.6267	0.9850		**********	
1250 x 1	0.7494	0.9981	0.9989	1.0032	1.0032
1500 x 1	0.7896	0.9998	1.0001	1.0032	1.0032
2000 x 1	0.8396	0.9996	1.0012	1.0032	1.0032
2000 x 2	0.8562				

increased number of elements, 10, 28, and 116 did provide acceptable solutions to the test problem. Examination of the results for the thin-walled case should provide a better understanding of the behavior of the elements for the diameter reduction problem as it too is thin-walled problem.

In Table 2.3 the shell elements again quickly converged to the result of Equation 2.5. Also as before, the mesh had to be refined in order for elements 10, 28, and 89 to approach convergence, with elements 28 and 116 continuing to yield results nearly corresponding to the analytical result. On the other hand, element 10 required a far greater

number of elements to converge and the final results obtained (200x2 mesh) were still in error by approximately 15 percent. The large error may be a result of the element experiencing locking and/or the size aspect ratio of the element.

Locking may be understood by considering the case of a thin beam subject to pure bending. For a situation such as this the transverse shear and membrane energies should be negligible throughout the element. However, the element approximation may not be able to satisfy the kinematic constraints of vanishing shear and membrane strains and also adequately represent the bending strains. As a result, the element may be too stiff and not converge. The most prevalent method for eliminating locking is to use fewer Gauss integration points than the minimum required for exact integration of the energy quantities, thereby relaxing the constraints in the element and allowing the bending energy to control the deformation (Averill and Reddy, 1990). One drawback to this solution technique is that a singular or nearly singular stiffness matrix may result which will cause large deformations to appear without any change in strain energy, a so-called zero energy or hourglass mode. Control of these modes may be attained by adding a small amount of stiffness, akin to adding springs, to their contributions in the coefficient matrix of the model. However, insufficient stiffness will not prevent the spurious energy modes, while too much will prevent viable modes from being found. Element 116 has been derived using both reduced integration and hourglass control, thereby presenting a viable alternative to element 10 which exhibits locking. While element 116 mandated more elements for convergence than the standard mesh, by a factor of 8, the increase in mesh size was manageable and the error for a mesh of this size was less than four percent.

Another solution to the problem of element locking is to increase the number of

DOF within the model. Two ways of doing this were available: a) increase the elements in the mesh or b) use an element with a higher order interpolation scheme. As can be seen from the results in Tables 2.2 and 2.3, the mesh refinement technique seemed to be working, though a converged solution was not yet attained using element 10 for these two cases. Use of element 28 increased the DOF in the analysis by increasing the interpolation order. Once again the table shows that a greater number of elements were needed to model the cylinder (about fifteen times more) than the benchmark, but the converged result was less than two percent in variance with the normalizing result.

The size aspect ratio, the length of the element divided by the height, also contributed to the failure of element 10 to converge. In the thick-walled case the 50 x 1 mesh resulted in an aspect ratio of 10, meaning the element length was 10 times longer than its height. Thus, to achieve the desired deflection the element was required to bend while experiencing very little shear. This was in contrast to the case of the 100x1 mesh, where the minimum aspect ratio was one half and shearing was the dominant mode of deformation. So, the mesh of 1000 x 1 converged to the closed form solution because the shear was not forced to vanish. The maximum and minimum aspect ratios in the thin case were 60.0 and 1.5 respectively. In both cases the bending energy was governing the deformation of the elements and, thus, locking was a consequence. Keeping the aspect ratio close to one or less, the phenomena of locking may be relieved. In order to confirm this hypothesis a third test case was run.

In this final case the same material properties as before were used and the geometry was as follows:

$$R = 100.0$$
 in. $h = 1.0$ in. $L = 200.0$ in. (2.7)

This geometry allowed greater flexibility in creating meshes with the aspect ratio of one. The analytical solution was again calculated using Equation 2.5 and found to be 1.4835x10⁻¹¹ in. Because elements 1 and 89 did not exhibit any difficulties in converging, only elements 10, 28, and 116 were used in modelling this second thin walled case. Of course both elements 28 and 116 did converge to the normalizing solution, but the hope was that by maintaining the aspect ratio as close to one as possible, these elements would converge faster. The results from the MARC analysis are given in Table 2.4. As expected element 10 did converge to the normalizing solution. Also, as was expected, elements 28 and 116 both converged to the analytical solution at a faster rate. Actually, they converged with the initial mesh. The results obtained indicated that the effect of the aspect ratio was significant and should be kept to a value of 1.0 or less.

Table 2.4 Predicted maximum deflection due to a circumferential line load in a simply supported cylinder of radius = 100.0 in., thickness = 1.0 in., and length = 200.0 in. All values are normalized to the closed form solution.

Mesh	Element 10	Element 28	Element 116
100 x 1	0.8989	1.0041	1.0046
200 x 1	0.9717	1.0049	1.0043
400 x 4	0.9961	1.0050	1.0048
800 x 4	1.0000	1.0050	1.0048

2.1.4 Nonlinear Evaluation of Element Performance

The ability of element 10 to represent the kinematics of a thin structure was still in question and the decision was made to test this element in a nonlinear situation. So a nonlinear test case was devised using the same geometry as given in Equation 2.7, but with L=100.0 and the following material properties:

$$E_{11} = 3.230 \times 10^7 \text{ Psi}$$
 $E_{22} = 2.72 \times 10^7 \text{ Psi}$ $E_{33} = 2.72 \times 10^7 \text{ Psi}$ $v_{12} = 0.3$ $v_{13} = 0.3$ $v_{23} = 0.3$ $G_{12} = 1.242 \times 10^7 \text{ Psi}$ $G_{13} = 1.242 \times 10^7 \text{ Psi}$ $G_{23} = 1.242 \times 10^7 \text{ Psi}$ $G_{24} = 1.242 \times 10^7 \text{ Psi}$ $G_{25} = 1.242 \times 10^7 \text{ Psi}$

where $E_{\alpha\alpha}$ are the Young's moduli, $G_{\alpha\alpha}$ are the shear modulus and σ_y is the yield stress. The subscripts given refer to the direction in which the property is valid. The 1 direction was defined to be parallel to the axis of the cylinder, 2 was in the circumferential coordinate, and 3 was parallel to the radial direction. In order to keep the computational times to a minimum plasticity was not included in this test case. A compressive circumferential line load of 4.5×10^6 pounds was applied to one end of the cylinder in the model. This load was chosen as it would provide for approximately the same amount of diameter reduction as in the swaging process under study. Also, because this problem was to be solved nonlinearly, Equation 2.5 was no longer valid and no other closed form solution was readily available. Hence the converged result of element 28 was chosen to serve as the normalizing solution for this case due to its previously demonstrated ability to converge. Table 2.5 contains the values obtained for this validation problem.

Table 2.5 Nonlinear test case results corresponding to the predicted maximum deflection due to a circumferential line load in a simply supported cylinder of radius = 100.0 in., thickness = 1.0 in., and length =100.0 in. All values are normalized to the converged solution of element 28.

Mesh	Element 10	Element 28
100 x 1	0.3078	0.9451
200 x 2	0.6322	0.9811
400 x 4	0.9498	1.0000
800 x 8	0.9537	

The data attests to the fact that element 10 will indeed converge in a nonlinear analysis. This, coupled with earlier information from the other test cases, indicates that any of the elements tested would be suitable for use in the forming process, but other information helped to eliminate some elements from further consideration.

One of the major features of the MARC finite element code is the ease in which the user can define contact bodies and conditions. Potential contact bodies are identified by the user, and the code internally defines the contact constraints. However, this algorithm does not detect contact at midside nodes, thus eliminating higher order elements from contact analysis. Elements 28 and 89 were, therefore, not eligible to be used in the analysis of the forming problem as the topology of these elements includes midside nodes. This left elements 10, 116, and 1 as the remaining possibilities. Each of these elements had capabilities as well as insufficiencies for use in forming problems. One drawback to element 116 was the reduced integration technique which provides only one Gauss point

within the element. Because the strains and stresses (and, hence, the elasto-plastic material properties) will vary from the outer surfaces inward, a single integration point through the thickness would not adequately predict the variation of these values through the thickness of the cylinder. It then becomes necessary to increase the number of elements in the transverse direction to gain more Gauss points. In contrast, Element 1 allows the user to input the number of points to use for Simpson's integration rule through the thickness, eliminating the need for multiple elements in the radial direction. The final decision of which element to use was left until each could be used in the necking analysis.

2.2 Boundary Conditions and Contact Constraints

2.2.1 Boundary Conditions

Some values of the primary degrees of freedom must be known on the boundaries of the cylinder in order to constrain rigid body motions. Therefore, the next step in the modelling process was to establish boundary conditions for the model. For the solution of the diameter reduction problem, it was appropriate to fix the axial displacements on the end opposite the necked region to zero. In doing so the continuity requirements between the modelled and unmodelled portions of the cylinder were satisfied. Since transverse displacements are constrained by the axisymmetric response of the cylinder and none of the elements under consideration have the ability to deform in the circumferential direction, this was the only boundary condition needed for the solution of the forming problem. The applied boundary conditions are illustrated in Figure 2.4 by the arrows located on the left hand end of the cylinder.

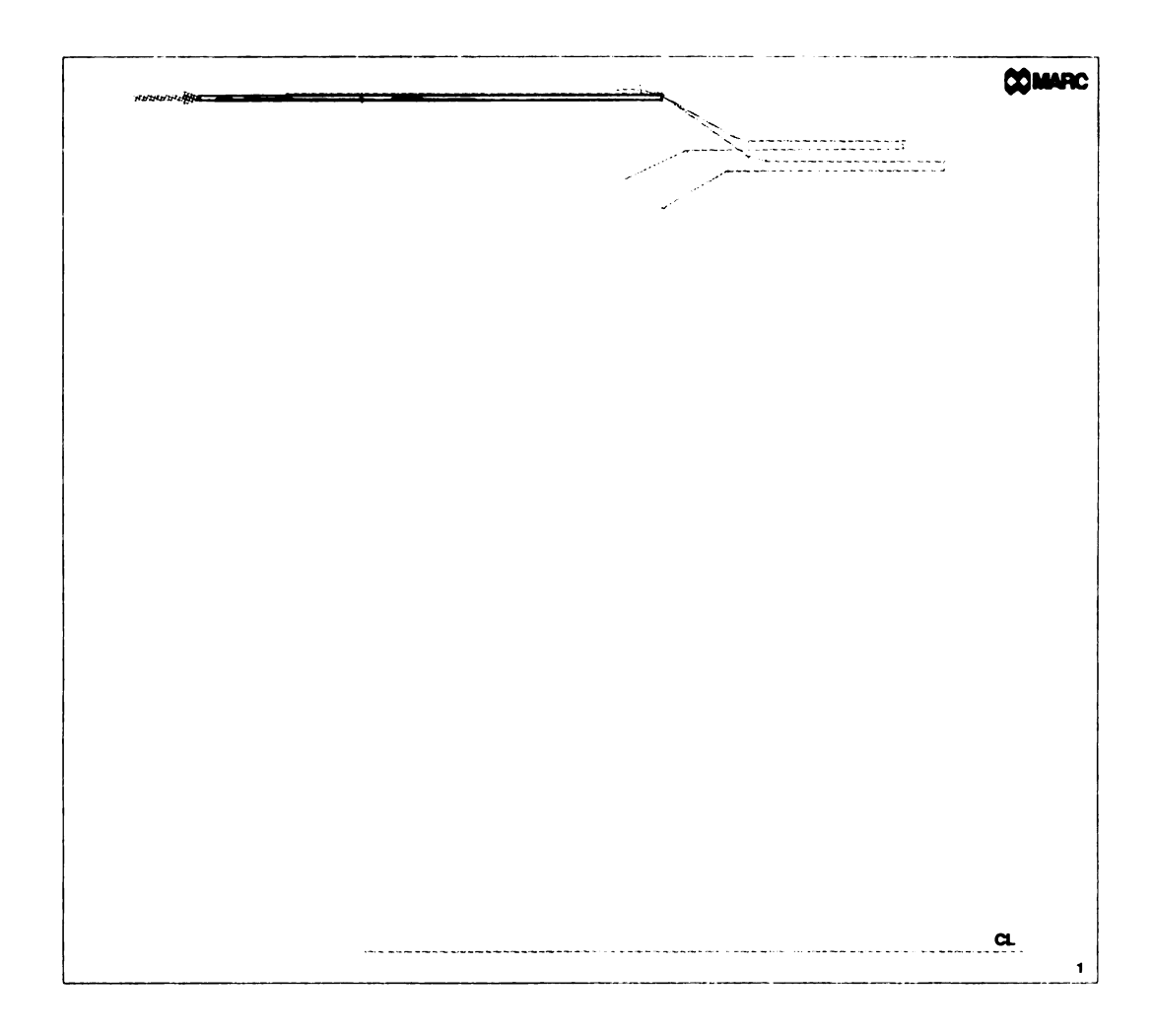


Figure 2.4 Geometric Model with Applied Boundary Conditions.

2.2.2 Initial Stresses

Prior to the actual forming process, the cylinder had a pre-existing state of stress due to the rolling of a flat sheet into a cylinder. These effects were also included in the model. It was assumed that the bending was the result of equal yet opposite moments being applied to the edges of the plate resulting in a state of pure bending and, hence, an exact elastic-plastic solution could be obtained. The effects of anticlastic curvature were, however, neglected. For elastic or plastic deformations, the circumferential strain in the cylinder after bending was obtained from geometric considerations as:

$$\varepsilon_{\theta\theta} = \frac{\bar{z}}{R} \tag{2.9}$$

where R=1.294 in. was the mean radius of curvature of the cylinder and \bar{z} was the distance from the midplane of the cylinder. Of course, the maximum strain occurred at $\bar{z}=\pm\frac{h}{2}$ and was equal to 0.0027, which exceeded the yield at:

$$\frac{\sigma_{\gamma P\theta}}{E_{\theta\theta}} = 0.00227 = \varepsilon_{\gamma P\theta} \tag{2.10}$$

where $\sigma_{YP\theta}$ was the yield stress in the circumferential direction, $E_{\theta\theta}$ was the elastic moduli in the same direction, and $\varepsilon_{YP\theta}$ is the yield strain. While some plasticity would be evident in the cylinder, the entire cross-section would not yield due to bending. Rather, there would exist an elastic core near the midplane of the flat sheet and yielding would occur

near the edges of the plate, with the plastic zone increasing toward the midplane as curvature was increased. In the final configuration, the elastic core extended a distance \bar{z}_{el} away from the midsurface found by:

$$\bar{z}_{el} = \frac{\sigma_{YP\theta}}{E_{\theta\theta}}R = 0.00294 \text{ in.}$$
 (2.11)

and illustrated in Figure 2.5 in which the cross section of the cylinder is shown with the distribution of stresses resulting from bending the flat sheet.

Determination of the limits of the elastic core was important in that MARC does

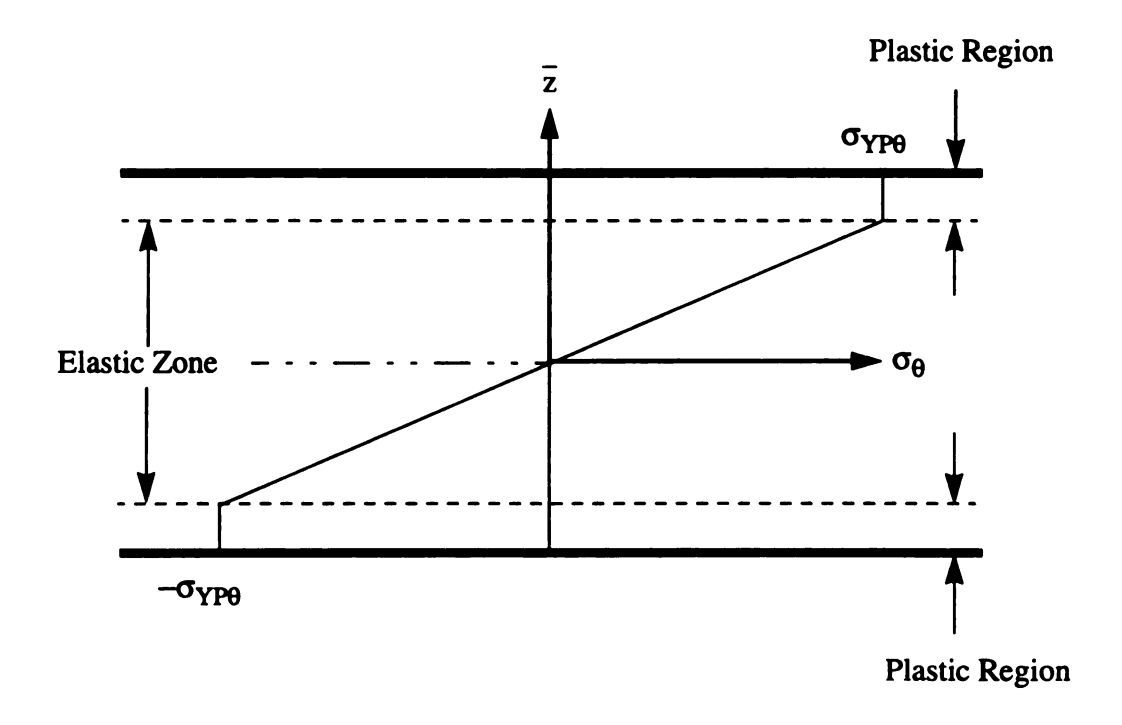


Figure 2.5 Cross Section of Cylinder with Stress Resulting from Cylindrical Bending.

not allow the initial stresses to exceed the elastic yield limit of the material. Being that the initial stresses must be input at the Gauss points of each element, it was important to ensure that the stress at these points did not exceed the yield stress. Thus, the coordinates of the Gauss points in reference to the inner diameter of the cylinder needed to be determined. Using this information the \bar{z} coordinate of each was also found with

$$\bar{z} = y(GP) - \frac{h}{2} \qquad (2.12)$$

where y(GP) was the coordinate of the Gauss point measured from the inner diameter of the cylinder and h was the cylinder thickness.

Initial stresses were determined in the following manner. From the bending strain found in Equation 2.9, the stresses at $\bar{z} = \pm \frac{h}{2}$ were found using the one dimensional Hooke's Law,

$$\hat{\sigma}_{\gamma P\theta} = E_{\theta\theta} \varepsilon_{\theta\theta} \tag{2.13}$$

where $\hat{\sigma}_{\gamma P\theta}$ was the calculated yield stress in the circumferential direction. Finally, assuming a linear distribution of stress through the thickness, and using the results from Equations 2.12 and 2.13, the stress at the Gauss points was found using:

$$\sigma(GP) = \frac{\hat{\sigma}_{\gamma P\theta}}{h/2}\bar{z} \tag{2.14}$$

where $\sigma(GP)$ is the stress at the Gauss point. In the event that the Gauss point fell within the plastic zone, the initial stress value was assumed to take on the value of stress at the elastic/plastic interface.

An alternate method of calculating the initial stresses would have been to assume a linear distribution through the elastic region of the cylinder and having the stress in the plastic zone maintain the stress value at the elastic/plastic interface. Employing this scheme would have resulted in a more accurate model of the initial stresses and a 16 percent increase in their magnitude. The results to be presented later will show that either approach does not significantly impact the final results of the model. In either case, the input of this data into the model results in circumferential stresses being present at the outset of analysis.

2.2.3 Contact Conditions

Using MARC, the user is able to define a deformable body through the definition of a set of finite elements and a rigid body is defined as a set of geometrical entities, such as lines, circles, splines, or surfaces.

In many commercial finite element codes, contact is defined by placing gapfriction elements between the two bodies that may come into contact during the analysis. The difficulty in this method is that the user is required to know a priori which bodies come into contact. While this approach is valid in MARC, another option is also available to automate the contact definition procedure. The basic thrust behind the option is the definition of bodies rather than gap elements. All the required information to enforce nonpenetration is contained on the surfaces of these boundaries. In the case of a deformable body, which is defined by a set of finite elements, all the nodes at the boundary become a set of candidate nodes for contact. For rigid bodies only the surfaces of potential contact need to be defined by a set of geometric entities, such as lines. As the analysis is performed, the contact condition is checked by calculating the vector product of the nodal displacements and the normal of the rigid body. If this result is less than or equal to the distance between the bodies contact is detected and constraints are applied to the contact nodes to prevent penetration. Because the distance between the deformable and rigid bodies is a calculated quantity, some round off error will be expected and lead to some penetration. To account for this phenomenon, a contact tolerance is provided to allow nodes to go an incremental distance below a surface and yet still be considered in contact. This may be a user defined quantity or assigned by the algorithm. For a continuum element, the default is 1/20 the smallest element edge and for a shell element it is 1/2 the element thickness. Finally the rigid body motion of the dies is given in the contact option by defining an instantaneous velocity. By explicitly integrating the velocity over time the motion path of the tools is provided (MARC, 1994).

For the swaging analysis the elements constituting the cylinder were classified as the deformable body and the forming tools declared as separate rigid bodies. The action of the forming process is such that the tools move toward the cylinder, so each rigid body defined was given a series of velocities to simulate their displacements. At the present time, displacements rather than velocities will be discussed with assumption that the time integration limits have been chosen properly to achieve the correct velocities. The first stage forming process was defined by applying an axial displacement of -0.3729 inches to the body defining the first stage tool. This die was then pulled off the cylinder by using a release option provided in MARC to decouple the nodes of the deformable body from the

rigid die in conjunction with a second rigid body translation of 0.4271 inches in the axial direction. Simulation of the swaging process was completed by the motion of the second tool. Initially the position of the tool relative to the cylinder was quite significant and would prevent the analysis from finding a converged solution. Therefore the first movement of the second stage was to bring the tool to a point just before contact would be detected. The required displacement was -0.1060 inches. Forming was done by then moving the die -0.2558 inches axially. This amount of movement was sufficient to bring the ramp of the tool into a position parallel with the previously formed angle in the cylinder. The process was completed by again using the release option with the 0.4271 inch translation of the tool.

2.3 Material Model

The response of the cylinder to the action of the forming is also dependent on the mechanical properties of the material used to construct the cylinder. Among these quantities are properties to describe the elastic response of the cylinder, but more important are the characteristics which dictate the behavior after the elastic limit has been exceeded.

2.3.1 Mechanical Properties

An elasto-plastic model was developed to describe the behavior of double-reduced tinplate sheet steel conforming to A.S.T.M. A-623 Type L, the material of choice in this analysis. The model began with the specification of the mechanical properties which are given in Table 2.6 (Wood, 1994). The in-plane values for Young's moduli and yield stress

were determined by averaging the results obtained from five samples used in standard tensile testing procedures. Given the thickness of the material, current experimental procedures were inadequate to measure the transverse material properties.

Table 2.6 Mechanical Properties of Double-Reduced Tinplate Steel, Type L.

Property	Axial, x	Circumferential, θ	Transverse, z
Young's Modulus, E (psi)	3.23x10 ⁷ in.	2.72x10 ⁷ in.	2.72x10 ⁷ in.
Poisson's ratio, v	0.3	0.3	0.3
Shear Modulus, G(psi)	1.242x10 ⁷ in.	1.242x10 ⁷ in.	1.242x10 ⁷ in.
Yield Stress, σ _{YP} (psi)	7.785x10 ⁴ in ⁻	6.544x10 ⁴ in.	6.544x10 ⁴ in.

Therefore, the shear moduli were calculated using,

$$G = \frac{E}{2(1+\nu)} \tag{2.15}$$

with E being given by the axial value of Young's modulus. This resulted in isotropic values for the shear moduli, in addition to the given isotropic values of Poisson's ratio. This assumption of isotropy in the shearing values will not lead to significant error. In fact, transverse shear effects are usually neglected in a structure with a radius to thickness ratio of greater than 20 (Dym, 1974). In this case the radius to thickness ratio is in excess of 180.

2.3.2 Plasticity Model

The definition of the plasticity model requires the yield stresses, a method for determining the onset of yielding (a yield surface), a definition of the hardening curve, and finally the effects of hardening on the yield criteria. The yield stresses are given in Table 2.6 and were found using the same tensile tests as used in finding the elastic properties. Since the cylinder was in a state of multi-axial loading during the simulation, a multi-axial yield criterion was required. Several models exist for this purpose, most notably among them is the von Mises yield criterion wherein the material is assumed to have yielded when the distortion energy is equal to the measured uniaxial yield stress (Mendelson, 1968). For an anisotropic material, the relationship of distortion energy to yield stress is given as

$$2\sigma_{YPx}^{2} = a_{1} (\sigma_{22} - \sigma_{33})^{2} + a_{2} (\sigma_{33} - \sigma_{11})^{2} + a_{3} (\sigma_{11} - \sigma_{22})^{2} . \qquad (2.16)$$
$$+ 3a_{4}\tau_{23}^{2} + 3a_{5}\tau_{31}^{2} + 3a_{6}\tau_{12}^{2}$$

where $\sigma_{\gamma Px}$ corresponds to the axial yield stress, σ_{ij} are the calculated stresses referred to the coordinate axes of the cylinder (11 - axial, 22 - circumferential, and 33 - transverse), τ_{ij} are the calculated shear stresses in the cylinder during analysis. The coefficients a_{α} , $\alpha=1$ to 6, account for directional variations in the yield stress from the axial and may be found by defining the Hill's yield ratios YRDIR1, YRDIR2, and YRDIR3 in conjunction with the following

$$a_{1} = \frac{1}{YRDIR2^{2}} + \frac{1}{YRDIR3^{2}} - \frac{1}{YRDIR1^{2}}$$

$$a_{2} = \frac{1}{YRDIR3^{2}} + \frac{1}{YRDIR1^{2}} - \frac{1}{YRDIR2^{2}}$$

$$a_{3} = \frac{1}{YRDIR1^{2}} + \frac{1}{YRDIR2^{2}} - \frac{1}{YRDIR3^{2}}$$

$$a_{4} = \frac{2}{YRDIR3^{2}} \qquad a_{5} = \frac{2}{YRDIR2^{2}} \qquad a_{6} = \frac{2}{YRDIR1^{2}}$$
(2.17)

where

$$YRDIR1 = \frac{\sigma_{YP_x}}{\sigma_{YP_x}}$$
 $YRDIR2 = \frac{\sigma_{YP_R}}{\sigma_{YP_x}}$ $YRDIR3 = \frac{\sigma_{YP_z}}{\sigma_{YP_x}}$ (2.18)

For double-reduced steel, YRDIR1=1.0, YRDIR2=0.8405, and YRDIR3=0.8405 were used.

After the material points in the cylinder reach the plastic region of the stress-strain curve, the material will begin to harden. The amount of hardening the material experiences must also be described through a mathematical model. Isotropic hardening, used in this model, allows the yield locus to retain its center point throughout the analysis, but the size of the locus will grow with increasing strain hardening. Inputting a table of plastic strain versus stress into the MARC data deck allowed the program to internally account for these effects. Table 2.7 contains the measured values for the double reduced tinplate sheet steel. When this data was plotted in a stress versus plastic strain curve, as in Figure 2.6, it was observed that the curve was nearly flat. This would indicate that the strain hardening will not have a significant impact on the results obtained for the model. Proof of this hypothesis will be left until the model has been completed and the analyses run.

Table 2.7 Stress versus Plastic Strain for Double-Reduced Tinplate Sheet Steel, Type L.

Stress	Plastic Strain	
7.7854x10 ⁴ Psi	0.0	
7.9024x10 ⁴ Psi	6.4000x10 ⁻⁴	
7.9727x10 ⁴ Psi	1.3700x10 ⁻³	
8.0079x10 ⁴ Psi	2.1900x10 ⁻³	
8.0109x10 ⁴ Psi	3.1000x10 ⁻³	

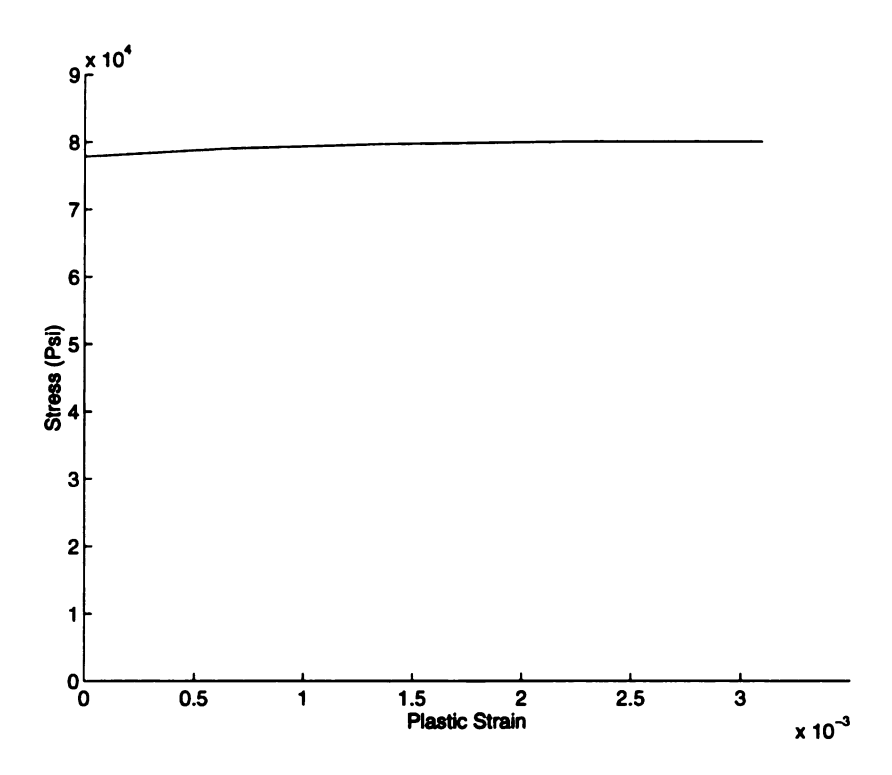


Figure 2.6 Stress versus Plastic Strain for Double Reduced Tinplate Sheet Steel.

2.4 Solution Parameters and Analysis Options

2.4.1 Solution Method

As previously mentioned, because the problem under consideration is nonlinear, the solution path is also nonlinear. In this case a method of tracing this curve was required in order to obtain solutions. Therefore, the Newton-Raphson method, which is one of several techniques, was employed to approximate a solution to the resulting nonlinear algebraic equations. The advantage of the Newton-Raphson method is that it provides a quadratic rate of convergence to the solution (Zienkiewicz, 1989). In order to understand the Newton-Raphson method, consider a fictitious load-deflection curve as shown in Figure 2.7. The desired load is given as P_C. In cases where the entire path must be known, such as in plasticity, the curve may be approximated by loading the structure incrementally. Within each load step the algorithm ensures the equilibrium by reaching the solution point in an iterative sequence which is terminated when some convergence criterion is satisfied.

Accordingly the motion of the forming tools was applied incrementally. Recalling the definitions of the tool motions in Section 2.2.3, the first stage tool has two separate translations, one onto the tool and the second a releasing action. In the Newton-Raphson solution the initial tool movement was divided into 250 equal load steps and the second was done in 2 unequal steps. The first increment of the releasing action was very small in order to ensure that the motion started in the correct direction and the second increment completed the releasing motion. For the second tool, three movements were given: bringing the tool near the cylinder, the forming operation, and the releasing action. The initial movement of the second stage tool was performed in one load step, the forming was

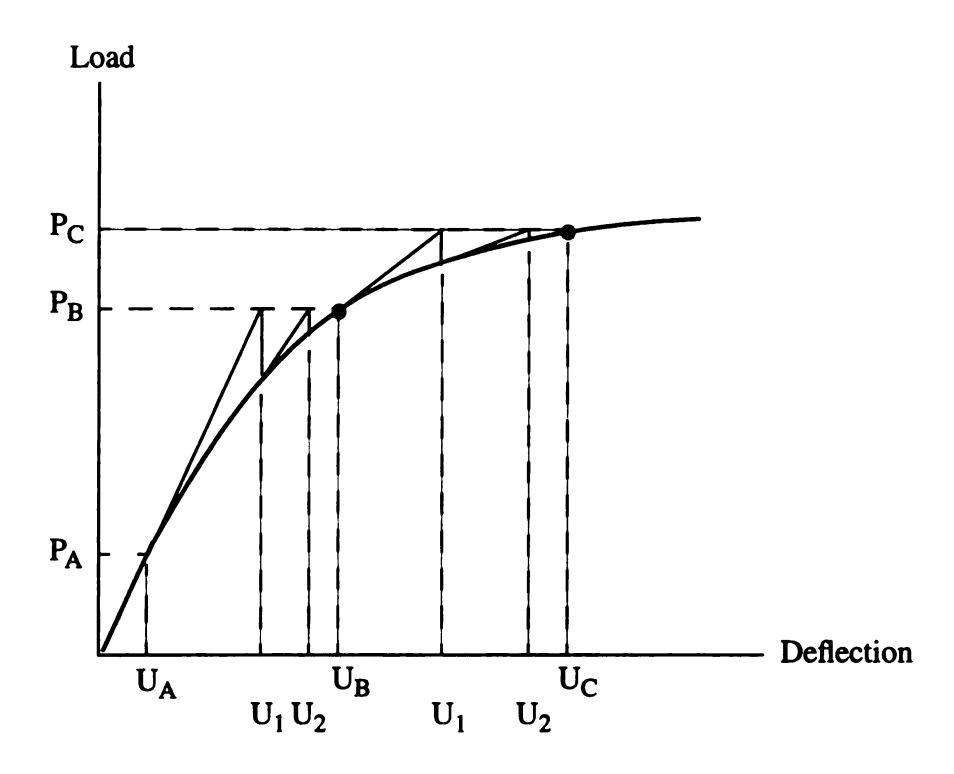


Figure 2.7 Newton-Raphson solution method.

again divided into 250 equal increments, and the releasing action also performed in two increments, one small and the other large enough to complete the requirements. Within all of the load increments a maximum of 20 iterations were allowed, but this was set as upper bound. After each iteration, the maximum displacement increment was divided by the maximum displacement change (for the load increment) within the model to calculate a convergence tolerance. When this tolerance was found to be less than or equal to 0.10 the increment was said to have satisfied the convergence criterion and the next load increment was begun. In the event that convergence was not achieved, upon reaching the end of the 20th iteration the program terminated giving a message that the convergence criterion was

not met. This leads to some comments about the number of load increments used. 250 increments was found to be a lower limit for convergence reasons. When a smaller number of increments was used, the load steps were too large for the algorithm to attain a converged result within the specified number of iterations. Using a greater number of increments could result in a more accurate solution, with the trade-off being increased solution time. Therefore, the initial simulations were done with 250 increments, but the effects of increased load steps on the solution were also investigated.

2.4.2 Analysis Options

The large deformations that are inherent in the process of swaging the cylinder required a reference frame from which the displacements may be measured. In addition, the particular measures of strain and stress that are to be used must also allow for the large deformation effects. MARC offers a set of options to account for this phenomenon, of which three were used in combination in the simulation model. These were the large displacement, finite strain plasticity, and updated Lagrange options. The first two cards account for the large deformations and strains as their names imply. The last option, updated Lagrange, gives a reference frame for the measurement of deformations and calculation of the stiffness matrix. Here the mesh is connected to the material throughout the analysis and is updated at the end of each load increment. By using these three options in combination the entire spectrum of large deformation were taken into account in the model. And with that the definition of the model for simulating the swaging process was completed. The forming process may now be analyzed and an understanding of the deformations and stress state of the cylinder during forming can be sought.

Chapter 3

Numerical Simulation of Swaging

3.0 Introduction

The model for the simulation of the swaging process has been described. Using this model preliminary deformations of the cylinder as it progresses through the process may be observed. The deformations are preliminary in that up to this point two rather important details have not yet been determined. The element that is to be used is yet to be finalized, with the remaining choices being elements 10, 116, and 1. In addition to the element decision, the size of the mesh is also a lingering question to this point. Upon making a decision about these components, the final deformations and stress state of the cylinder during and after the necking process may be analyzed. The information revealed may then be used to ascertain possible causes for the formation of wrinkles in the cylinder

and ultimately may lead to candidate solutions.

3.1 Simulation of the Swaging Process

Now that a model has been defined, the swaging process can be simulated. Although, it should be noted that the results shown are preliminary until final selection of an element and mesh size. Thus, a baseline mesh of 150 elements along the length and 2 elements through the thickness, or a 150 x 2 mesh, was used in concert with element 10 to produce the initial simulation shown in Figures 3.1 (a) through (i). In Figure 3.1(a) the cylinder and tools are shown at the zeroth increment of the simulation, before the forming operation had begun. As the first stage tool progressed forward, the leading edge of the cylinder was bent down and traveled along the tool ramp toward the "alley" as shown in Figure 3.1(b), the 50th increment of the simulation. Figure 3.1(c) depicts the leading edge of the cylinder as it was just being bent back into the "alley", increment 100, so that the diameter reduction of the first stage could be achieved. By the 250th increment, the leading edge had slid down the "alley" until the end of the tool was reached, as illustrated in Figure 3.1(d). Finally the first stage was completed as the tool was removed in the 252nd increment of analysis, as seen in Figure 3.1(e).

In Figure 3.1(f) the second stage tool has moved to a position near the cylinder so as to prevent numerical difficulties in attaining convergence, increment 253. The tool then pushed the cylinder's leading edge down until the "alley" was again reached at the 352nd increment of analysis, as shown in Figure 3.1(g). The advancement of the second tool was discontinued when the angled portion of the cylinder was parallel to the ramp of the tool

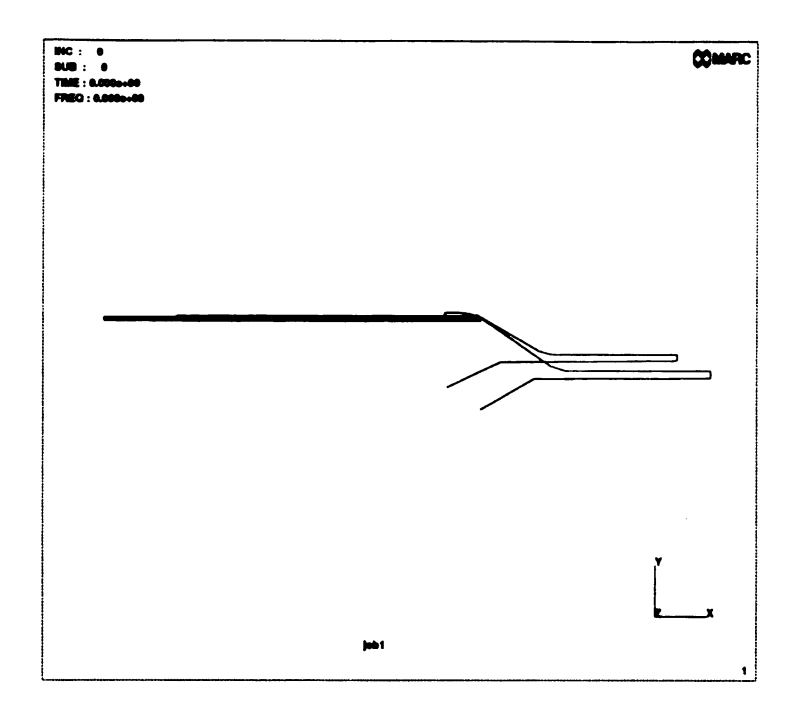


Figure 3.1(a) First Stage of Swaging at the Zeroth Increment.

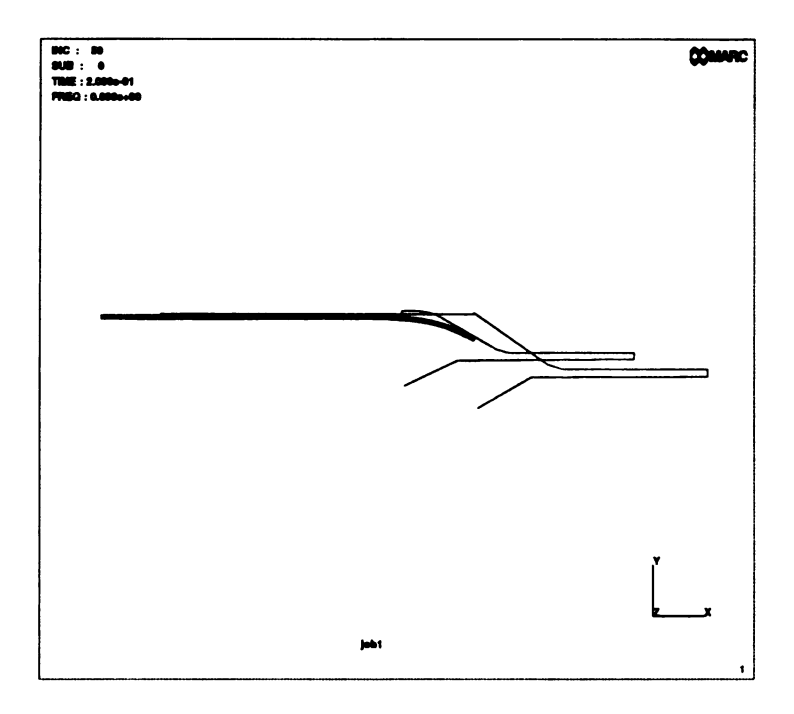


Figure 3.1(b) First Stage of Swaging at the 50th Increment.

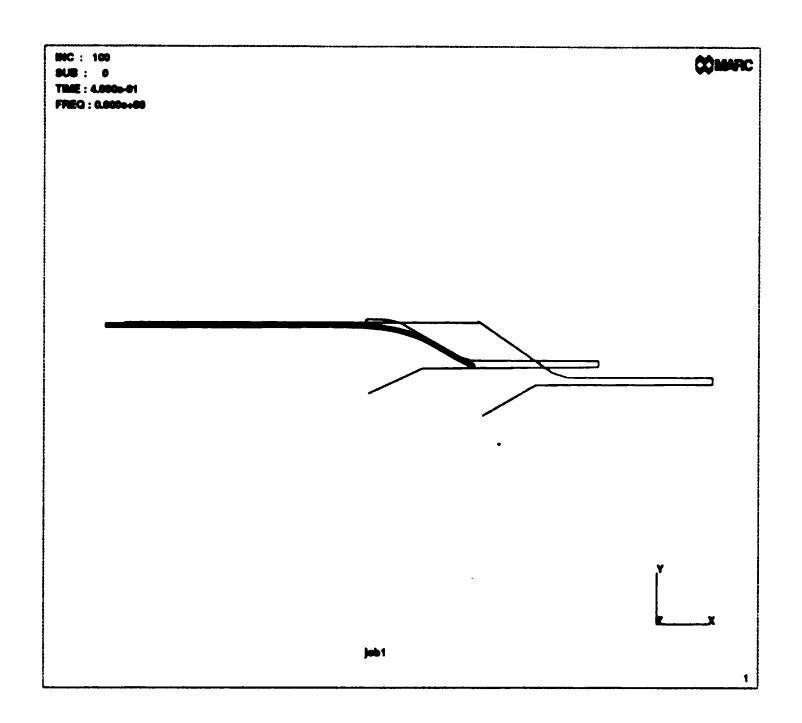


Figure 3.1(c) First Stage of Swaging at the 100th Increment.

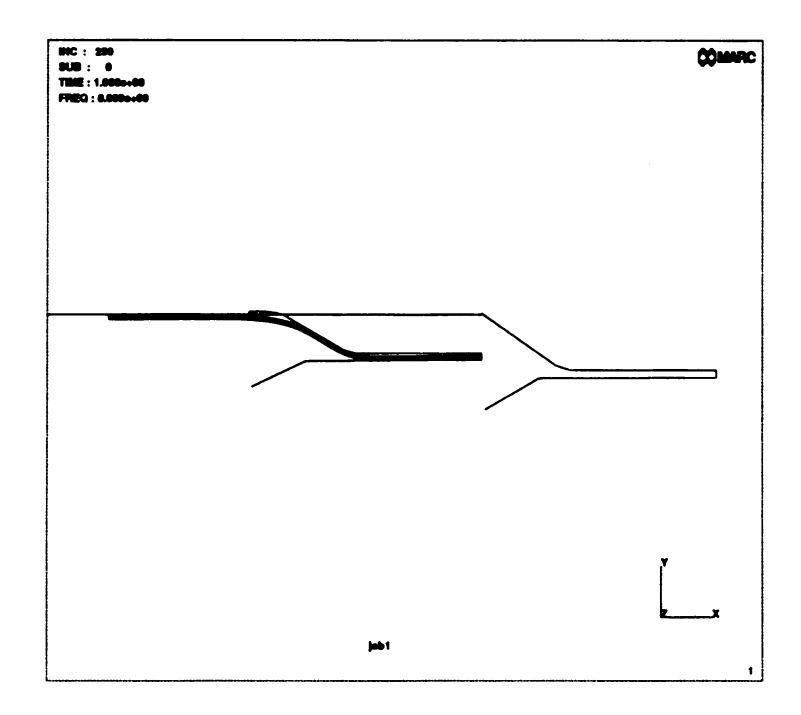


Figure 3.1(d) First Stage of Swaging at the 250th Increment.

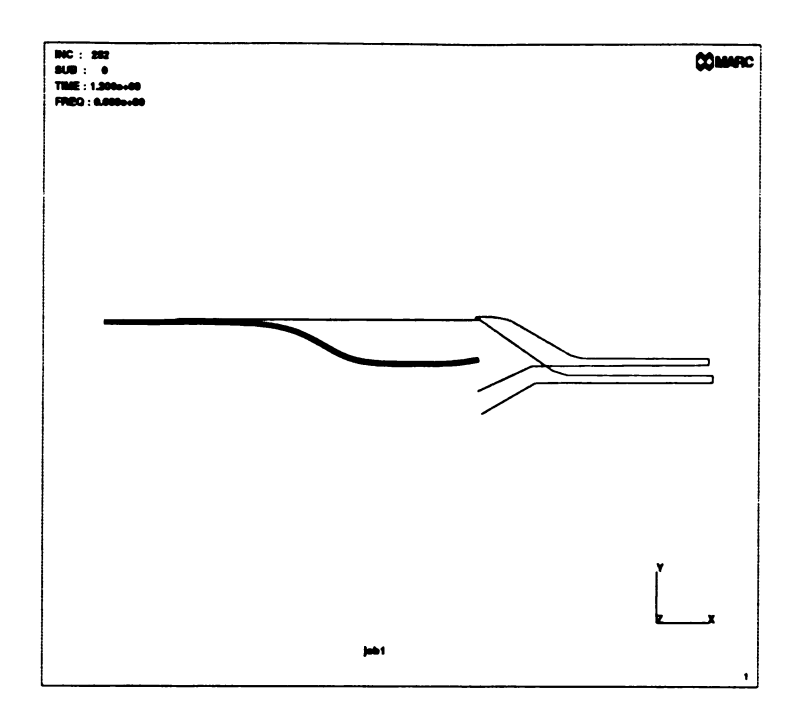


Figure 3.1(e) Release of the First Stage Tool.

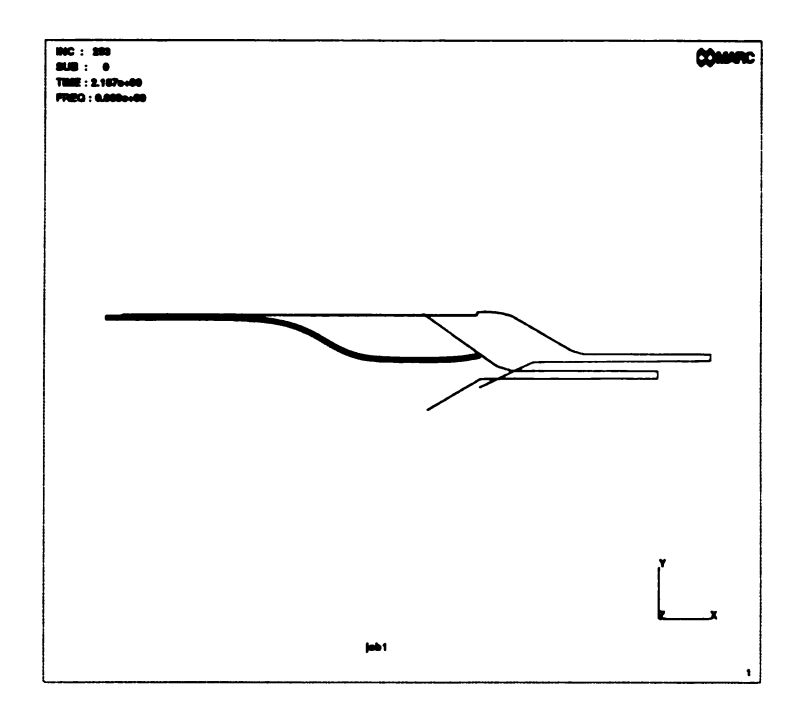


Figure 3.1(f) Tool Moved into Position in First Increment of Second Stage.

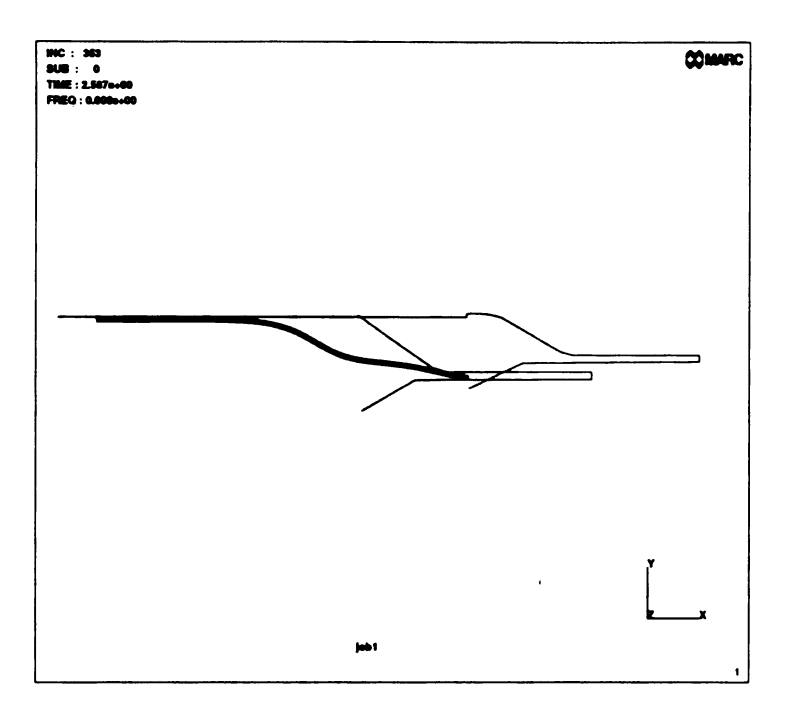


Figure 3.1(g) Second Stage of Swaging at the 352nd Increment.

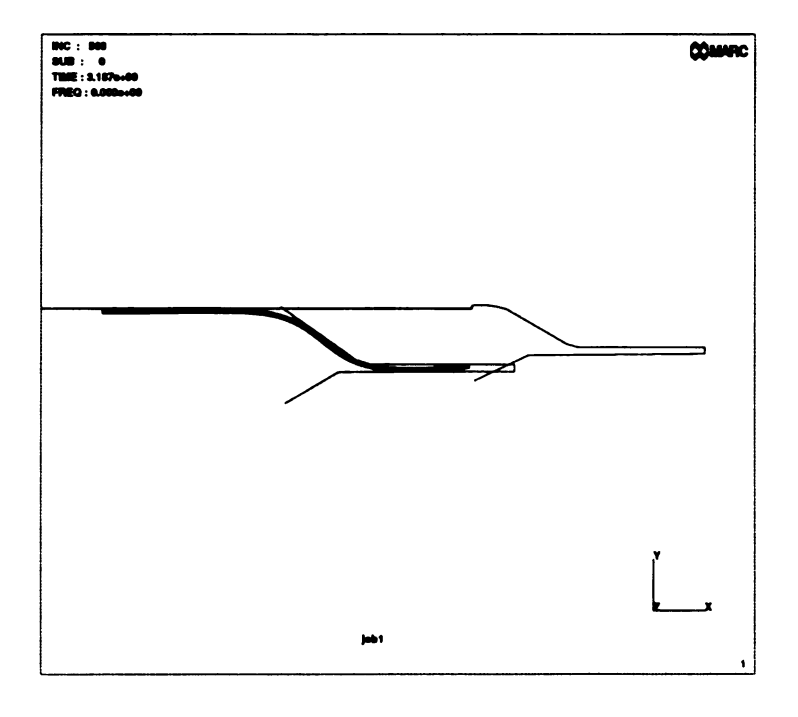


Figure 3.1(h) Final Increment of the Second Stage.

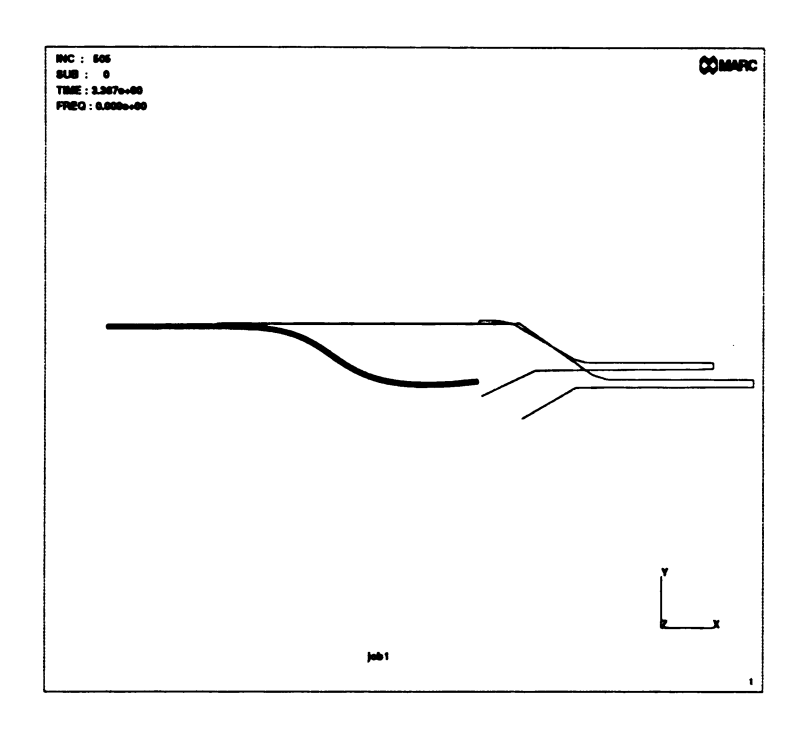


Figure 3.1(i) Release of Second Stage Tool.

which occurred at the 503rd increment and is shown in Figure 3.1(h). The forming process was completed in the 505th increment when the second stage tool was removed from the cylinder, as illustrated in Figure 3.1(i).

3.2 Final Element Selection

Three elements were still available for use in the modelling of the swaging process, elements 10,116, and 1. Each of these was used the model previously discussed. The results from each of these analyses were then evaluated to determine which provided the most accurate solution at the best computational cost.

3.2.1 Forming Analysis Results Using Element 1

After establishing the baseline with element 10, element 1 was used in the simulation of the forming process to determine if the efficiency which was exhibited in the test cases still held true. In review, Table 2.1 indicates that element 1 is a two-noded, isoparametric, and axisymmetric element which employs Simpson's rule integration through the thickness. As such, when substituting element 1 into the model, the number of layers within the element needed to be defined. For the metal forming analysis to be conducted 11 layers were specified. This was equivalent to using 11 Gauss points through the thickness which was attractive in that an accurate representation of the material effects should be the result. However, when the analysis was run, the model consistently failed to provide a solution. Either the solution failed to converge or the stiffness matrix of the model became singular (or nearly singular). Several attempts were made to overcome these difficulties, but no resolution was found. Therefore the decision was made to abandon further use of element 1.

3.2.2 Forming Analysis Results Using Element 116

The second element that was used in the model was element 116. Recalling Table 2.1, element 116 is a four-noded, isoparametric, and axisymmetric element employing reduced integration and hourglass control. In the previous studies of Section 2.1.1, this element also provided good convergence characteristics within a reasonable amount of computational time, and the same was hoped of the swaging simulation. Once again, however, the analysis deteriorated in all cases with element 116 providing the kinematical model for the cylinder. Inspection of Figure 3.2 reveals the presence of hourglass modes

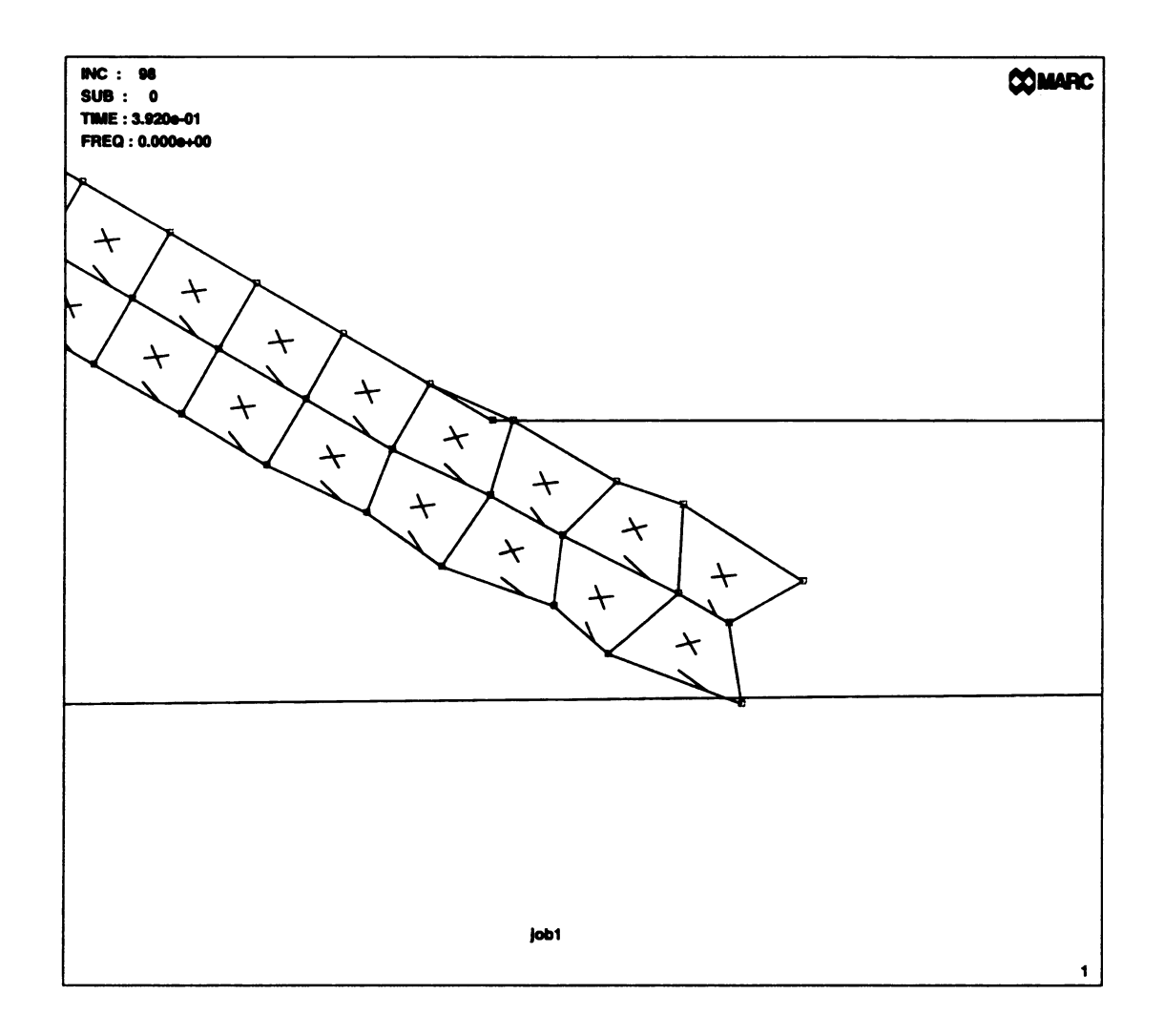


Figure 3.2 Swaging Analysis Using Element 116 with a 150x2 Mesh.

within the model at the 96th increment of the analysis. Thus it may be concluded that the stiffness that was added to the element in order to prevent zero-energy modes from occurring was not sufficient for this particular model. Thus, alternative approaches of prevention were tested. The first run using element 116 only had two elements through the thickness. It was believed that this may not provide enough stiffness in the presence of the plasticity model, nonetheless, increasing the number of through the thickness elements did not eliminate the hour glass modes. Therefore, a second attempt was made using a mixed model with two elements of type 10 at the leading edge of the cylinder and the remaining elements being type 116. This again proved to be a fruitless effort. As a result, element 116 was also no longer considered a viable element for the analysis at hand.

3.3 Convergence of Forming Problem

Element 10 was left as the only available element to discretize the model of the cylinder. With an element now selected, the mesh size needed to be finalized by conducting another convergence study similar to that of Section 2.1.1. Again, for the case of the forming process no tractable analytical solution is available, and experimental studies of the problem do not provide an adequate description of the internal stress state of the cylinder. Therefore, to gain confidence in the finite element solution, the model must be evaluated until a converged solution is found. For the swaging simulation, convergence must be achieved in two manners.

The mesh used to model the geometry should be refined in both the axial and radial directions to gain monotonically convergent results. Several reasons exist for the need to smooth the model in both coordinates. The cylinder initially has regions of plastic stress

due to the rolling of the flat sheet into a cylinder at the inner and outer surfaces as discussed in section 2.2.1. These plastic regions will grow radially inward as the cylinder is subjected to the forces of the forming dies. In order to capture the material effects of the growing plastic region, the model should have a large number of Guass points through the thickness of the cylinder cross section. The convergence of the calculated values in the radial coordinate would indicate the accuracy of the material model. In addition, the number of elements in the axial direction were increased to capture the path dependency involved. This was done in conjunction with a study on the number of load steps that were necessary for reliable results.

The number of load used to model the forming process will also contribute to the path dependency of the results obtained from the model. This is because the physical process of swaging the cylinder is carried out in two smooth, continuous motions. However, in the finite element model of the process, the tools were given a velocity which was divided into a number of equal load steps. By this method, the displacement of the rigid dies is not a continuous function of time, but rather a piecewise linear approximation. Of course a greater number of time steps taken will increase the smoothness of the tool displacement which affects the path dependency of the cylinder. Larger time steps will move the tool a greater distance along the axis of the cylinder and will result in greater incremental displacements. Therefore it is recommended that a convergence study on the number of load steps also be conducted.

3.3.1 Mesh Refinement Study

A study of the elemental convergence of the first stage was conducted to determine which mesh would provide for the most accurate results. For this convergence study, the baseline mesh remained 150 x 2. The elements were then increased through the thickness of the cylinder up to eight. The number of axial elements were then expanded to 300 and finally to 400. In the case of 300 elements the through the thickness elements were the same as for the 150 meshes. For the meshes containing 400 elements, analyses with 2 and 3 elements through thickness were not run because it was already determined that more elements through the thickness were needed to account for the material variations in that direction. Upon completion of each analysis, the values of axial and circumferential strain and stress were collected on the outer surface, mid-plane, and inner surface of the cylinder at two points within the mesh. The first of these points, labeled 'Point A' in Figure 3.3, was within the first bending region and the second was in the critical region, 'Point B' in Figure 3.3. Also it should be noted that the data was gathered at the 240th increment of the analysis and not the final 250th increment as specified in the model. The reason for this was that some of the models exhibited slight penetration through the end of the tool, which resulted in extraneous axial stresses in the cylinder. Therefore, to make a fair comparison between the models, the 240th increment was used to avoid the penetration problem. The strain and stress data resulting from the convergence study can be found in the Appendix Tables A.1 through A.24. For compactness, the discussion that follows will refer to that data, but specific data values are not mentioned.

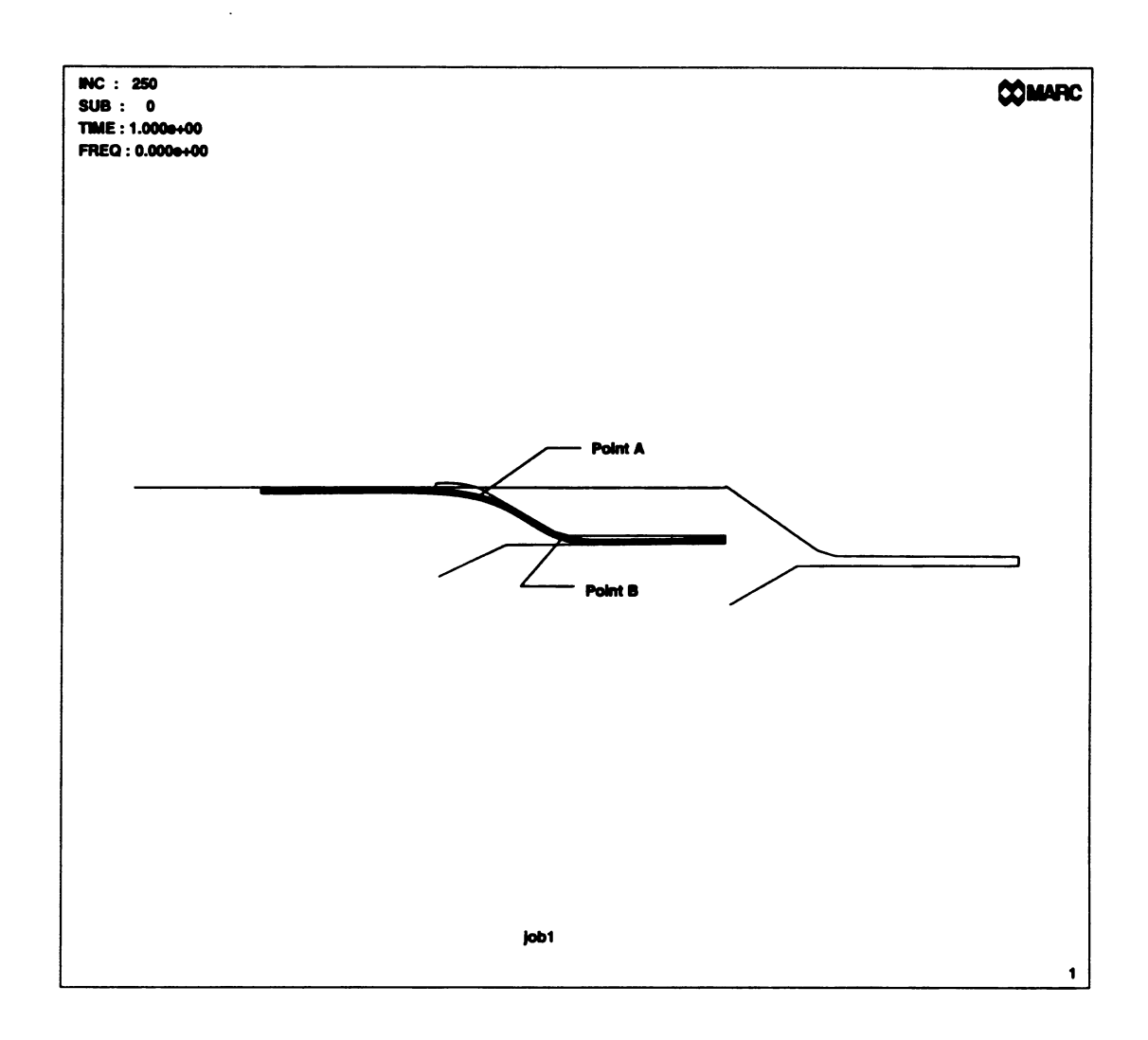


Figure 3.3 Sampling Locations for Convergence Study of Forming Analysis.

3.3.2 Discussion of Mesh Convergence Study Data

The analysis of the gathered data began with an evaluation of the strain values, where very little variation resulted from increasing the number of through-the-thickness elements. In Figures 3.4 through 3.7, the strain values versus mesh size were plotted for the critical region and appear to contradict this assessment. While the data for those meshes with 150 elements and 400 elements along the length were in good agreement with one another, meshes with 300 elements along the length exhibited large variations in the strain values with increasing mesh refinement through-the-thickness. This is, however, misleading due to the scaling used for the generation of these plots. In fact, an examination of the percentage change in the strain resulting from refining the mesh size would be more revealing as has been done in Tables 3.1 and 3.2. The observation could then be made that the changes in strain magnitude were actually less than four percent for each component on both of the cylinder surfaces. The exception was the axial strain on the outer surface of the cylinder. Here the values varied by up to 350 percent, however, the magnitude of strain in this region was an order of magnitude smaller than the other strain measures. Thus, this strain component was not dominant in the swaging simulation and therefore did not alter the earlier conclusion. Similar conclusions may be drawn for the strains in the first bending region. In any case, these small changes in strain were not surprising because the displacements in the first stage of the forming process were controlled by the geometry of the tool. The route followed by the cylinder would not be significantly altered by an increase in the number of elements through the thickness.

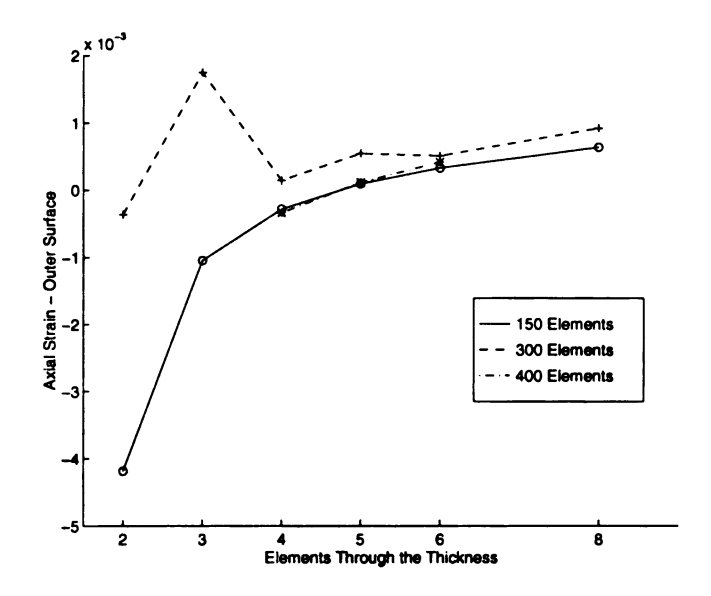


Figure 3.4 Axial Strain on the Outer Surface in the Critical Region vs. Mesh Size.

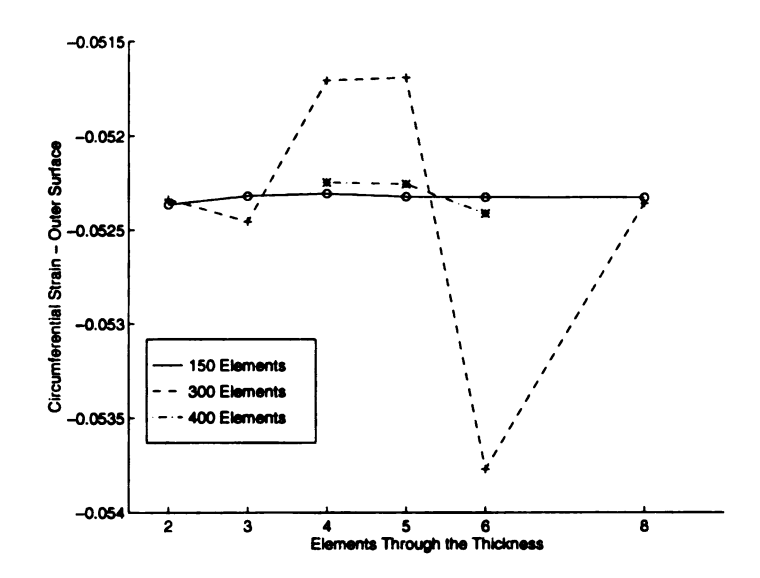


Figure 3.5 Circumferential Stress on the Outer Surface in the Critical Region vs. Mesh Size.

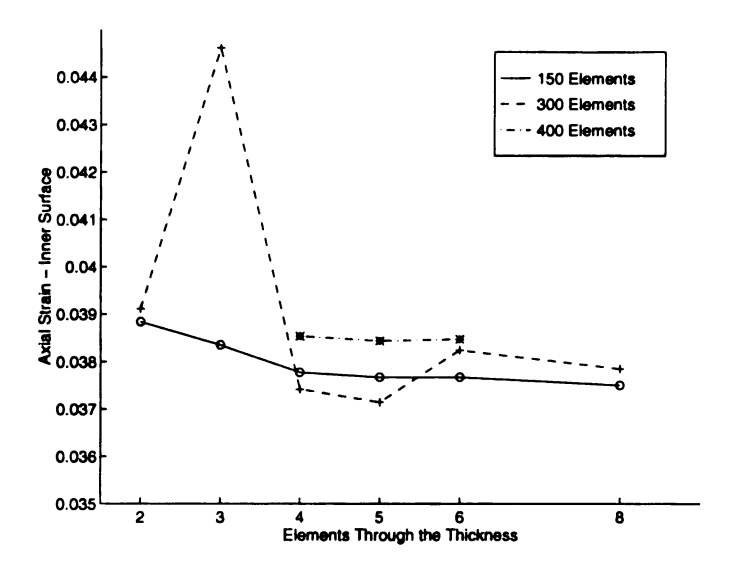


Figure 3.6 Axial Strain on the Inner Surface in the Critical Region vs. Mesh Size.

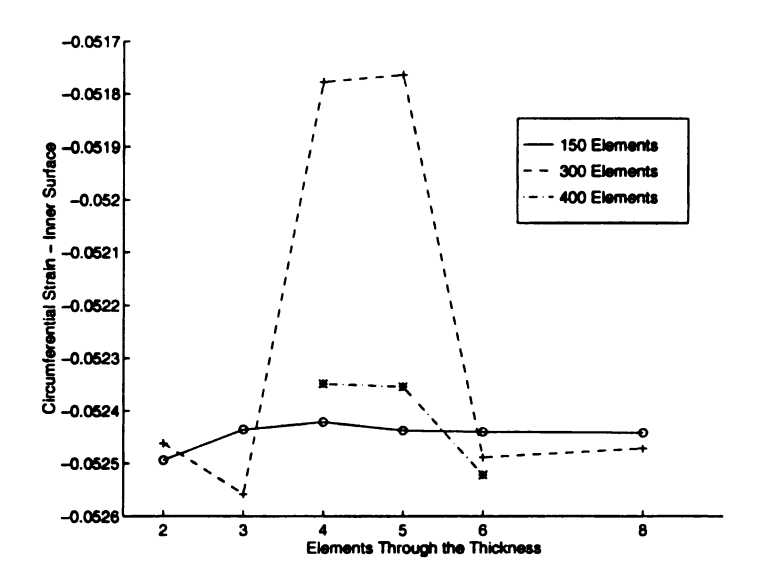


Figure 3.7 Circumferential Strain on the Inner Surface in the Critical Region vs. Mesh Size.

Table 3.1 Percentage Change in Axial Strain Values in the Critical Region. (%)

		Elements Through the Thickness					
Cylinder Surface	Axial Increase	2	3	4	5	6	8
Outer	150 to 300	91.46	267.71	286.70	81.60	34.98	30.70
	300 to 400			-144.70	-348.90	-21.83	
Inner	150 to 300	0.70	14.05	-0.95	-1.40	1.53	0.92
	300 to 400			2.90	3.34	0.60	

Table 3.2 Percentage Change in Circumferential Strain Values in the Critical Region. (%)

		Elements Through the Thickness					
Cylinder Surface	Axial Increase	2	3	4	5	6	8
Outer	150 to 300	0.06	-0.26	1.16	1.22	-2.69	-0.06
	300 to 400			-1.03	-1.07	2.59	
Inner	150 to 300	0.06	-0.23	1.24	1.30	-0.09	-0.06
	300 to 400			-1.09	-1.13	-0.06	

The formation of wrinkles in the cylinder is directly attributable to the build up of stresses and strains in the critical region. Therefore attention was also focused on the calculated stress values obtained from the convergence study where it was found that the trends contrasted those of strains. The change in stress states due to an increase in elements along the length was found to be minimal, but a change in the number of elements in the radial coordinate had a distinct impact on the stress values as shown in Figure 3.8 through 3.11. For the cases of 150 and 300 elements along the length, these plots show the stresses found on the outer and inner surfaces in the critical region versus the number of elements through the thickness. The effect of increasing the axial elements had very little consequence on the stress values obtained from the model as evidenced by the close agreement between the two curves in each of the plots. In contrast the multiplication of the number of elements through the thickness seemed to have a dramatic effect. As discussed in Section 2.2.1, the cylinder enters the forming process with initial stresses which induce zones of plasticity near the outer and inner surfaces of the crosssection. During the forming of the cylinder these plastic regions grow radially inward and the resulting stress gradients were adequately captured only by increasing the number of elements (thereby increasing the Gauss points) through the thickness. Accordingly, as the mesh was refined through the thickness, the values of stress began to converge. However, as can been seen in Figures 3.8 through 3.11, a converged solution was not attained with the meshes used.

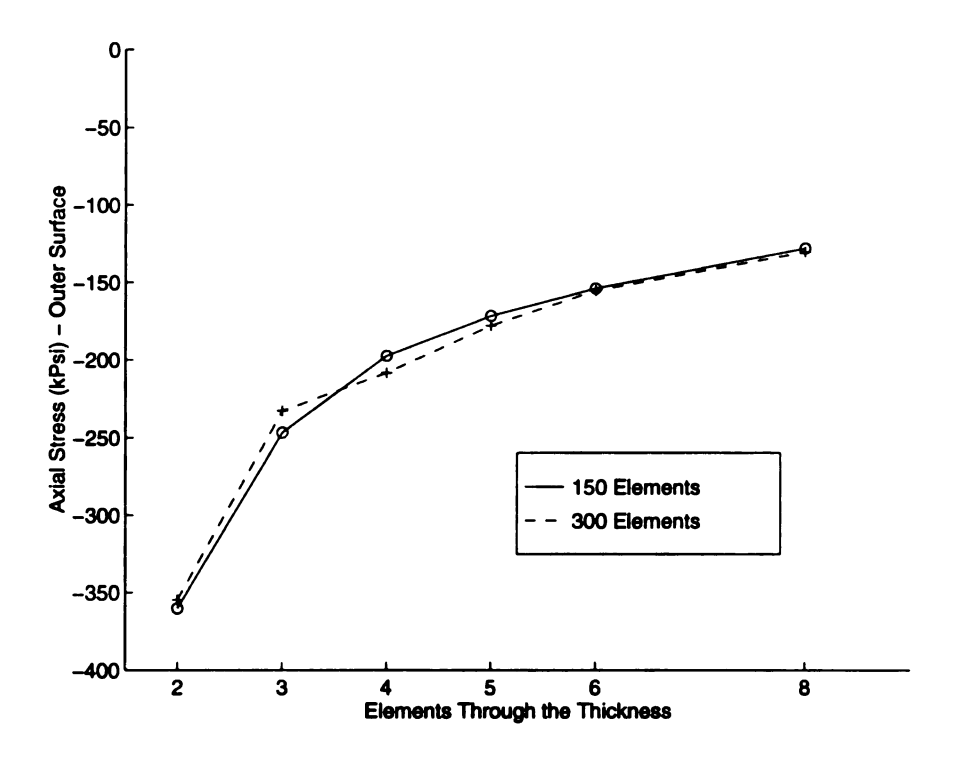


Figure 3.8 Axial Stress on the Outer Surface in the Critical Region vs. Mesh Size.

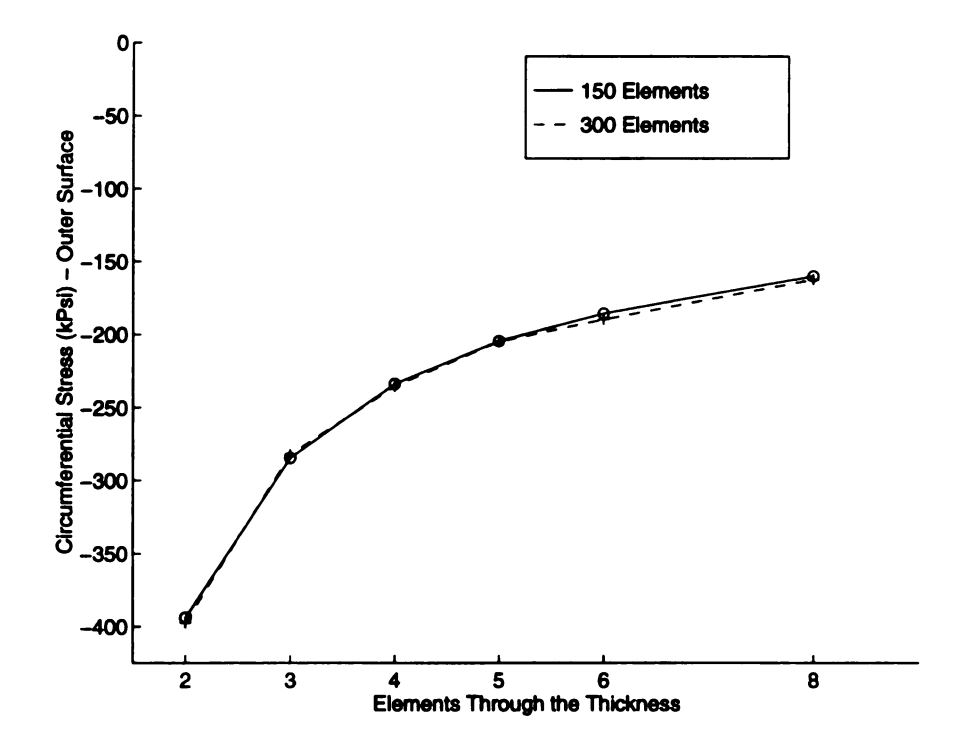


Figure 3.9 Circumferential Stress on the Outer Surface in the Critical Region vs. Mesh Size.

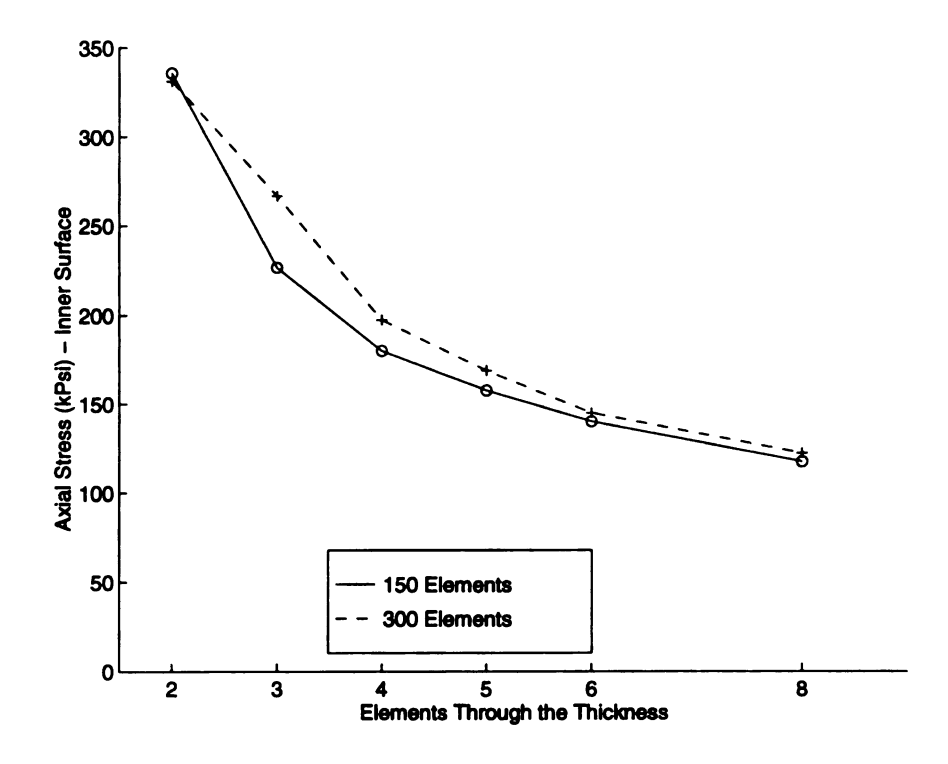


Figure 3.10 Axial Stress on the Inner Surface in the Critical Region vs. Mesh Size.

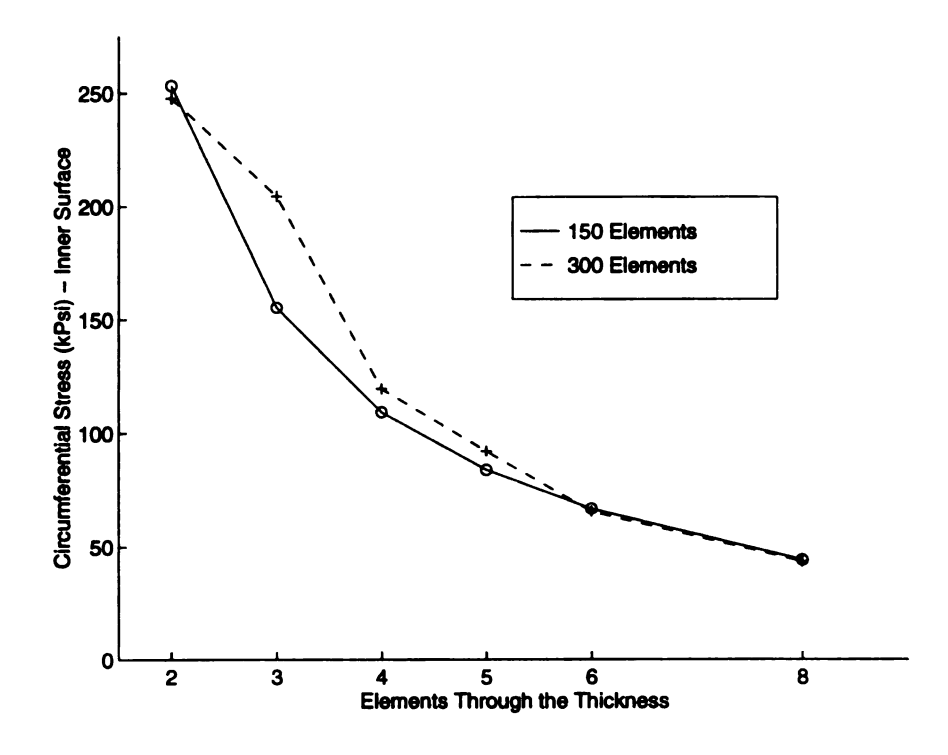


Figure 3.11 Circumferential Stress on Inner Surface in the Critical Region vs. Mesh Size.

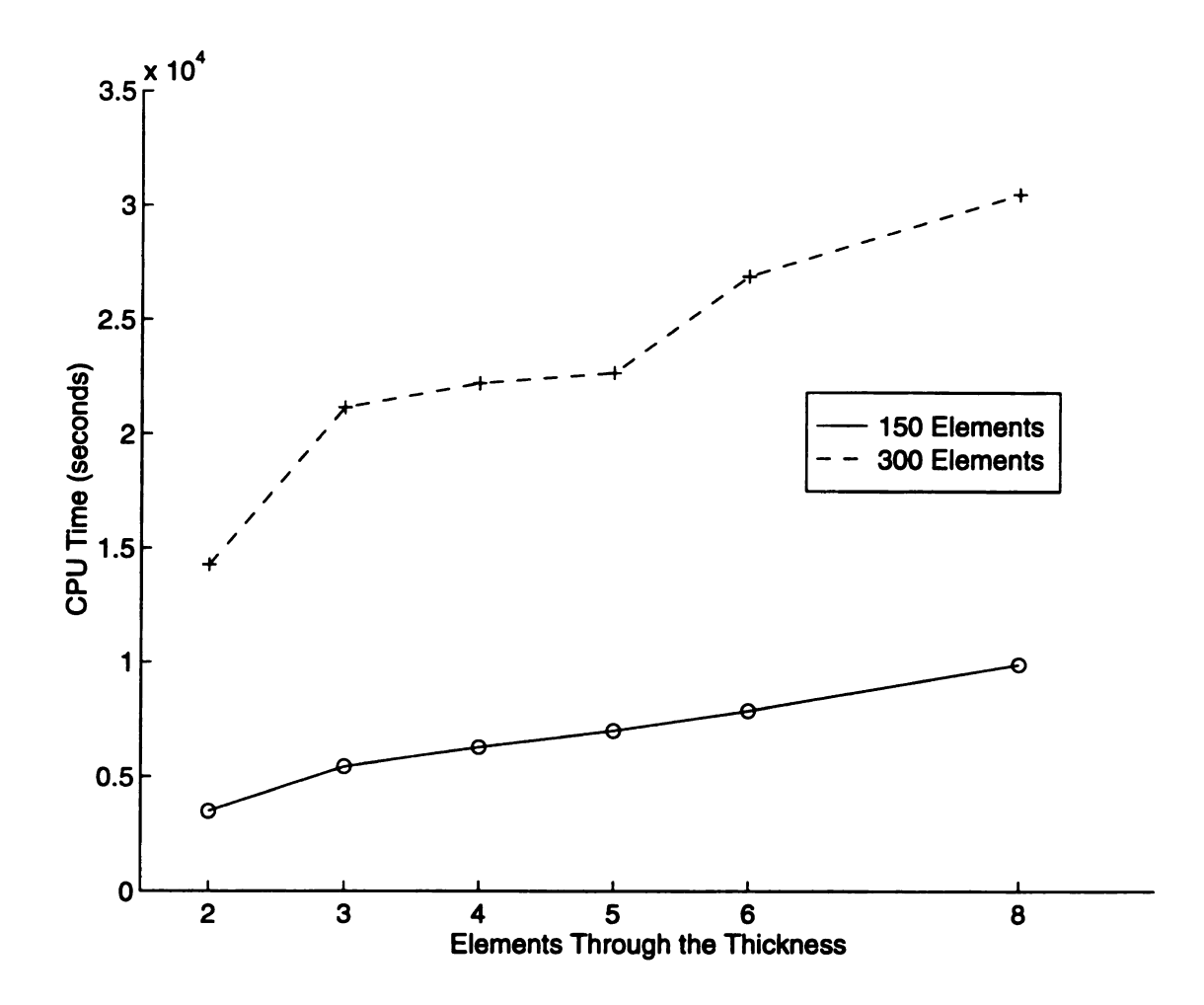


Figure 3.12 Computational Time vs. Mesh Size.

The question still remains as to which mesh should be used in the simulation of the forming simulation. Two final analyses of the convergence data provided the answer. First of all, was the rather minimal increase in strain and stress values obtained from increasing the number of elements along the length computationally efficient? This query was answered by plotting the CPU time (the amount of time the computer took to solve the finite element equations) versus the mesh size, as was done in Figure 3.12. The CPU times were obtained by performing each analysis on a Hewlett-Packard Series 9000 model 715 Unix workstation running at 75 MHz with 32 megabytes of RAM and 1 Gigabyte of disk swap space. In Figure 3.12 the meshes containing 300 elements were observed to require an average of 1.57x104 CPU seconds (4.4 CPU hours) more CPU time to complete than those with 150 elements. Therefore, the 150 element meshes appeared to be more attractive, but final judgement was reserved until a comparison of the results was made.

3.3.3 Comparison of Stress Trends Resulting from Mesh Refinement

Finally, the axial and circumferential stresses in the critical region for three meshes; 150x8, 300x8, and 150x2, were plotted to see the variations present. By zooming in on the critical region, the stress gradients were magnified to produce Figures 3.13 through 3.18. In each of the figures, the color bar indicates that compressive stresses were present on the outer surface, while the inner surface was subjected to tensile stresses. Comparing the stresses for the 150x8 mesh in Figure 3.13 and 3.14 to those of the 300x8 mesh in Figure 3.15 and 3.16 the only evident improvement was in the lengthwise gradients, but the gains were minimal. This information coupled with the run time data lead to the conclusion that 150 element meshes should be used for any subsequent analysis

of the forming process. In looking at the results from the 150x2 mesh in Figure 3.17 and 3.18 the trends remained the same, but the contours were more banded than in the previous plots. This was a result of only two elements through the thickness being used. As such, the stresses can only be linearly interpolated between four points rather than sixteen, thus yielding poorer gradations of stress. But the trends still show compressive stresses on the outer surface and tensile stress on the inner. This appeared to indicate that the 150x2 mesh would be appropriate for the simulation, provided the conclusions are to be based on the stress trends and not the absolute values.

Earlier, concern was expressed about the presence of locking in meshes where the element aspect ratio was greater than 1.0. The 150 x 2 mesh has an aspect ratio of 1.33 and as a consequence locking should be a concern in the second stage of the forming. In order to judge the effects of locking an 800 x 2 mesh, aspect ratio = 0.25, was run. The displacements from that analysis were plotted in Figure 3.19 for increment 303 and in Figure 3.21 for increment 373. Analogous plots were constructed for the 150x2 mesh and are shown in Figures 3.20 and 3.22. The results were very nearly the same in both meshes, thereby indicating that the 150 x 2 mesh was not overly stiff. A possible explanation for the non-existence of locking could be the complicated state of plasticity in the model, but an in depth evaluation for this phenomenon was not performed. But, the absence of locking certainly solidified the argument to use the 150 x 2 mesh in the swaging simulation.

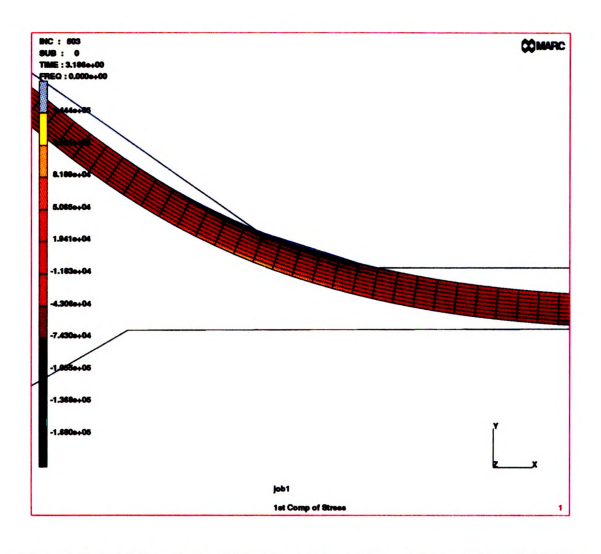


Figure 3.13 Axial Stress in the Critical Region for the Second Stage of the 150x8 Mesh.

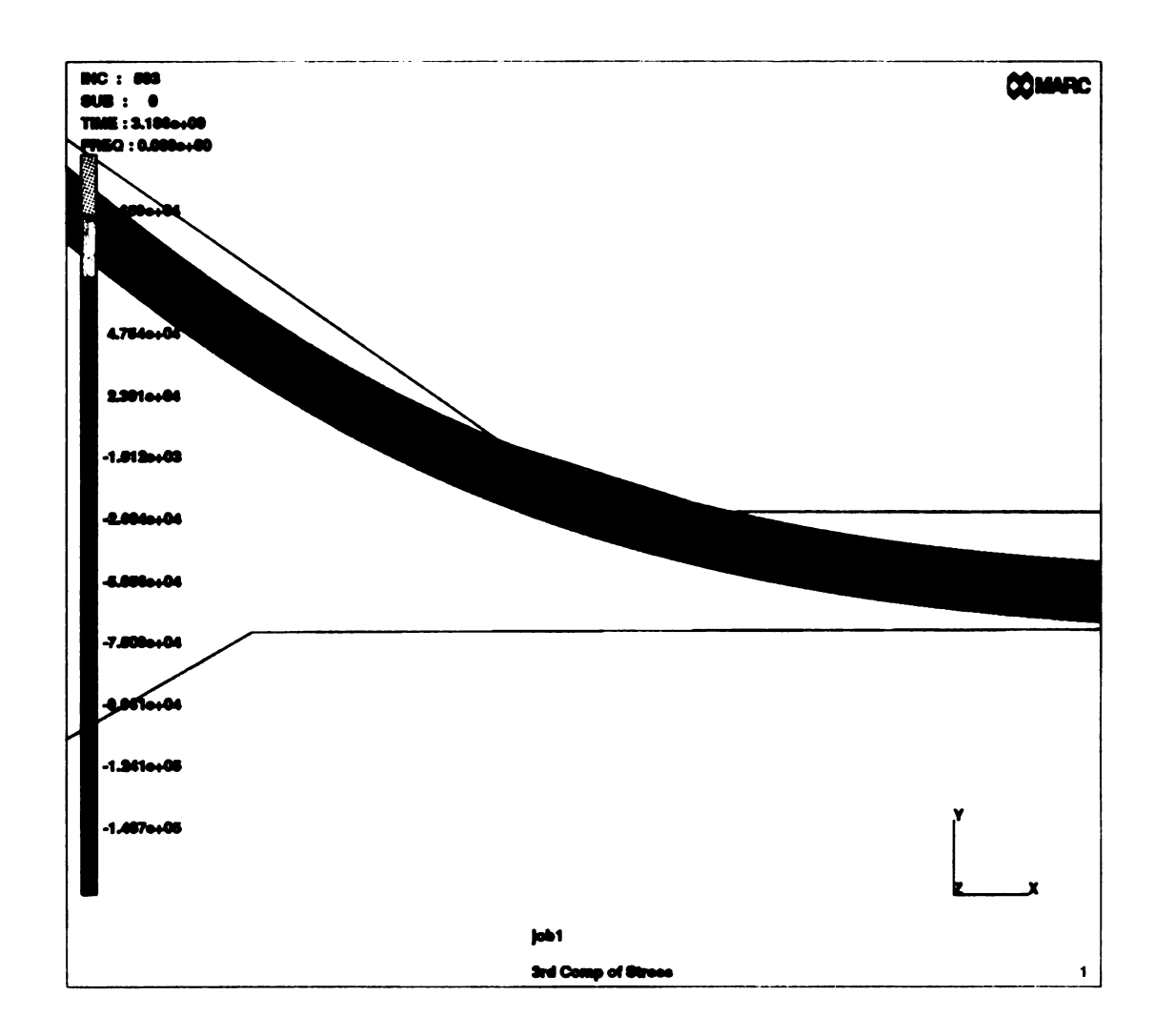


Figure 3.14 Circumferential Stress in the Critical Region for the Second Stage of the 150x8 Mesh.

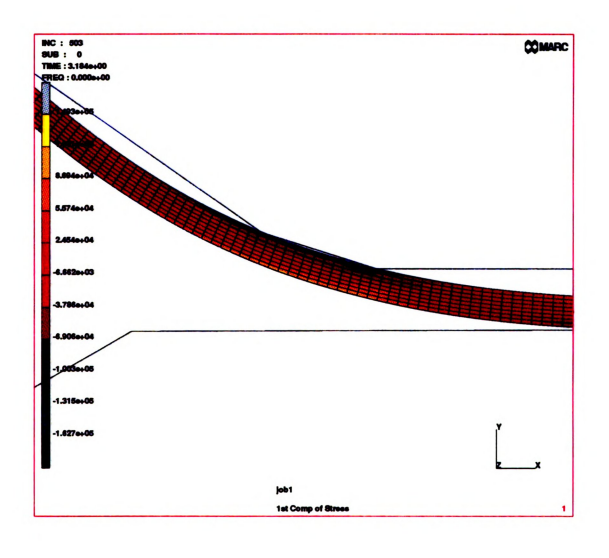


Figure 3.15 Axial Stress in the Critical Region for the Second Stage of the 300x8 Mesh.

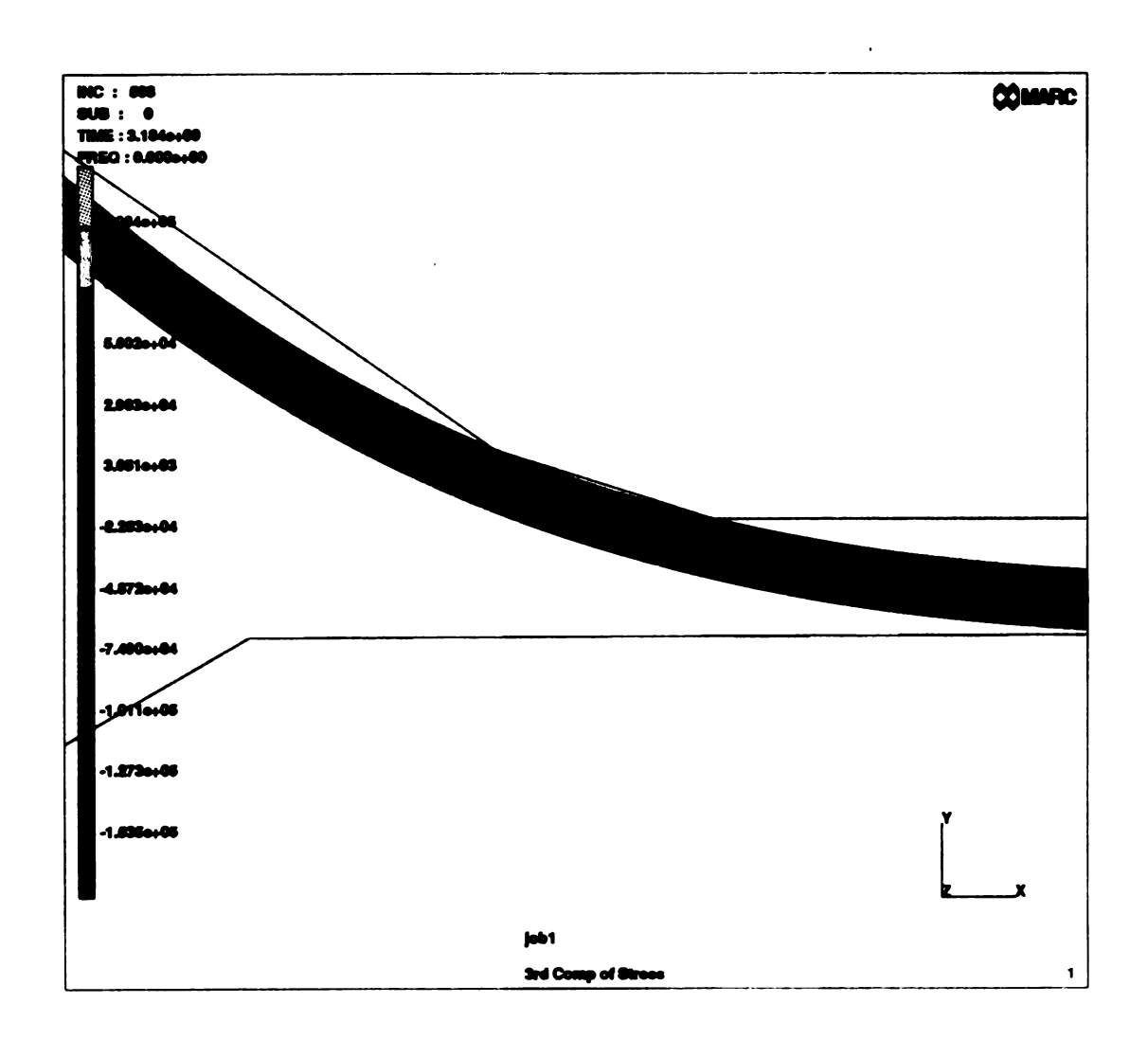


Figure 3.16 Circumferential Stress in the Critical Region for the Second Stage of the 300x8 Mesh.

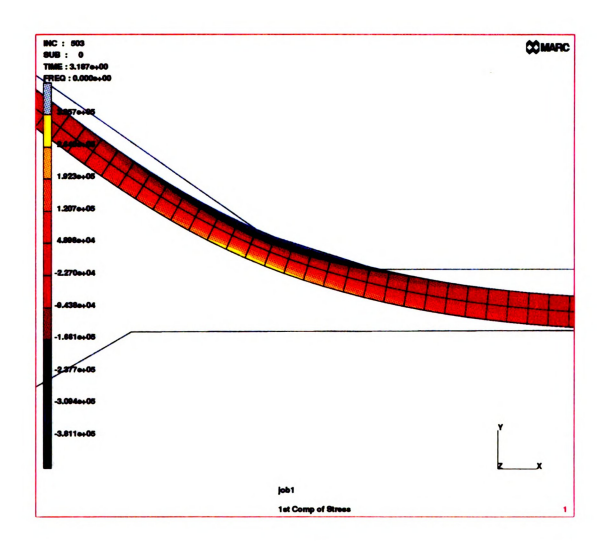


Figure 3.17 Axial Stress in the Critical Region for the Second Stage of the 150x2 Mesh.

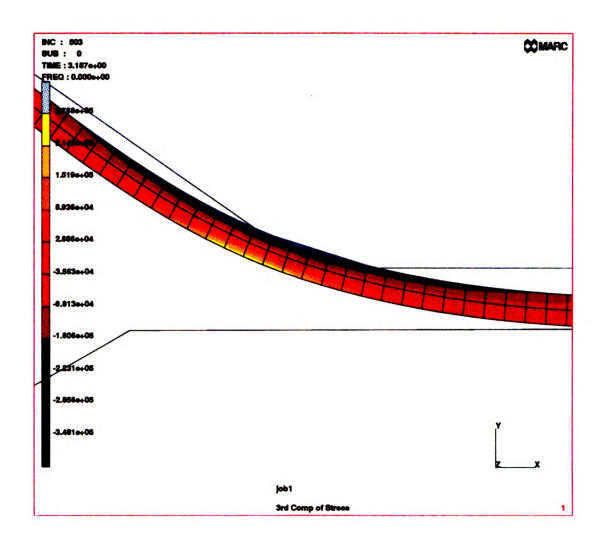


Figure 3.18 Circumferential Stress in the Critical Region for the Second Stage of the 150x2 Mesh.

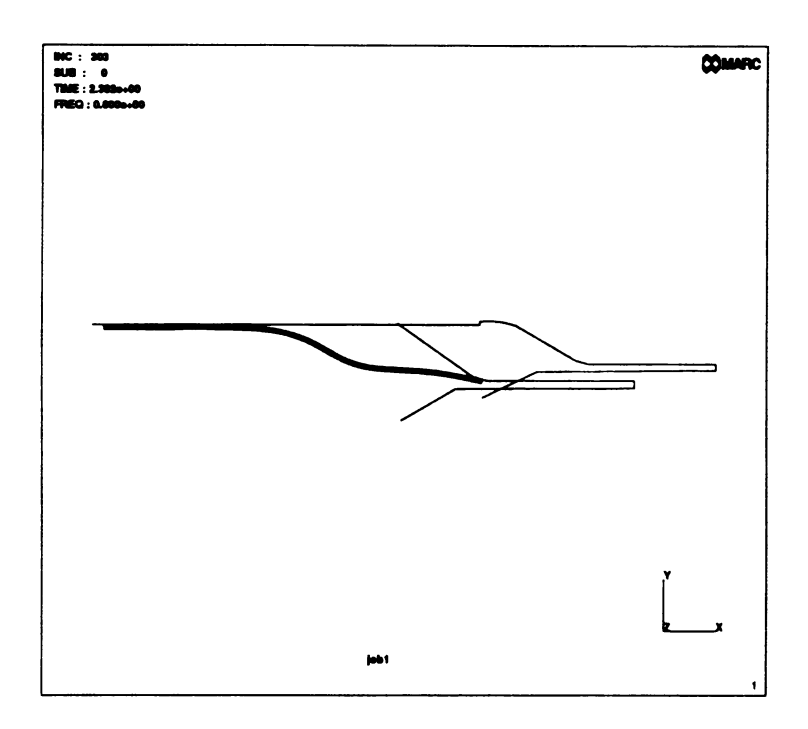


Figure 3.19 Deformations of the 800x2 Mesh at Increment 303.

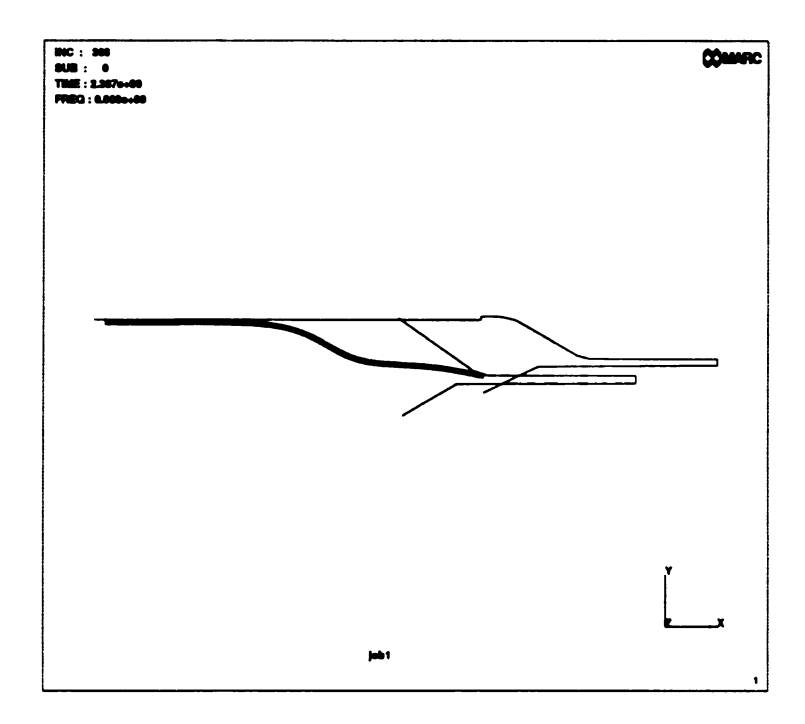


Figure 3.20 Deformations of the 150x2 Mesh at Increment 303.

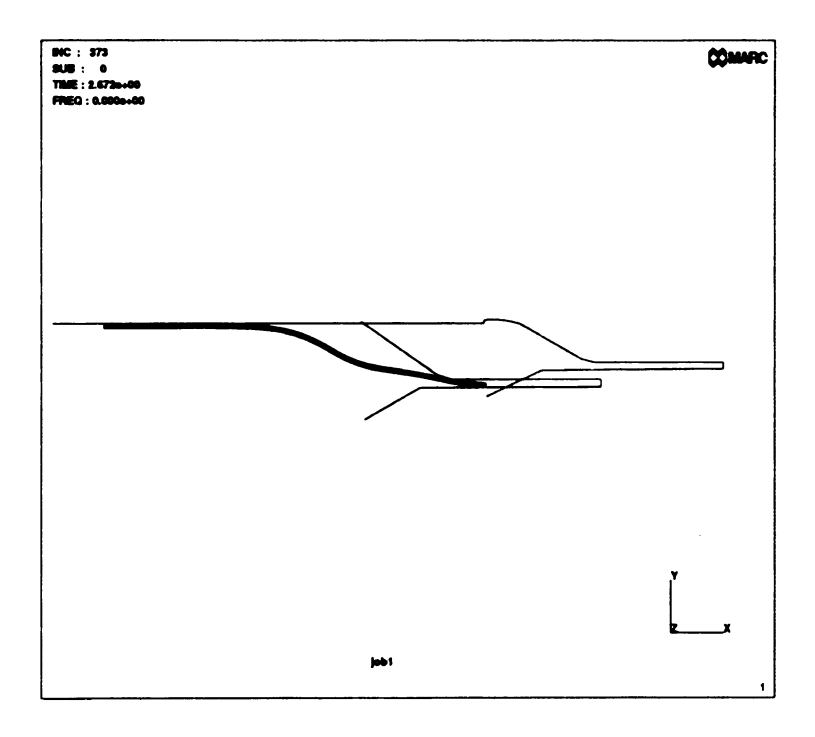


Figure 3.21 Deformations for the 800x2 Mesh at Increment 373.

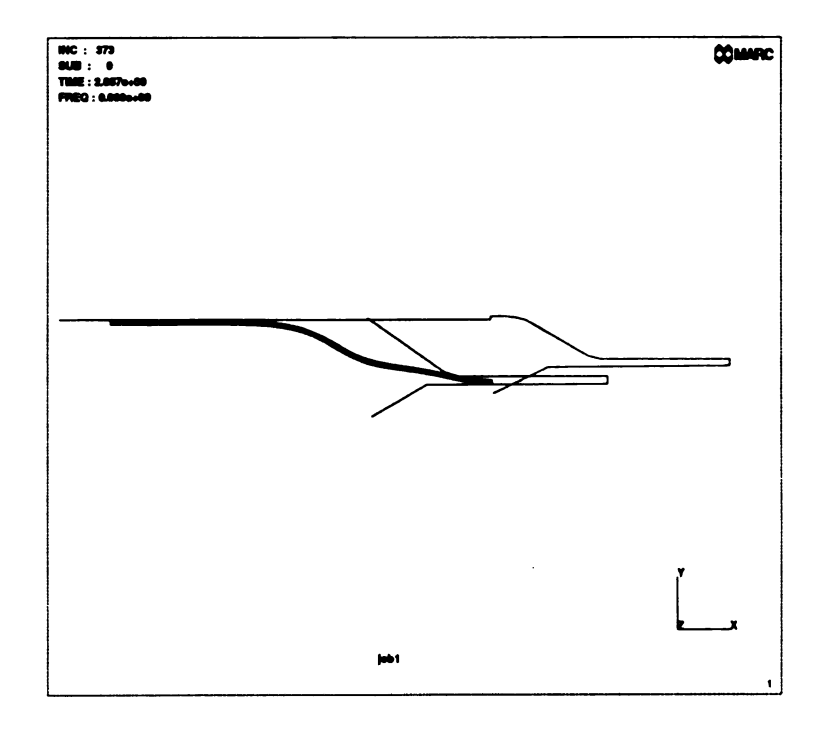


Figure 3.22 Deformations for the 150x2 Mesh at Increment 373.

3.3.4 Convergence Study on Number of Load Increments

The last component of the mesh that needed to be finalized was the number of increments required. Some indications of path independence were expressed above. To prove this was the case, both stages of the 150x2 mesh were used in an analysis with 500 load steps for each stage of forming instead of the usual 250. Once again, very little variation in the strains was evident. The stress data in the critical region for the first stage was collected in Table 3.3 and the second stage in Table 3.4. The data indicated that the largest change for any of the values was less than 3.0 percent, and therefore it could be said that the increase in the number of increments used to perform the analysis made no change in the results. As such, the simulation of the swaging process could confidently be carried out using the 150x2 mesh and 250 increments.

3.4 Results from Forming Simulation

3.4.1 Strain and Stress States in the Critical Region

Once a mesh was settled upon, results from the simulation were analyzed to determine possible mechanisms for wrinkling. The results from the final analysis are shown in Figures 3.23 through 3.26. In each of the plots the cylinder was in the final increment of the forming process (increment 503) and the data was collected in the critical region of the cylinder. The first contour plot, Figure 3.23, consists of the axial strains. As before, the color bar on the left hand side designates the dark red (almost a purple) region on the outer surface of the cylinder to be in a state of tension which increases in magnitude to the inner surface that is yellow. Intuitively, one would think the outer surface should be in compression as a thin-walled structure in bending would exhibit. However, the severe

Table 3.3 Stress Values for 250 vs. 500 incs for the First Stage in the Critical Region.

Number of Incs	σ _{xx} (outer)	σ _{xx} (mid)	σ _{xx} (inner)	σ _{θθ} (outer)	σ _{θθ} (mid)	σ _{θθ} (inner)
250	-288.52	8.38	272.58	-366.38	-64.87	208.42
500	-283.95	8.14	267.11	-361.82	-65.36	204.21
% change	1.58	-2.86	-2.01	1.24	-0.75	-2.02

Table 3.4 Stress Values for 250 vs. 500 incs for the Second Stage in the Critical Region.

Number of Incs	σ _{xx} (outer)	σ _{xx} (mid)	σ _{xx} (inner)	σ _{θθ} (outer)	σ _{θθ} (mid)	σ _{θθ} (inner)
250	-263.48	-4.12	240.95	-277.50	-63.17	175.29
500	-263.56	-4.23	240.22	-276.62	-63.04	174.92
% change	-0.03	-2.67	-0.30	0.32	0.21	0.21

state of bending to which the cylinder was being subjected has created membrane forces which overwhelm the bending forces resulting in tensile axial strains. Figure 3.24 shows the circumferential strains as increasing in magnitude moving left to right, corresponding to increased necking. Each value of strain was approximately constant through the thickness, analogous to a cylinder undergoing a uniform diameter reduction. The axial stress distribution displayed in Figure 3.25 indicates that the outer surface of the cylinder is in compression, as shown by the blue region, and the inner surface is in tension, as

shown by the red zone. In this case the membrane forces were as dominant as in the case of strains and so the bending forces were significant enough to create the compressive stresses on the outer surface. Finally, the stress gradients in the circumferential direction are given in Figure 3.26 and once again the outer surface was blue, or compressive, and the inner surface was red indicating tension. Recalling the circumferential strains were found to be uniformly compressive through the thickness, the presence of tensile circumferential stresses was initially surprising. These will be explained in the sequel

3.4.2 Assessment of Strain Hardening and Initial Stress Effects on Strain and Stress States

The effects of strain hardening and the initial stresses were examined by carrying out additional analyses, once without the work hardening table and the other without the initial stresses. In Table 2.5 the global maximum and minimum values of strain and stress are shown for the strain hardening models. From the data tabulated it can be seen that the hypothesis of Section 2.3.2 was indeed correct, the strain hardening had very little effect on the outcome of the analysis. Further comparison can be made by contrasting the contour plots of the model with strain hardening, Figures 3.23 - 3.26, to those without strain hardening which may be found in the Appendix, Figures A.1 through A.4.

The effects of the initial stresses were also evaluated. In Section 2.2.2 two methods of calculating the initial stresses were given. At that time it was stated that either method would not significantly affect the final results obtained from the model. Table 3.6 contains the global minimum and maximum strain and stress values from two models, the first being the model run with the initial stresses calculated by the first method (linear distribution through the thickness) and the second a model analyzed with no initial

stresses. From the data it may be concluded that the impact of initial stresses on the strain and stress values was minimal. More importantly the trends of stress distribution did not change, which can be seen by comparing the plots in Figures 3.25 and 3.26 to those of Figures 3.27 and 3.28. As previously stated, the model used does not yield a converged solution, and any explanations offered for the formation of wrinkles in the cylinder must be based on the trends of stress. Therefore, despite the fact that an alternate method of calculating initial stresses was available, the conclusions drawn from the results of the model are not dependent on either method.

Table 3.5 Effects of Strain Hardening on the Global Minimum and Maximum Strain and Stress Values

Model	ε _{xx} (max/ min)	ε _{θθ} (max/ min)	σ _{xx} (max/ min)	σ _{θθ} (max/ min)
With Strain Hardening	4.686x10 ⁻²	1.210x10 ⁻³	3.357x10 ⁵	2.768x10 ⁵
	-1.568x10 ⁻²	-8.707x10 ⁻²	-3.811x10 ⁵	-3.481x10 ⁵
Without Stain Hard- ening	4.685x10 ⁻²	1.207x10 ⁻³	3.392x10 ⁵	2.862x10 ⁵
	-1.574x10 ⁻²	-8.703x10 ⁻²	-3.863x10 ⁵	-3.508x10 ⁵
% Change	0.0	-0.2	1.0	3.3
	-0.4	0.5	-1.4	0.8

Table 3.6 Effects of Initial Stresses on the Global Minimum and Maximum Strain and Stress Values

Model	ε _{xx} (max/ min)	ε _{θθ} (max/ min)	σ _{xx} (max/ min)	σ _{θθ} (max/ min)
With Initial Stresses	4.686x10 ⁻²	1.210x10 ⁻³	3.357x10 ⁵	2.768x10 ⁵
	-1.568x10 ⁻²	-8.707x10 ⁻²	-3.811x10 ⁵	-3.481x10 ⁵
Without Initial Stresses	4.471x10 ⁻²	1.089x10 ⁻³	3.463x10 ⁵	2.867x10 ⁵
	-1.563x10 ⁻²	-8.705x10 ⁻²	-3.923x10 ⁵	-3.597x10 ⁵
% change	4.8	-11.1	3.1	3.5
	3.2	0.0	-2.9	-3.2

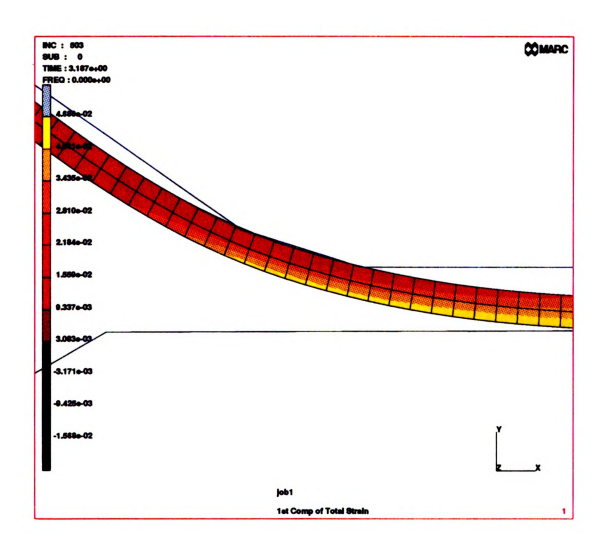


Figure 3.23 Axial Strains in the Critical Region at the 503rd Increment.

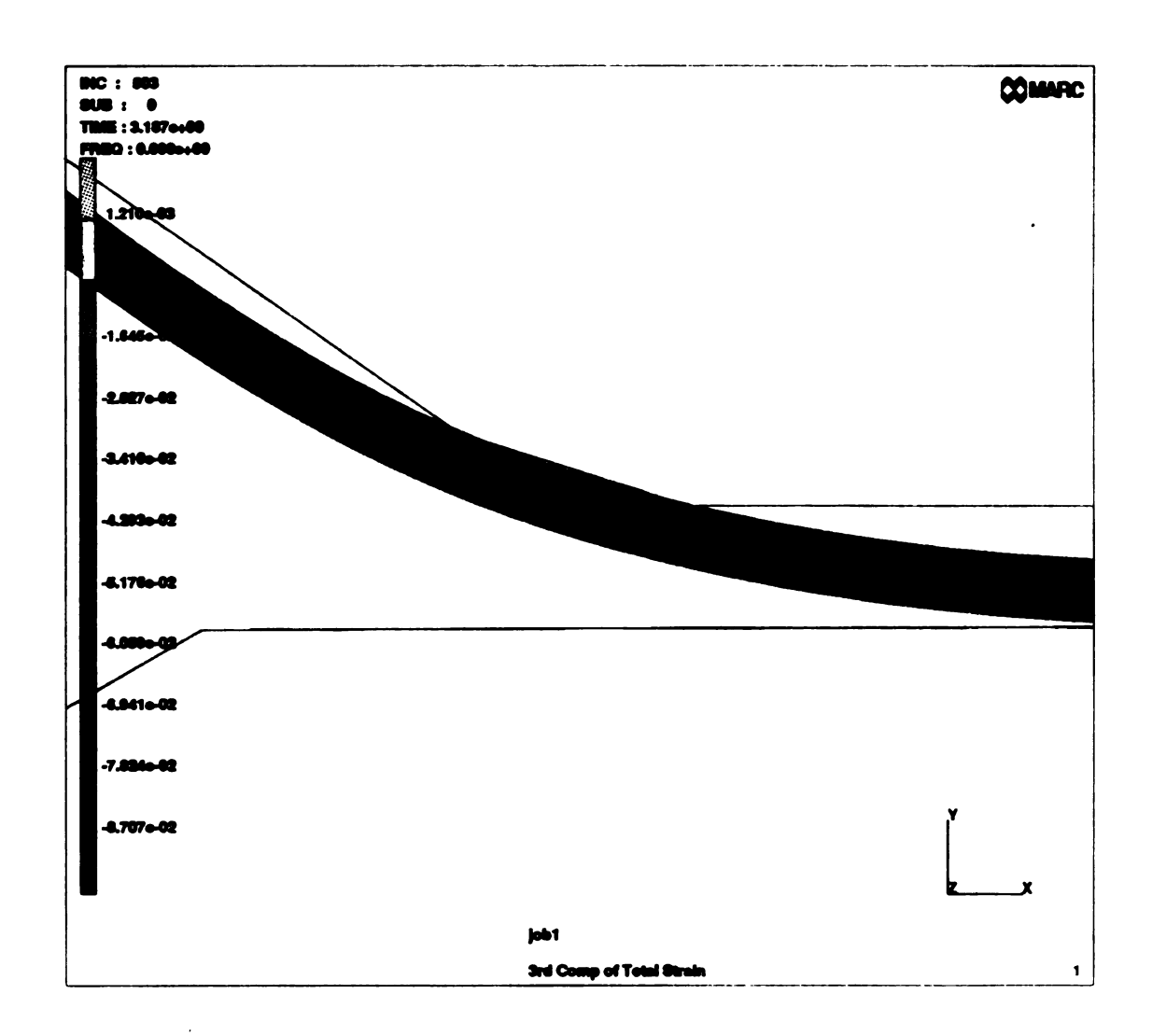


Figure 3.24 Circumferential Strains in the Critical Region at the 503rd Increment.

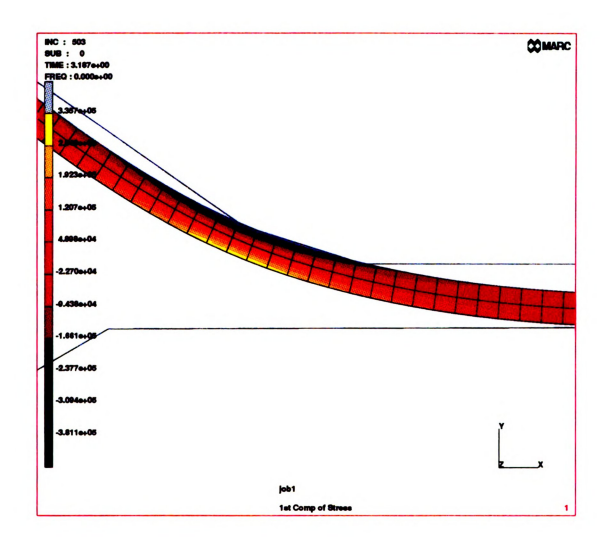


Figure 3.25 Axial Stresses in the Critical Region at the 503rd Increment.

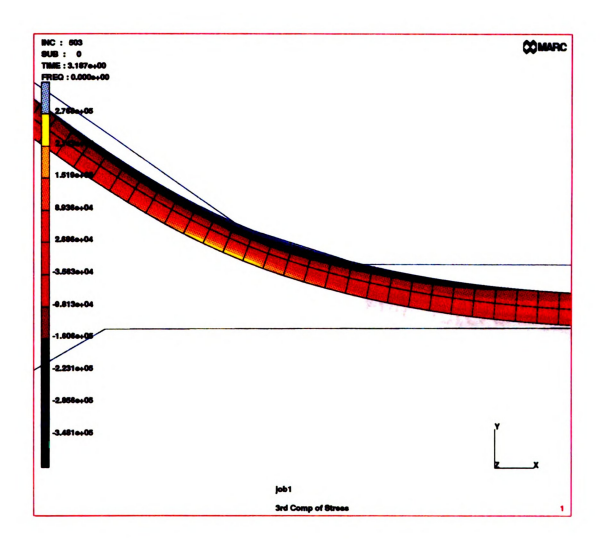


Figure 3.26 Circumferential Stresses in the Critical Region at the $503^{\rm rd}$ Increment.

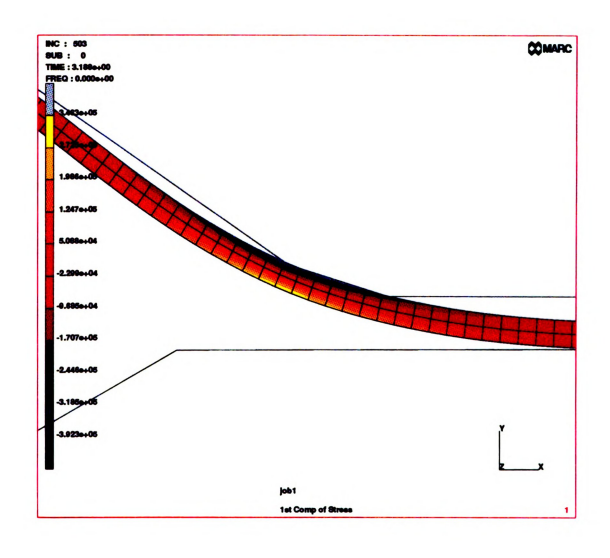


Figure 3.27 Axial Stresses in Critical Region at 503rd Increment, Calculated without Initial Stresses.

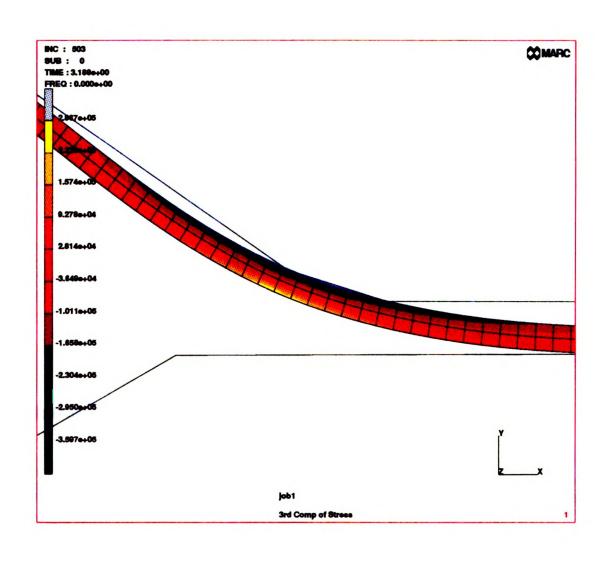


Figure 3.28 Circumferential Stresses in the Critical Region at the 503rd Increment, Calculated without Initial Stresses.

Chapter 4

Discussion of Wrinkling

4.0 Introduction

An assessment of the forming operation reveals that two basic modes of deformation are responsible for the diameter reduction of the cylinder. The first is a uniform diameter reduction and the second is the bending needed to get the leading edge of the cylinder into the "alley". While these two modes are, in fact, coupled due to the nonlinear nature of the problem, to understand their contribution to the formation of wrinkles, two arguments will be made. The first is based on the existence of some critical circumferential strain in the cylinder. The second will reveal the contribution of the bending energy to the formation of wrinkles.

4.1 Existence of Critical Strain

For illustration purposes, consider a straight column under an axial load, as shown in Figure 4.1. From strength of materials it is known that this column has a critical load, P_{CR} , which, when exceeded, will cause the column to snap into a new configuration upon the application of some small lateral load. This critical load may be found using Euler's equation,

$$P_{CR} = \frac{\pi^2 EI}{L^2},\tag{4.1}$$

where E is Young's modulus of the material, I is the moment of inertia of the column, and L is the length of the column. The moment of inertia for a rectangular column is given as,

$$I = \frac{1}{12}bh^3, (4.2)$$

where b is the width of the column and h is the thickness. Substituting Equation 4.2 into 4.1 and knowing that the area of the column is given as:

$$A = bh, (4.3)$$

Equation 4.1 may be written as:

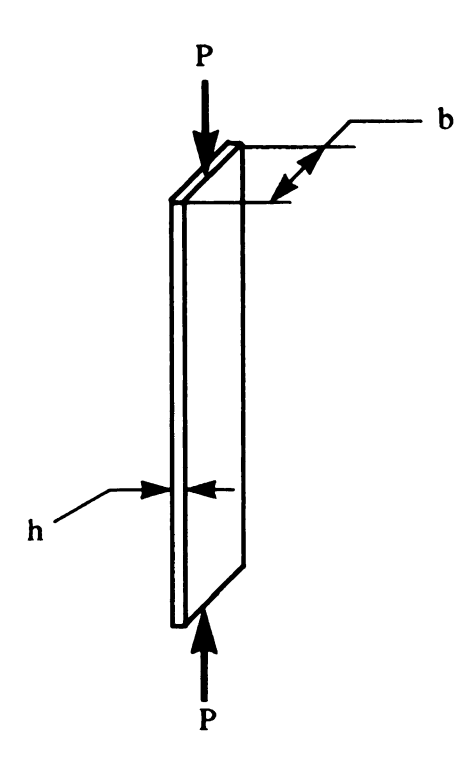


Figure 4.1 Euler Buckling Column.

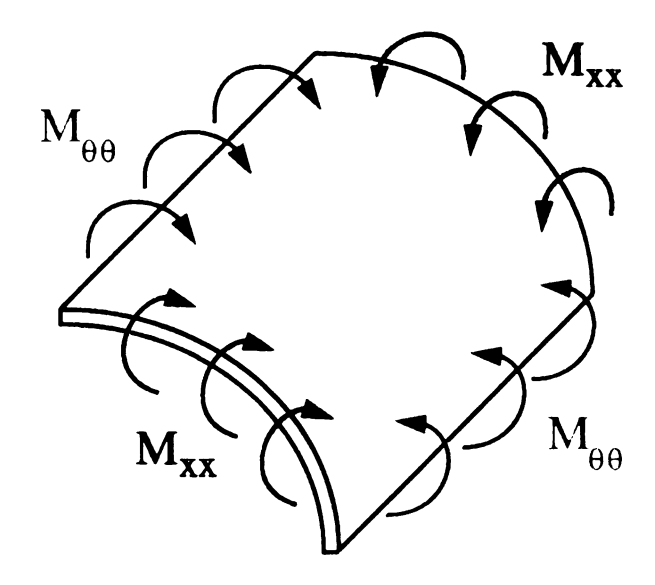


Figure 4.2 Shell Element Subject to Bending and Resultant Moments.

$$P_{CR} = \frac{\pi^2 h^2 A}{12L^2}. (4.4)$$

Finally the critical load may be written in terms of stress, which in turn may be related to a strain by the following equations,

$$P_{CR} = \sigma_{CR} A \qquad \sigma_{CR} = E \varepsilon_{CR}. \tag{4.5}$$

Thus, the critical strain relationship is found by,

$$\varepsilon_{CR} = \frac{\pi^2}{12} \left(\frac{h}{L}\right)^2. \tag{3.6}$$

From Equation 4.6 it may be seen that the critical strain of the column with a constant length, L, is a function of the thickness, h, squared. So as the thickness of the column is increased the critical load of the column grows in a quadratic manner.

The issue of wrinkling occurs in a cylinder under external pressure. For this geometry, the critical strain is proportional to the square of the thickness, h, over the radius, R, of the cylinder. Thus, if the induced strain is equivalent in the two cylinders, the thicker cylinder may not exceed its buckling strain, whereas the thin-walled cylinder under consideration could. From the viewpoint of a cylinder subject to a uniform diameter reduction the importance of the wall thickness is realized. However, the cylinder was also

loaded in bending, which gives rise to a more complicated state.

4.2 Bending Effects

Isolating the applied bending loads, a second approach is proposed to explain the results obtained for the variation of circumferential stresses as shown in Figure 3.26. The geometry to consider for this explanation is that of a cylindrical shell element depicted in Figure 4.2. Imagining that this shell was participating in the forming process, then as the leading edge of the shell was entering the "alley" it could be considered to be subjected to a bending moment $M_{xx} = \hat{M}$, shown in blue. The moment-curvature relations are given as,

$$M_{xx} = D(\kappa_{xx} + \nu \kappa_{\theta\theta}) M_{\theta\theta} = D(\kappa_{\theta\theta} + \nu \kappa_{xx})$$
(4.7)

where κ_{xx} and $\kappa_{\theta\theta}$ are the changes in curvature and D is the flexural rigidity given by

$$D = \frac{Eh^3}{12(1-v^2)}. (3.8)$$

The changes in the circumferential curvature were assumed to be neglible in comparison to κ_{xx} so let, $\kappa_{\theta\theta} = 0$. So $\kappa_{\theta\theta}$ was eliminated from both equations in Equation 4.8, yielding,

$$M_{xx} = D(\kappa_{xx} + 0)$$

$$M_{\theta\theta} = D(0 + \nu\kappa_{xx})$$
(4.9)

Examination of the second of Equations 4.9 reveals the existence of a significant resulting circumferential moment,

$$M_{\theta\theta} = D \nu \kappa_{xx}, \qquad (3.10)$$

shown in red in Figure 4.2.

 $M_{\theta\theta}$ is responsible for the regions of tensile circumferential stress in Figure 3.26, while in the presence of uniform compressive circumferential strains, Figure 3.24. As the cylinder was initially bent toward the "alley", corresponding to Point A in Figure 3.3, it was being loaded. Then, as it was bent back to go into the "alley", Point B in Figure 3.3, it was unloaded. The action of unloading the cylinder allows for the tensile stresses while at the same time producing compressive strains. This phenomena is demonstrated in Figure 4.3 which shows a history plot of the leading edge node on the inner surface as it travels through the second stage of the forming process. As can be seen at the zeroth increment the strains were zero and the stresses took on the value of the initial stresses. The first load step of the analysis takes both the strains and stresses into the compressive region and by the one hundredth load step the cylinder has reached the maximum values of strain and compressive stress. This corresponds to the point at which the leading edge was ready to enter the "alley". Subsequent load steps take the leading edge down the "alley", and the

stress strain curve enters the region of tensile stresses and compressive strains.

It has been shown that some critical strain exists within the cylinder. Upon exceeding that strain, any disturbance, whether due to the process or material imperfections, will cause the cylinder to buckle. However, the portion of the cylinder in the "alley" region of the tool does not exhibit the wrinkling phenomena. Thus, it is hypothesized that the wrinkling is due to the combined effects of diameter reduction and severe bending. Additionally, the resultant moment, $M_{\theta\theta}$, is responsible for the wrinkles protruding inward rather than outward. While the simple models used up to this point present possible explanations of the wrinkling problem, they do not, however, allow the prediction of the onset of wrinkling. They only provide a means to understand the phenomenon, and, at the same time, the suppositions made allow the possibility to present some recommendations.

4.4 Introduction of Stiffening Rib

Based on the level of understanding of the mechanics involved in the formation of wrinkles during the swaging process, a recommendation was proposed as a possible means of alleviating the wrinkling phenomenon. Because the stability of the cylinder was governed by a complex relationship between stress, material properties, and geometry, techniques for increasing the level of stability could be derived from one or more of these factors. After evaluation of several different solution methods, the addition of a circumfer

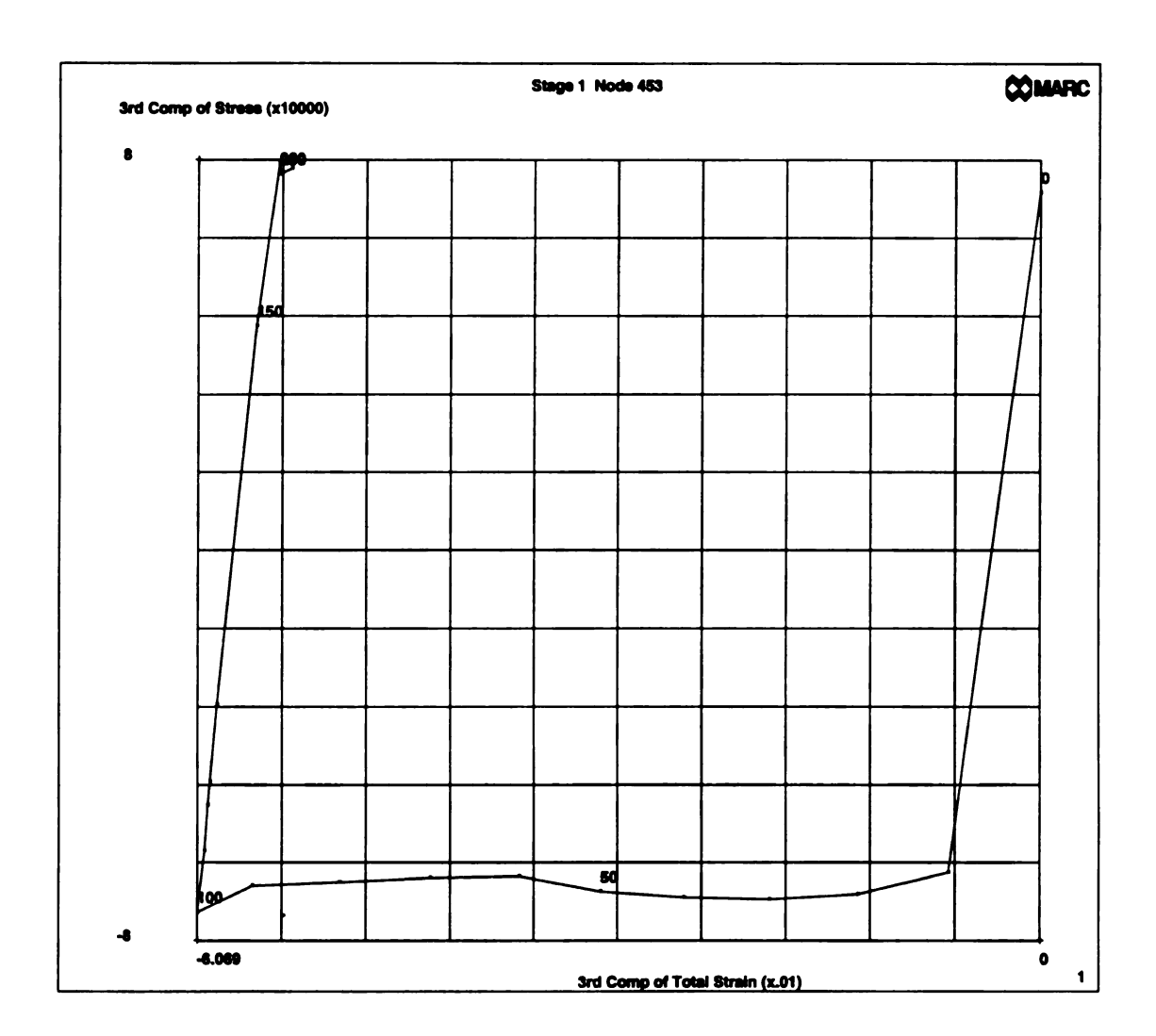


Figure 4.3 Circumferential Stress versus Strains for the First Stage of Forming.

ential stiffening rib presented itself as the most viable option.

In Section 4.2, the cylinder was shown to have a critical circumferential strain above which the cylinder could buckle. In addition the severe bending necessary to accomplish the diameter reduction also contributed to buckling. The combination of these two mechanisms is believed to give rise to wrinkling. The diameter to which the cylinder is reduced is an integral feature of the finished product and cannot be altered. Therefore, the options would be to reduce the compressive/tensile stress gradients or increase the cylinder's resistance to localized bending associated with the wrinkling mode. Stress reduction could be achieved by actually thinning the wall thickness of the cylinder in localized zones. But this would then weaken the resistance of the cylinder to axial loading, for example in the press fitting of a top, and as such this option did not seem to be acceptable. Also, a means of thinning the material in a high volume production setting could not be established. Thus, stress reduction did not appear to be practical. As a result attention was then focused on increasing the cylinder's resistance to bending.

Again, several methods were available to increase bending stiffness. An inspection of the equation which relates the changes in curvature to the bending moments shed light on these possibilities,

$$\kappa = \frac{M}{EI} \tag{4.11}$$

Equation 4.11 indicates that with a constant bending moment either the Young's modulus, E, or the moment of inertia, I, could be increased to result in smaller changes in curvature. Because the material used produced other desirable characteristics, the decision was to

attempt to increase the moment of inertia. This concept is reinforced by considering a beam in bending. In Figure 4.4(a) a bending moment is applied to the wide, flat face of the beam, whereas in Figure 4.4(b) the bending moment is applied to the thin edge of the beam. Intuitively, the beam of Figure 4.4(a) should bend more easily than the one in Figure 4.4(b) because of the increased vertical thickness of the beam in Figure 4.4(b). This is confirmed by Equation 4.12 which gives the moment of inertia for the beam,

$$I = \frac{1}{12}bh^3. {(4.12)}$$

where b is the width of the beam and h is the vertical thickness. Thus, I_a for Figure 4.4(a) is smaller than I_b for Figure 4.4(b). Substituting I_a and I_b into Equation 4.11 individually, it can be seen that the curvature for the second beam is indeed smaller than that of the first beam.

In a flat sheet, a stiffening rib can be used to increase the effective moment of inertia (see Figure 4.5). The addition of the central depression in the plate will act as a stiffening rib in the plate and give an increased resistance to bending. These same principles could be applied to the cylinder. For the cylinder, the moment of inertia is a function of both the wall thickness and the (current, or instantaneous) cylinder radius. Increasing the wall thickness has already been deemed undesirable and a global change to the diameter is not feasible. So, a local change in the geometry was proposed to increase the moment of inertia. This would produce the desired increase in bending stiffness, while, at the same time, possibly enhancing the aesthetics for commercial applications.

Figure 4.6 shows a model of the cylinder with the addition of a circumferential stiffening rib. The placement of the rib was such that upon the completion of the swaging process the rib would approximately be at the midpoint of the ramped portion into the "alley". The axial width of the stiffening rib was chosen to be one third of the overall length of the ramped portion of the cylinder and the depth was arbitrarily chosen to be one quarter of the width of the rib length. The initial stresses induced by the formation of the stiffening rib were not calculated as the primary purpose of the following numerical results was to observe the effect of the stiffening rib on the forming paths and the final geometry. Figures 4.6 through 4.8 show the initial geometry of the cylinder with the stiffening rib, the formed geometry, and the final geometry upon tool release. The final geometry has a characteristic stairstep shape. However, despite the apparent large change in geometry, the strain and stress distribution was not significantly affected, as evidenced by comparing Figures 4.9 through 4.12 to Figures 3.23 through 3.26 which did not include the stiffener. Nevertheless, the objective behind the stiffening rib was not reduction in stress and strain level, but an increase in the stability of the critical region.

Introduction of the stiffening rib into the final geometry of the cylinder may be achieved in several manners. The simplest would be to use rollers or a stamping operation on the flat sheet before bending into the shape of the cylinder. A consequence of this may be difficulties in obtaining strong weld seams in the swaged zone of the cylinder. The stiffening rib may also be produced in the cylinder after the welding process has been finished. One possibility is to use a clamp-like tool with appropriately shaped complimentary rollers on opposite sides. The clamp can be closed, rotated around the circumference of the cylinder to create the desired shape, and then removed. Finally, the stairstep shape may be

realized by using a multi-stage forming process similar to that of this study to gain additional "steps" in the critical region. For example in the current tooling the amount of diameter reduction produced by the first stage tool could be decreased and the translation of the second stage truncated. This would require only small modifications to the current tooling.

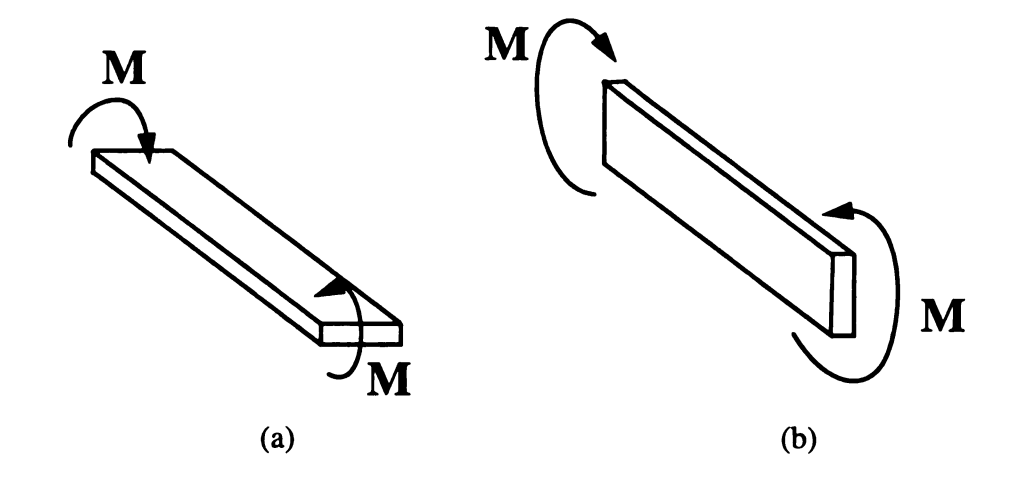


Figure 4.4 Simple Beam Subjected to a Bending Moment.

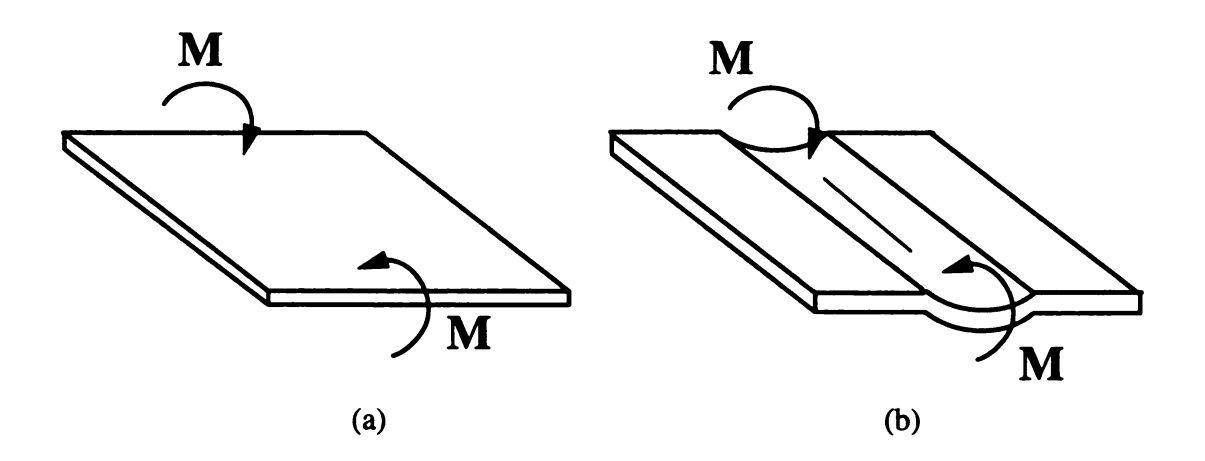


Figure 4.5 Plate Subjected to a Bending Moment.

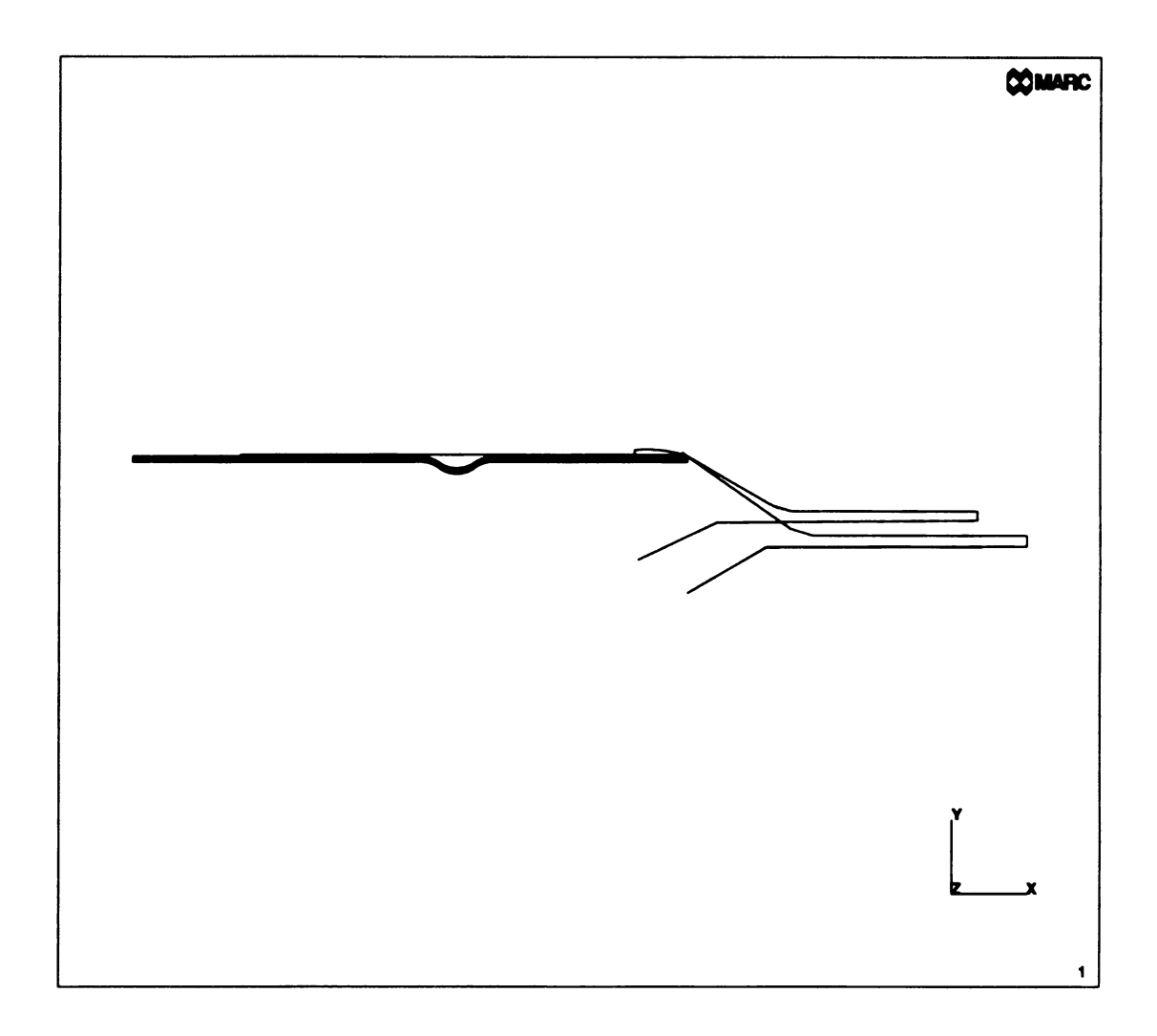


Figure 4.6 Initial Geometry of Cylinder with Added Stiffening Rib.

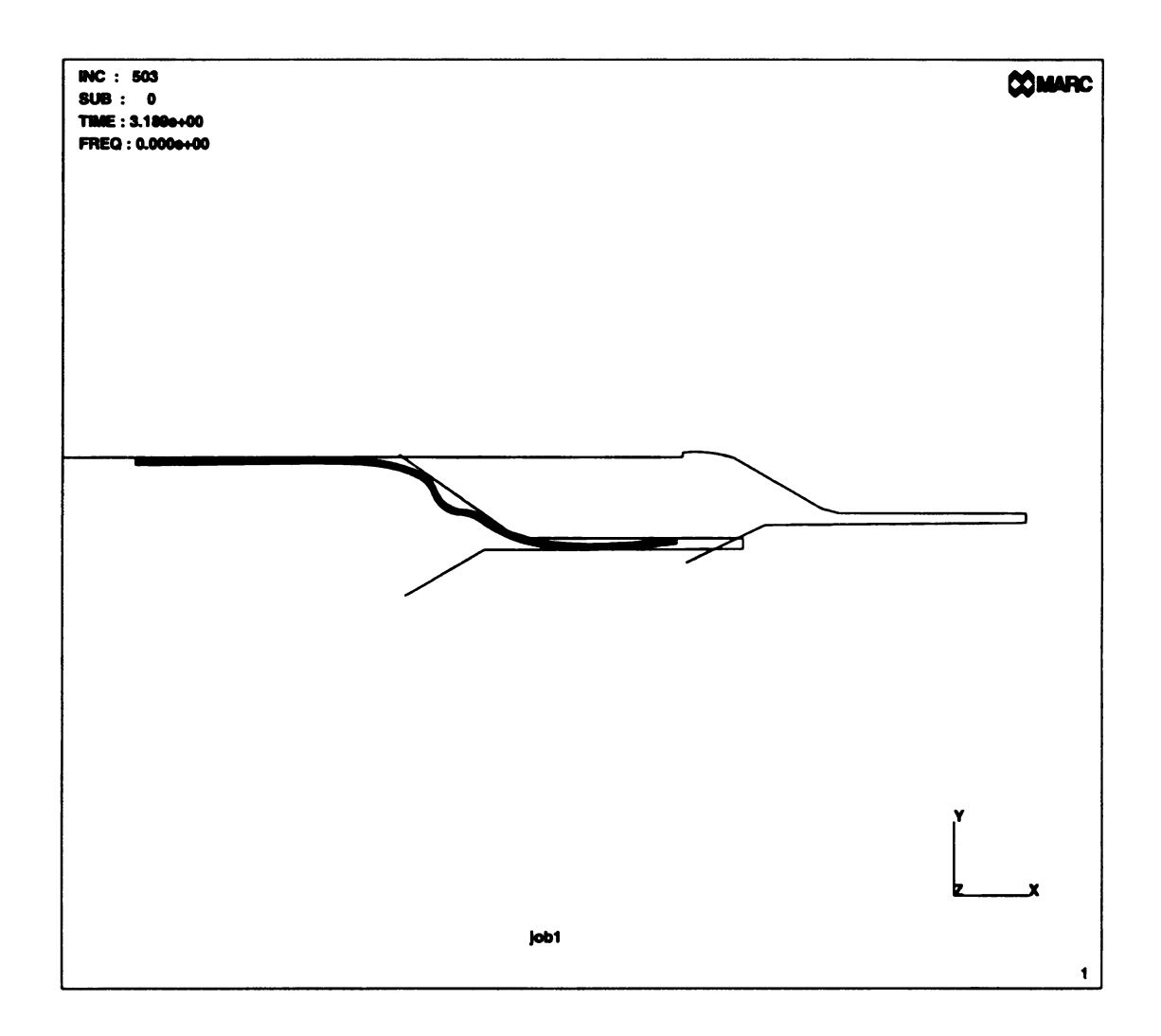


Figure 4.7 Formed Shape of the Cylinder with Added Stiffening Rib.

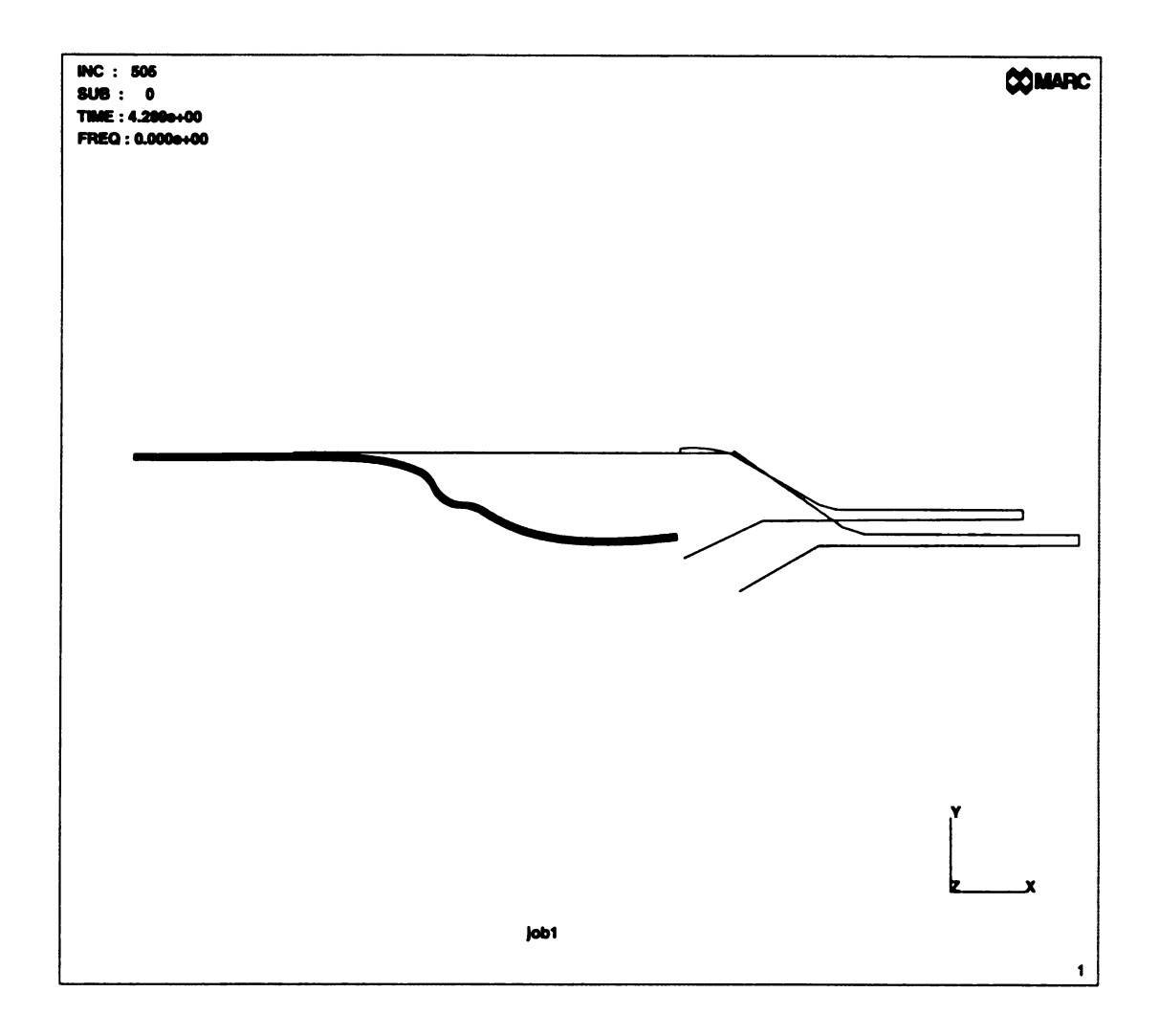


Figure 4.8 Final Shape of the Cylinder with Added Stiffening Rib after Elastic Snapback.

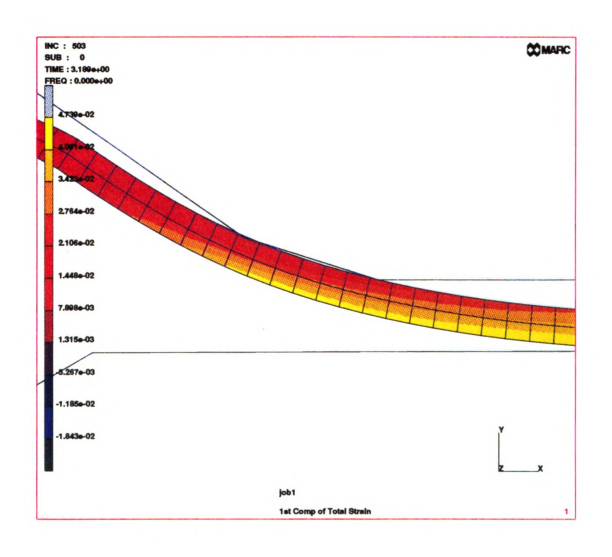


Figure 4.9 Axial Strains in the Critical Region of the Cylinder with Added Stiffening Rib.

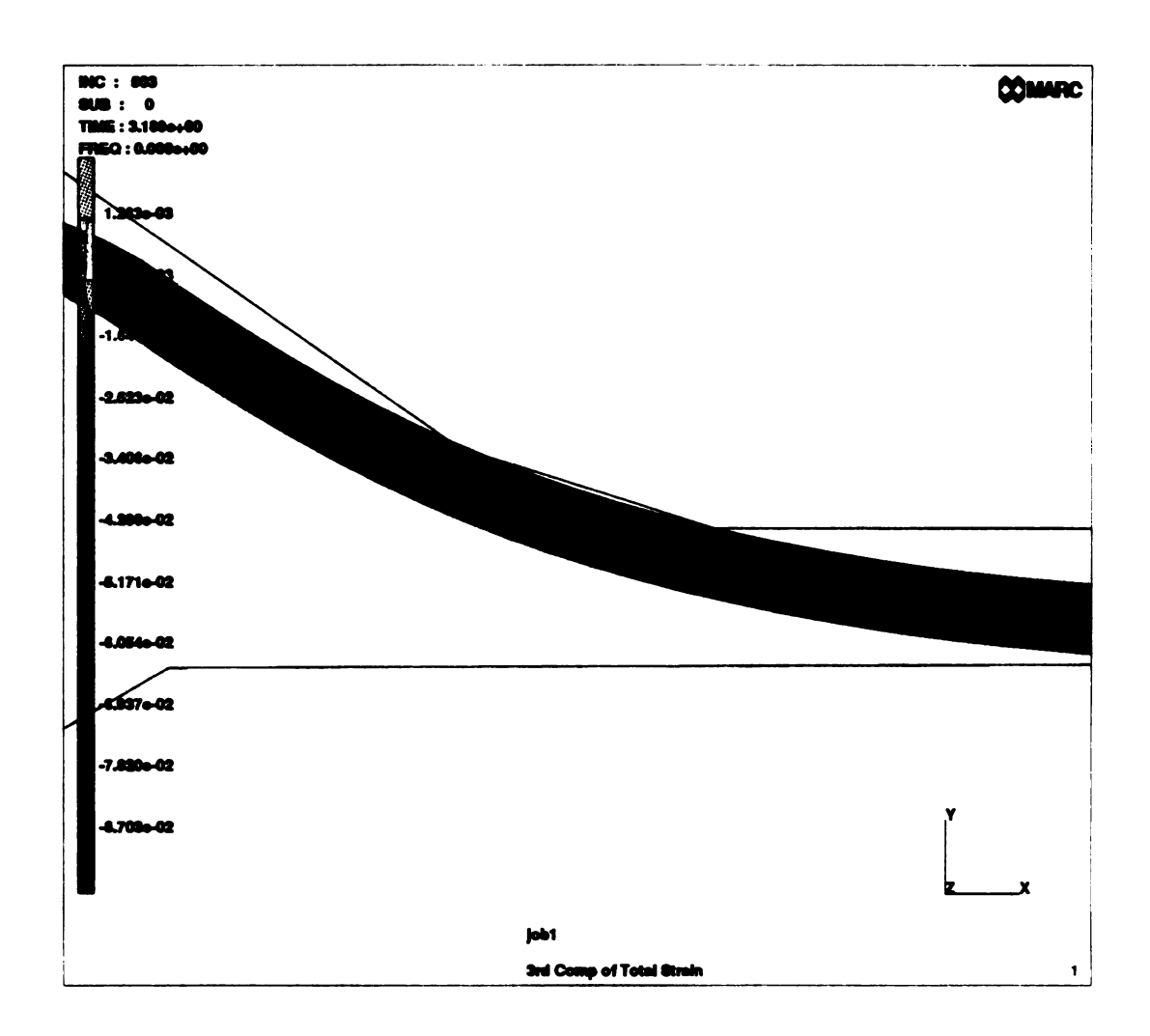


Figure 4.10 Circumferential Strains in the Critical Region of the Cylinder with Added Stiffening Rib.

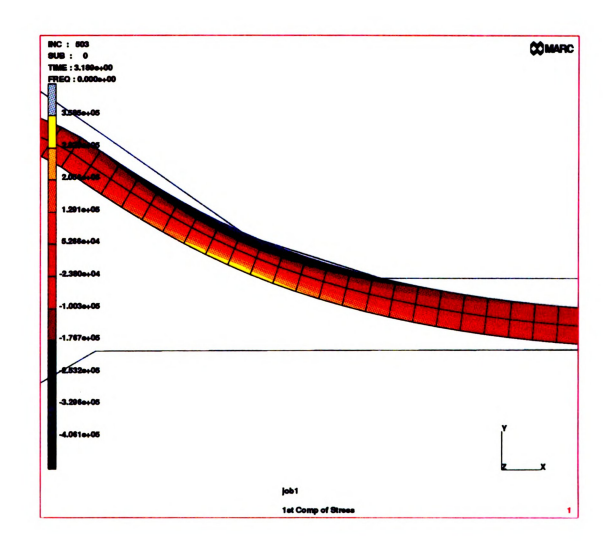


Figure 4.11 Axial Stresses in the Critical Region for the Cylinder with Added Stiffening Rib.

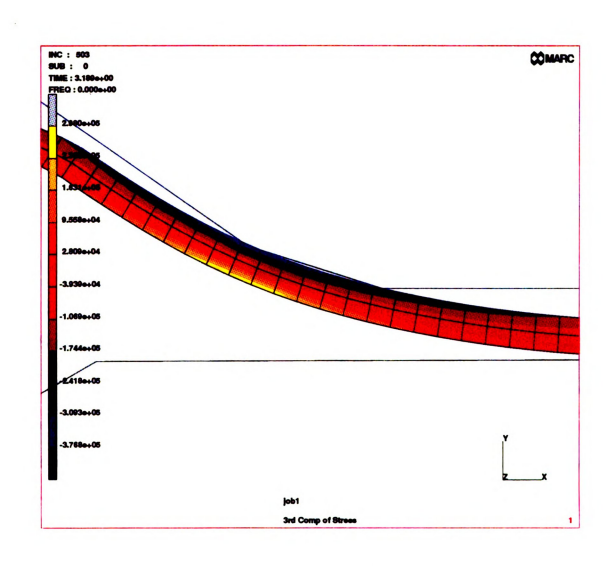


Figure 4.12 Circumferential Stresses in the Critical Region for the Cylinder with Added Stiffening Rib.

Chapter 5

Summary and Future Work

5.1 Summary

The stated objectives of the project were to determine the deformations and the stress state of the cylinder during the swaging operation. Each of these goals has been accomplished through the use of a numerical simulation of each step in the manufacturing process. Simple examples were then used to interpret the results obtained from the analyses. From the explanations offered, a hypothesis of the mechanism responsible for the formation of the wrinkles was presented. Finally, candidate solution methods were proposed, with the most reasonable being partially studied using in the finite element model. Throughout this simulation the cost was in man time to develop the model and to subsequently run the model on the computer. At no time was any physical simulation performed, thereby yielding a cost reduction in raw materials for test construction of the

cylinder and the forming tools. In addition, any follow up work or additional proposals can be performed using the developed model as a basis. Shortcomings have, however, been demonstrated within the model.

The use of element 10, which is based on a continuum formulation, has proven to be inherently expensive for the type of analysis being done, as pointed out by Rebolo, et al. (1990). In the initial convergence studies done to confirm the most appropriate element for use in the simulation, element 10 required a large number of elements to reach the exact solutions sought, while the shell elements converge to the closed form solution quickly. Again, in the convergence studies performed to determine mesh size, convergence was slow and actually never achieved using element 10. Although acceptable solutions were found in each case, the computational cost involved was considerable. The conclusion must be drawn that an alternative should be found. The model developed does not predict the formation of wrinkles in the cylinder. This does not diminish the results obtained up to this point, but only presents the opportunity for further work.

5.2 Future Work

It is proposed to develop a new finite element based on nonlinear shell theory and a novel formulation that appears to be ideally suited for analysis of sheet metal forming processes. The theory is based on a displacement field that allows a cubic distribution through the thickness of the inplane displacement components and satisfies the shear traction boundary conditions on the top and bottom surfaces of the shell. For cylindrical shells undergoing axisymmetric deformations, the displacement field takes the form,

$$u_{x}(x,z) = u(x) + z\psi_{x}(x) + \frac{z^{2}}{h}k_{51} + \frac{4z^{3}}{3h^{2}} \left[k_{52} - \psi_{x}(x) - \frac{dw}{dx} \right]$$

$$u_{y}(x,z) = v(x) + z\psi_{y}(x) + \frac{z^{2}}{h}k_{41} + \frac{4^{3}}{3h^{2}} \left[k_{42} - \psi_{y}(x) - \frac{v(x)}{R} \right]$$

$$u_{z}(x,z) = w(x)$$
(5.1)

where u_x , u_y , and u_z are the displacements of a point in the shell in the x (axial), y (circumferential), and z (thickness) directions respectively, and,

$$k_{51} = \frac{1}{2} \left(\frac{\tau_{5}^{t}}{Q_{55}^{(N)}} - \frac{\tau_{5}^{b}}{Q_{55}^{(1)}} \right) \qquad k_{52} = \frac{1}{2} \left(\frac{\tau_{5}^{t}}{Q_{55}^{(N)}} + \frac{\tau_{5}^{b}}{Q_{55}^{(1)}} \right)$$

$$k_{41} = \frac{1}{2} \left(\frac{\tau_{4}^{t}}{Q_{44}^{(N)}} - \frac{\tau_{4}^{b}}{Q_{44}^{(1)}} \right) \qquad k_{42} = \frac{1}{2} \left(\frac{\tau_{4}^{t}}{Q_{44}^{(N)}} + \frac{\tau_{4}^{b}}{Q_{44}^{(1)}} \right)$$
(5.2)

 τ_4^l , τ_4^l and τ_5^l , τ_5^b are the shear tractions on the top and bottom surfaces of the shell in x and y directions, respectively and $Q_{44}^{(1)}$, $Q_{44}^{(N)}$ and $Q_{55}^{(1)}$, $Q_{55}^{(N)}$ are the transverse shear stiffnesses in the first and Nth layer of the shell in the yz and xz planes, respectively. The shear tractions must be known, and may be due to friction between the tool and the cylinder. In the current analysis friction was ignored, so $k_{51} = k_{52} = k_{41} = k_{42} = 0$.

The nonlinear shell theory based on the above displacement field allows for transverse shearing effects and a nonlinear distribution through the thickness of deformations due to bending. Such higher order effects are usually neglected in the analysis of thinwalled structures. However, these effects may be important for nonlinear deformations,

and the inclusion of these effects allows the satisfaction of shear tractions on the top and bottom surfaces of the shell, yielding a more accurate physical description of the problem. This element, once formulated, could be used in the current analysis to provide a very accurate, efficient, and robust model for thin cylinders undergoing axisymmetric deformations.

The use of the new element would remove the current barriers to reaching a converged solution, but does not allow for the prediction of wrinkling in the swaging process. To accomplish this, a method similar to that proposed by Adams (1993) could be employed. Once a converged solution to the axisymmetric forming problem has been found the analysis could be rerun, seeking the onset of wrinkling. This could done by checking the solution after each stage of the forming process, to determine if circumferential buckling has occurred. Tracing the determinant of the characteristic system of equations for cylindrical shells to determine when (or if) it goes to zero would indicate that the cylinder has buckled or wrinkled.

The characteristic system of equations could be formulated from the non-axisymmetric form of the governing equations of the nonlinear shell theory discussed above. The circumferential variations of the deformations, in this case, could be approximated using a Fourier series method. In this method, the problem is analyzed for several independent harmonics which are superimposed to give a final solution. Because of the independence of the harmonics only those harmonics which influence the buckling of the cylinder need be analyzed. Use of this method is possible because the circumferential direction (the rolling direction) is also a principal material direction, and the cylinder geometry is axisymmetric. Therefore, each of the five degrees of freedom may be represented by a Fourier series in y,

$$u(x, y) = \sum_{n=1}^{\infty} \overline{u_n}(x) \cos \frac{ny}{R} = \sum_{n=1}^{m} \sum_{i=1}^{2} \overline{u_{in}} P_i(x) \cos \frac{ny}{R}$$

$$v(x, y) = \sum_{n=1}^{\infty} \overline{v_n}(x) \sin \frac{ny}{R} = \sum_{n=1}^{m} \sum_{i=1}^{2} \overline{v_{in}} P_i(x) \sin \frac{ny}{R}$$

$$w(x, y) = \sum_{n=1}^{\infty} \overline{w_n}(x) \cos \frac{ny}{R} = \sum_{n=1}^{m} \sum_{i=1}^{3} \overline{w_{in}} N_i(x) \cos \frac{ny}{R}$$

$$\psi_x(x, y) = \sum_{n=1}^{\infty} \overline{\psi_{x_n}}(x) \cos \frac{ny}{R} = \sum_{n=1}^{m} \sum_{i=1}^{2} \overline{\psi_{x_{in}}} P_i(x) \cos \frac{ny}{R}$$

$$\psi_y(x, y) = \sum_{n=1}^{\infty} \overline{\psi_{y_n}}(x) \cos \frac{ny}{R} = \sum_{n=1}^{m} \sum_{i=1}^{2} \overline{\psi_{x_{in}}} P_i(x) \cos \frac{ny}{R}$$

where m is the number of Fourier harmonics, P_i are the linear Lagrange interpolation functions, and N_i are the quadratic Lagrange interpolation functions. In the above equations the DOF are approximated in the circumferential direction by the product of a trigonometric function and an amplitude term, with the axial variation of the amplitudes approximated by the finite element method. Also of note is the approximation \overline{w}_n . In this case, an interdependent interpolation scheme is employed to allow for greater accuracy without an increase in computational cost. The third DOF in the element approximation of \overline{w}_n would be eliminated before assembly by imposing a constraint on the variation of transverse shear strain (see Averill, 1994 and Tessler, 1983)

Due to the form of the displacement approximations in Equation (5.3), integration in the thickness and circumferential directions can be performed analytically, so that the model is reduced to one dimension (along the axis of the cylinder). The final model is given as,

$$K_{ij}^n d_i^n = F_j^n (5.4)$$

where n is the Fourier harmonic, K the global stiffness matrix, d the Fourier series amplitude, and F the force matrix. The characteristic system of equations is obtained for each harmonic to measure the stability of the current configuration. When the determinant goes to zero for a given harmonic, buckling is predicted to occur, with a buckling pattern wavelength related to n.

The development of the axisymmetric, nonlinear shell element is currently being conducted by other researchers. Upon completion of the development, the element can be implemented into the current model for solution of the axisymmetric forming problem. The solutions from this analysis must then be coupled with the proposed wrinkling analysis formulation to complete the solution.



A.1 Mesh Refinement Study Data

In Section 3.3.1, an elemental convergence study was conducted on the first stage of the forming process. In this study a series of meshes were analyzed using the developed model. From those analyses data was collected on the outer, mid-plane, and inner surfaces of the cylinder at locations within the first bending region and the critical region. Tables A.1 through A.24 contain all of that data collected.

Table A.1 Axial Strain on the Outer Surface in the First Bending Region. (x10⁻³)

Elements	2	3	4	5	6	8
150	14.3964	15.2937	15.2429	15.2084	15.2017	15.2091
300	14.2752	15.6635	15.5345	15.6663	15.6150	15.7637
400			15.6079	15.7318	15.8140	

Table A.2 Axial Strain on the Mid-Plane Surface in the First Bending Region. (x10⁻³)

Mesh	2	3	4	5	6	8
150	0.838835	1.233395	0.997778	0.98309	0.953442	0.923400
300	0.645666	1.45242	1.04027	1.00798	0.990998	0.884100
400			1.12246	1.158305	1.080070	

Table A.3 Axial Strain on the Inner Surface in the First Bending Region. (x10⁻³)

Mesh	2	3	4	5	6	8
150	-13.2124	-13.1500	-13.5015	-13.4648	-13.4725	-13.5070
300	-13.4868	-13.0982	-13.7462	-13.9155	-13.9076	-14.1870
400			-13.6394	-13.6624	-13.8760	

Table A.4 Circumferential Strain on the Outer Surface in the First Bending Region. $(x10^{-3})$

Mesh	2	3	4	5	6	8
150	-6.98879	-6.93845	-6.91135	-6.96230	-6.97252	-6.64920
300	-6.90258	-6.82011	-6.70422	-6.66099	-6.68490	-6.63974
400			-6.85317	-6.85937	-6.81014	

Table A.5 Circumferential Strain on the Mid-Plane Surface in the First Bending Region. $(x10^{-3})$

Mesh	2	3	4	5	6	8
150	-6.92393	-6.87485	-6.84736	-6.899825	-6.90983	-6.91335
300	-6.83654	-6.75465	-6.63764	-6.59537	-6.61930	-6.57391
400			-6.78859	-6.79609	-6.74601	

Table A.6 Circumferential Strain on the Inner Surface in the First Bending Region. $(x10^{-3})$

Mesh	2	3	4	5	6	8
150	-6.89687	-6.84650	-6.82324	-6.87584	-6.88715	-6.89121
300	-6.80847	-6.72467	-6.68394	-6.56921	-6.59467	-6.54976
400			-6.76480	-6.77228	-6.72332	

Table A.7 Axial Stress on the Outer Surface in the First Bending Region. (kPsi)

Mesh	2	3	4	5	6	8
150	240.268	187.504	158.886	138.823	126.935	111.188
300	240.424	191.156	162.397	144.685	132.495	115.812
400			157.724	140.057	128.731	

Table A.8 Axial Stress on the Mid-Plane Surface in the First Bending Region. (kPsi)

Mesh	2	3	4	5	6	8
150	0.17758	-4.8125	-65.3146	-8.3254	-10.2651	-11.9106
300	1.14157	-4.7234	-65.3091	-8.6686	-10.8890	-13.7535
400			-45.8308	-6.54295	-8.965.84	

Table A.9 Axial Stress on the Inner Surface at in the First Bending Region. (kPsi)

Mesh	2	3	4	5	6	8
150	-268.912	-208.256	-176.320	-153.901	-140.543	-122.824
300	-271.538	-213.056	-180.558	-159.968	-146.372	-127.406
400			-171.748	-152.187	-139.352	

Table A.10 Circumferential Stress on the Outer Surface in the First Bending Region. (kPsi)

Mesh	2	3	4	5	6	8
150	155.628	106.460	78.7539	58.5953	47.0817	31.7309
300	156.503	109.640	81.7260	64.5423	52.8537	362061
400			75.4760	58.2574	47.2932	

Table A.11 Circumferential Stress on the Mid-Plane Surface in the First Bending Region. (kPsi)

Mesh	2	3	4	5	6	8
150	-55.8569	-56.7963	-62.6269	-614201	-64.9001	-657393
300	-58.4541	-58.0932	-65.3584	-63.0065	-67.8407	-69.1656
400			-65.8639	-63.9364	-68.2242	

Table A.12 Circumferential Stress on the Inner Surface in the First Bending Region. (kPsi)

Mesh	2	3	4	5	6	8
150	-256.441	-198.253	-165.400	-145.595	-131795	-114095
300	-258.999	-199.263	-167.479	-147.434	-132.657	-116.286
400			-172.804	-151.758	-138.334	

Table A.13 Axial Strains on the Outer Surface in the Critical Region. (x10⁻³)

Mesh	2	3	4	5	6	8
150	-4.18674	-1.04515	-0.278518	0.101525	0.336483	0.644162
300	35759	1.75286	0.14918	0.551638	0.517526	0.929506
400			-0.333748	0.122887	0.424808	

Table A.14 Axial Strains on the Mid-Plane Surface in the Critical Region. (x10⁻³)

Mesh	2	3	4	5	6	8
150	17.8305	19.05300	18.9696	18.9899	19.0050	18.9928
300	18.2751	23.7753	18.8816	18.8507	19.3794	19.2492
400			19.2907	19.3346	19.3919	

Table A.15 Axial Strains on the Inner Surface in the Critical Region. (x10⁻³)

Mesh	2	3	4	5	6	8
150	38.8382	38.3533	37.7740	37.6701	37.6560	37.5003
300	39.1136	44.6235	37.4199	37.1498	38.2427	37.8484
400			38.5379	38.4350	38.4716	

Table A.16 Circumferential Strains on the Outer Surface in the Critical Region. $(x10^{-3})$

Mesh	2	3	4	5	6	8
150	-52.3648	-52.3186	-52.3061	-52.3227	-52.3256	-52.3274
300	-52.3355	-52.4560	-51.7063	-51.6914	-53.7710	-52.3589
400			-52.2466	-52.2544	-52.4124	

Table A.17 Hoop Strains on the Mid-Plane Surface in the Critical Region. (x10⁻³)

Mesh	2	3	4	5	6	8
150	-52.4591	-52.4024	-52.3916	-52.4067	-52.4104	-52.4121
300	-52.4281	-52.5357	-51.7063	-51.7540	-52.4607	-52.4428
400			-52.3256	-52.3312	-52.4950	

Table A.18 Hoop Strains on the Inner Surface in the Critical Region. (x10⁻³)

Mesh	2	3	4	5	6	8
150	-52.4937	-52.4353	-52.4211	-52.4368	-52.4393	-52.4409
300	-52.4615	-52.5579	-51.7774	-51.7640	-52.4881	-52.4710
400			-52.3482	-52.3537	-52.5213	

Table A.19 Axial Stresses on the Outer Surface in the Critical Region. (kPsi)

Mesh	2	3	4	5	6	8
150	-360.213	-246.750	-197.342	-171.537	-153.706	-127.704
300	-354.848	-232.841	-208.305	-177.613	-155.114	-130.090
400			-216.718	-186.542	-164.428	

Table A.20 Axial Stresses on the Mid-Plane Surface in the Critical Region. (kPsi)

Mesh	2	3	4	5	6	8
150	12.007	4.2907	2.18321	1.0688	-0.00944	-2.0748
300	12.5069	4.06294	5.9629	4.2178	1.6014	0.0673
400			6.5923	4.3753	3.7378	

Table A.21 Axial Stresses on the Inner Surface in the Critical Region. (kPsi)

Mesh	2	3	4	5	6	8
150	335.940	226.770	180.082	157.769	140.193	117.602
300	331.314	266.730	197.465	168.970	144.993	122.361
400			201.974	174.301	154.099	

Table A.22 Circumferential Stresses on the Outer Surface in the Critical Region. (kPsi)

Mesh	2	3	4	5	6	8
150	-394.100	-284.650	-233.855	-204.445	-185.684	-160.038
300	-397.440	-282.371	-235.476	-204.863	-189.751	-162.522
400			-238.453	-209.154	-188.076	

Table A.23 Circumferential Stresses on the Mid-Plane Surface in the Critical Region. (kPsi)

Mesh	2	3	4	5	6	8
150	-58.9971	-63.8572	-68.5703	-67.9680	-70.7456	-70.9200
300	-59.7367	-20.7880	-67.0310	-66.2861	-71.3535	-72.1101
400						

Table A.24 Circumferential Stresses on the Inner Surface in the Critical Region. (kPsi)

Mesh	2	3	4	5	6	8
150	253.175	155.333	109.250	83.8303	66.7538	44.0962
300	247.643	204.532	119.618	91.9736	65.4983	43.4282
400			123.298	96.5859	76.1358	

A.2 Analysis Results without Strain Hardening

The effects of strain hardening on the analysis results were evaluated in Section 3.4.2. It was determined at that time the effects were minimal at most. This may be conformed by comparing the plots that follow in Figure A.1 - A.4 to those of Figures 3.23 - 3.26. Doing so will show that while the magnitudes of the strain and stress values have small incremental changes, the trends remain constant. Therefore, strain hardening effects are categorized as minimal.

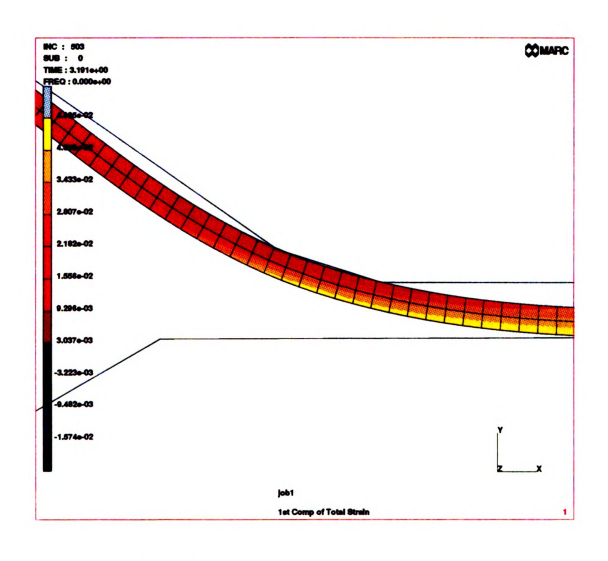


Figure A.1 Axial Strains in the Critical Region Without Work Hardening.

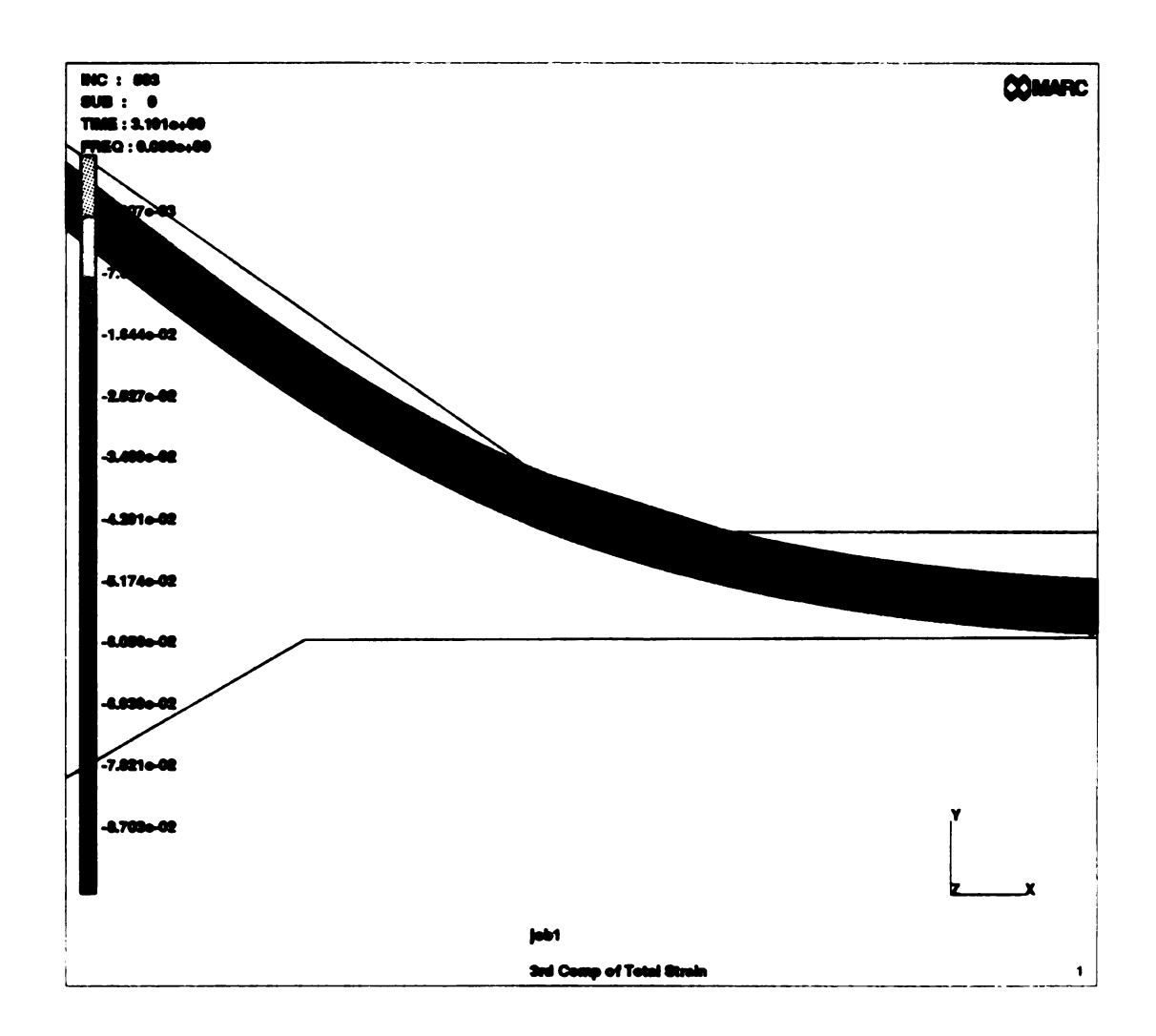


Figure A.2 Circumferential Strains in the Critical Region Without Work Hardening.

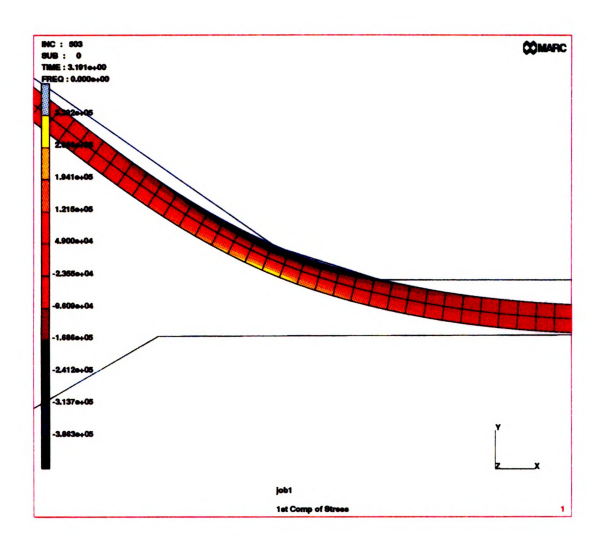


Figure A.3 Axial Stresses in the Critical Region Without Work Hardening.

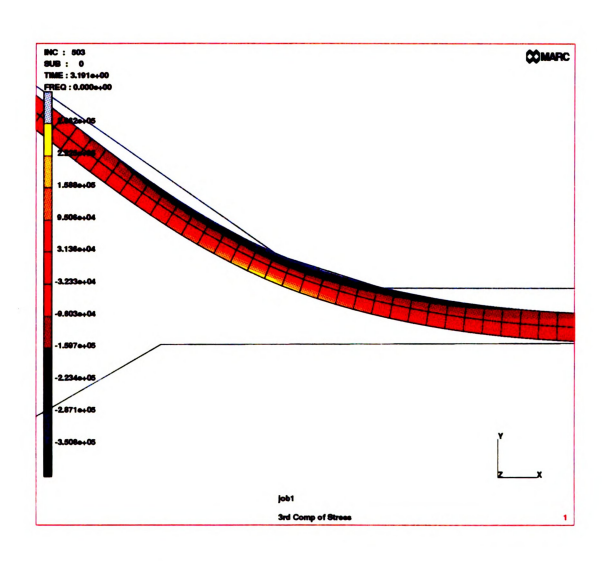


Figure A.4 Circumferential Stresses in the Critical Region Without Work Hardening.



Adams, G. G., (1993), "Elastic Wrinkling of a Tensioned Circular Plate Using von Karman Plate Theory", **Journal of Applied Mechanics**, 60, pp. 520 - 525

Averill, R. C. and Reddy, J. N., (1990), "Behaviour of Plate Elements Based on the First Order Shear Deformation Theory", **Engineering Computing**, vol. 7, pp. 57-74

Averill, R. C., (1994) "Static and Dynamic Response of Moderately Thick Laminated Beams with Damage", Composites Engineering, vol. 4, pp. 381-395

Butman, J., (1991), Car Wars, Grafton Book, London, p 11

Chan, S. L., (1993), "A Non-Linear Numerical Method for Accurate Determination of Limit and Bifurcation Points", International Journal for Numerical Methods in Engineering, vol. 36, pp. 2779 - 2790

Dym, C. L., (1974), **Introduction to the Theory of Shells**, Pergamon Press, Oxford, p. 26.

Eterovic, A. L. and Bathe, K. J., (1991), "On the Treatment of Inequality Constraints Arising form Contact Conditions in Finite Element Analysis", Computers and Structures, vol. 40, pp. 203-209

Green, C. M., (1956), Eli Whitney and the Birth of American Technology, Little, Brown and Company, Boston, p. 120

Kalpakjian, S., (1991), "Manufacturing Processes for Engineering Materials", Second Edition, Addison-Wesley Publishing Company, Reading, MA, pp. 461-462

Keck, P., Wilhelm, M., and Lange, K., (1991), "Application of the Finite Element Method to the Simulation of Sheet Forming Processes: Comparison of Calculations and Experiments", International Journal for Numerical Methods in Engineering, vol. 30, pp. 1415-1430

Lee, J. K., Cho, U. Y., and Hambrecht, J., (1991), "Recent Advances in Sheet Metal Forming Analysis", Advances in Finite Deformation Problems in Materials Processing and Structures, ASME 1991, AMD vol.125

MARC User's Guide Volume A: User Information, (1994), MARC Analysis Research Corporation, Palo Alto, CA

Mendelson, A., (1968), **Plasticity: Theory and Application**, Robert E. Krieger Publishing Company, Malabar, FL.

Mentat II Command Reference, (1994), MARC Analysis Research Corporation, Palo Alto, CA

Neale, K.W. and Tugcu, P., (1990), "A Numerical Analysis of Wrinkle Formation Tendencies in Sheet Metals", International Journal for Numerical Methods in Engineering, vol. 30, pp. 1595-1608

Padovan, J., (1974), "Quasi-Analytical Finite Element Procedures for Axisymmetric Anisotropic Shells and Solids", Computers and Structures, vol. 4, pp. 467 - 483

Parr, G., (1958), Man, Metals and Modern Magic, American Society for Metals, Cleveland and The Iowa State University Press, Ames, Iowa

Rebolo, N., Nagetaal, J. C., and Hibbitt, H. D., (1990), "Finite Element Analysis of Sheet Forming Processes", International Journal for Numerical Methods in Engineering, vol. 30, pp. 1739 - 1758

Reddy, J. N., (1984), Energy and Variational Methods in Applied Mechanics, John Wiley and Sons, New York

Riccobno, R., (1992), "A Comparison Between Two Different Models for Metal Forming FEM Analysis", Computers and Structures, vol. 44, pp. 429-433

Sedaghat, M. and Herrmann, L. R., (1983), "A Nonlinear, Semi-Analytical Finite Element Analysis for Nearly Axisymmetric Solids", Computers and Structures, vol. 17, no. 3, pp. 389 - 401

Simo, J. C., Wriggers, P., and Taylor, R. L., (1985), "A Perturbed Lagrangian Formulation for the Finite Element Solution of Contact Problems", Computer Methods in Applied Mechanics and Engineering, vol. 50, pp. 163 - 180

Tessler, A. and Hughes, T. J. R., (1983), "An Improved Treatment of Transverse Shear in the Mindlin-Type Four-Node Quadrilateral Element", Computer Methods in Applied Mechanics and Engineering, vol. 39, pp. 311-335

Toh, C. H., (1989), "Prediction of the Forming Limit Curves of Sheet Materials Using the Rigid-Plastic Finite Element Method", International Journal of Machine Tools and Manufacture, vol. 29, pp. 333-343

Wood, M. D., (1994), "The Effect of Microstructure and Texture on the Mechanical Properties of Double-Reduced Tinplate Steel", Master's Thesis, Michigan State University, East Lansing, Michigan

Zhang, L. C. and Yu T. X., (1988), "The Plastic Wrinkling of an Annular Plate Under Uniform Tension on Its Inner Surface", **International Journal of Solid Structures**, vol 24, no. 5, pp. 497 - 503

Zienkiewicz, O. C. and Taylor, R. L., (1989), **The Finite Element Method**, McGraw-Hill, New York